Modeling the Interior of Haumea

by

Luke Probst

A Thesis Presented in Partial Fulfillment
of the Requirements for the Degree
Master of Science

Approved April 2015 by the
Graduate Supervisory Committee:

Steven Desch, Chair
Erik Asphaug
James Bell

ARIZONA STATE UNIVERSITY

May 2015

ABSTRACT

The Kuiper Belt Object Haumea is one of the most fascinating objects in the solar system. Spectral reflectance observations reveal a surface of almost pure water ice, yet it has a mass of 4.006×10^{21} kg, measured from orbits of its moons, along with an inferred mean radius of 715 km, and these imply a mean density of around 2600 kg m^{-3}. Thus the surface ice must be a veneer over a rocky core. This model is supported by observations of Haumea's light curve, which shows large photometric variations over an anomalously rapid 3.9154-hour rotational period. Haumea's surface composition is uniform, therefore the light curve must be due to a varying area presented to the observer, implying that Haumea has an oblong, ellipsoidal shape. If Haumea's rotation axis is normal to our line of sight, and Haumea reflects with a lunar-like scattering function, then its axis ratios are $p = b/a = 0.80$ (in the equatorial cross section) and $q = c/a = 0.52$ (in the polar cross section). In this work, I assume that Haumea is in hydrostatic equilibrium, and I model it as a two-phase ellipsoid with an ice mantle and a rocky core. I model the core assuming it has a given density in the range between 2700–3300 kg m^{-3} with axis ratios that are free to vary. The metric which my code uses calculates the angle between the gravity vector and the surface normal, then averages this over both the outer surface and the core-mantle boundary. When this fit angle is minimized, it allows an interpretation of the size and shape of the core, as well as the thickness of the ice mantle. Results of my calculations show that Haumea's most likely core density is 2700–2800 kg m^{-3}, with ice thicknesses anywhere from 12–32 km over the poles and as thin as 4–18 km over the equator.

TABLE OF CONTENTS

CHAPTER Page

LIST OF TABLES

LIST OF FIGURES

Figure Page

Figure Page

Figure Page

Chapter 1

BACKGROUND

1.1 Introduction

1.1.1 A Brief Introduction to Haumea

Of the variety of objects known in the solar system, none quite compares to the icy dwarf planet named Haumea. Currently orbiting at a distance of 51 AU (Rabinowitz et al. 2006; hereafter R06), roughly 10 AU beyond Pluto's average distance in the Kuiper Belt of the outer solar system, Haumea displays many intriguing qualities. With a rotational period of roughly 3.9 hours and an apparent ellipsoidal shape with longest axis around 2000 km, Haumea is the most rapidly rotating large (>100 km) body in the solar system (R06). It is also one of the brightest known Kuiper Belt Objects (KBOs) after Pluto and Makemake, another dwarf planet (Brown et al. 2006). Its surface spectrum shows strong crystalline water ice absorption features covering the entire surface (Trujillo et al. 2007, hereafter T07; Pinilla-Alonso et al. 2009), yet its mass of 4.006×10^{21} kg, derived via observations of its two satellites' orbits (Ragozzine & Brown 2009; hereafter RB09), suggests an abnormally large density of roughly 2600 kg m^{-3}, so large that most of the body should be composed of rock and not ice.

All models and calculations of Haumea thus far have treated it with a single homogeneous density. In this work, Haumea is modeled as a two-phase ellipsoid with an ice mantle surrounding a rocky core. The gravitational potential is then calculated, with the primary goal of constraining Haumea's core density and size, thereby achieving a clearer understanding of Haumea's interior. Our approach is to

calculate the average deviation between the gravitational potential and the surface normal around the body, for both the outer surface and the core-mantle boundary (CMB), in order to provide constraints on the density of Haumea's core material. This will then allow a determination of the size and shape of the core as well as the thickness of the ice mantle.

1.1.2 Comparative KBOlogy

Given the many other large KBOs known currently, it is illustrative to examine their physical properties, in order to gain more perspective about Haumea. Starting with one of the largest KBOs and certainly the most well known, Pluto has a diameter of 2306 km and a density of 2030 kg m^{-3} (Buie et al. 2006). Haumea's mass is 31% that of Pluto's mass, 1.287×10^{22} kg, which Buie et al. measured using observations of three of Pluto's moons. Pluto is also the only other known multiple KBO system, with five satellites known currently. As for Pluto's interior, two-layer thermal models performed by Hussmann et al. (2006) assume a rocky core of density 3500 kg m^{-3} and an icy mantle of density 1000 kg m^{-3}. They then calculated a core radius of 855 km and an ice mantle thickness of 282 km. Using the following equation to calculate the silicate mass fraction f for a sphere,

$$f = \frac{\rho_{\text{core}}}{\rho_{\text{mantle}}\left(\left(\frac{R_{\text{planet}}}{R_{\text{core}}}\right)^3 - 1\right) + \rho_{\text{core}}}, \tag{1.1}$$

we find that according to this model, the amount of rock Pluto contains is around 72%.

These models found that the interior of Pluto is expected to be very similar to that of Eris (Hussmann et al. 2006), another large KBO currently orbiting roughly 97 AU out, three times Pluto's distance from the Sun (Brown et al. 2006). Using observations of its moon Dysnomia, Brown and Schaller (2007) measured Eris' mass

to be 1.66×10^{22} kg. From stellar occultation observations, Sicardy et al. (2011) measured its density to be 2520±50 kg m^{-3} and its visual albedo to be $0.96^{+0.09}_{-0.04}$. This makes Eris one of the brightest objects in the known solar system (Sicardy et al. 2011). If Eris is given a diameter of 2600 km, Hussmann et al.ś thermal models calculated Eris' core radius to be 914 km and its ice mantle to be anywhere from 169 km to 242 km thick. The former thickness corresponds to the ice containing 31.5% NH_3, while the latter value is derived if the ice mantle contains 3.4% NH_3 (Hussmann et al. 2006). With these dimensional values for Eris' interior, we calculate its silicate mass fraction to be around 65%, less than that of Pluto's, even though Eris' dimensions are slightly larger.

Makemake, the largest known KBO without a satellite, has been measured from stellar occultation to be slightly elongated in the north-south direction, with a polar diameter of 1420 km and an equatorial diameter of 1434 km (Brown 2013). It has an albedo of 0.81, and since it lacks a satellite, there is no known mass. However, Brown (2013) estimates its density to be anywhere in the range from 1400 kg m^{-3} to 3200 kg m^{-3}. Perhaps Makemake never experienced a collision event, which would have both potentially created satellites and increased its density (Brown 2013). In contrast to Haumea, Pluto, Eris, and Makemake are all covered in CH_4 ice, and are sometimes referred to as "Methanoids" (Lacerda 2010).

Focusing on some of the smaller large KBOs, Sedna is another object with no known mass, because it also has no known satellite (Pal et al. 2012). From thermal measurements taken with the Herschel Space Observatory, Sedna's diameter has been measured to be 995±80 km, and its albedo is 0.32. This makes Sedna very red, but yet still brighter than the average TNO (Trans-Neptunian Object) population (Pal et al. 2012).

Quaoar's diameter has been measured via stellar occultation to be 1138^{+48}_{-34} km, just a bit larger than Sedna (Braga-Ribas et al. 2013). Through observations of its moon Weywot, Quaoar's mass is estimated to be 1.6×10^{21} kg (roughly 10% that of Eris), with an estimated density of 4200 ± 1300 kg m^{-3} (Fraser & Brown 2010), an even higher density than that of Haumea! This unusually high density implies little to no ice content, despite surface absorption features which show crystalline water ice and ammonia hydrate (Jewitt & Luu 2004). This leads to the question of whether Quaoar is a displaced asteroid (Fraser & Brown 2010). Another possibility is that it experienced a collision which stripped it of its ice and left tiny Weywot (diameter 74 km) in a highly eccentric and highly inclined orbit (Fraser & Brown 2010). However, Braga-Ribas et al. (2013) recently used equilibrium considerations (which I will explain in a later section as applied to Haumea) to determine Quaoar's density to be 1990 ± 460 kg m^{-3}. This lower density still implies a large silicate content, though now not as large as that of Haumea.

Last but not least, the KBO Varuna is another fascinating object for our purposes here. Analysis of its light curve reveals a rapid rotation rate of 6.344 hours, and also a shape that is ellipsoidal! Jewitt and Sheppard (2002) measured Varuna's longest dimension to be around 900 km and its shortest to be roughly 465 km. From its light curve and equilibrium considerations for ellipsoids (also explained shortly), Lacerda and Jewitt (2007) calculated Varuna's density to be around 992 kg m^{-3}. With this low density, the silicate mass fraction is expected to be extremely low. Varuna is significantly smaller than Haumea and evidence suggests it may be asymmetrical in shape (Jewitt & Sheppard 2002), yet it still seems to be another case in addition to Haumea in which the ellipsoidal shape is linked with a fast spin rate.

With this brief overview of the properties of many of the largest known KBOs, their variabilities and their similarities, we will now examine Haumea in depth.

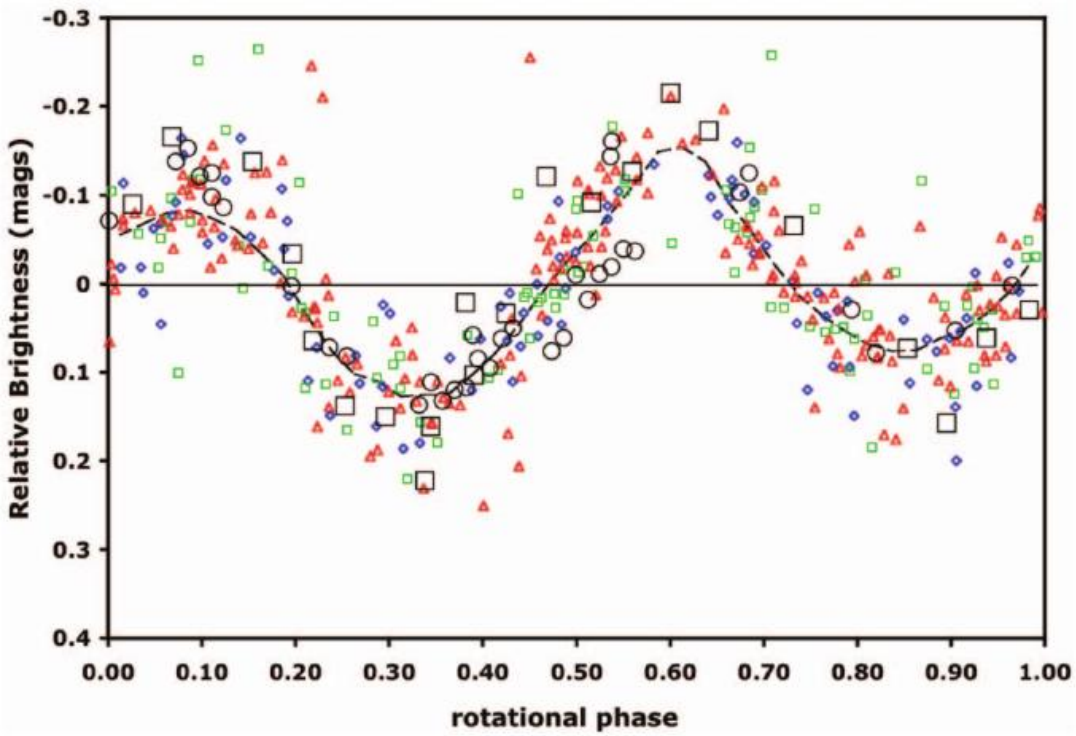

Figure 1.1: Haumea's Light Curve as a Function of Rotational Phase, Assuming a Period of 3.9154 Hours. The Blue, Green, and Red Symbols Correspond to B-Band, V-Band, and I-Band, Respectively, Measured with the SMARTS 1.3-m Telescope at Cerro Tololo. The Black Circles and Squares Correspond to Additional Observations with the 5.1-m Hale Telescope at Palomar Observatory and the 32-inch Telescope at Tenagra Observatory, Respectively. The Dashed Line Represents the Median Average of the Data (R06).

1.2 Observations of Haumea

1.2.1 Bulk Properties

Haumea was discovered December 28, 2004 by Brown et al. (2004) with the 48-inch Samuel Oschin Schmidt telescope at Palomar. Originally nicknamed "Santa", its two moons, discovered later, were nicknamed "Rudolph" and "Blitzen" (Ragozzine et al. 2008). Its current distance from the Sun is 51 AU, but it has quite an elliptical orbit, with a semimajor axis of 43.3 AU, eccentricity of 0.19, and orbital inclination of 28.2°, making it a member of the classical Kuiper Belt (R06).

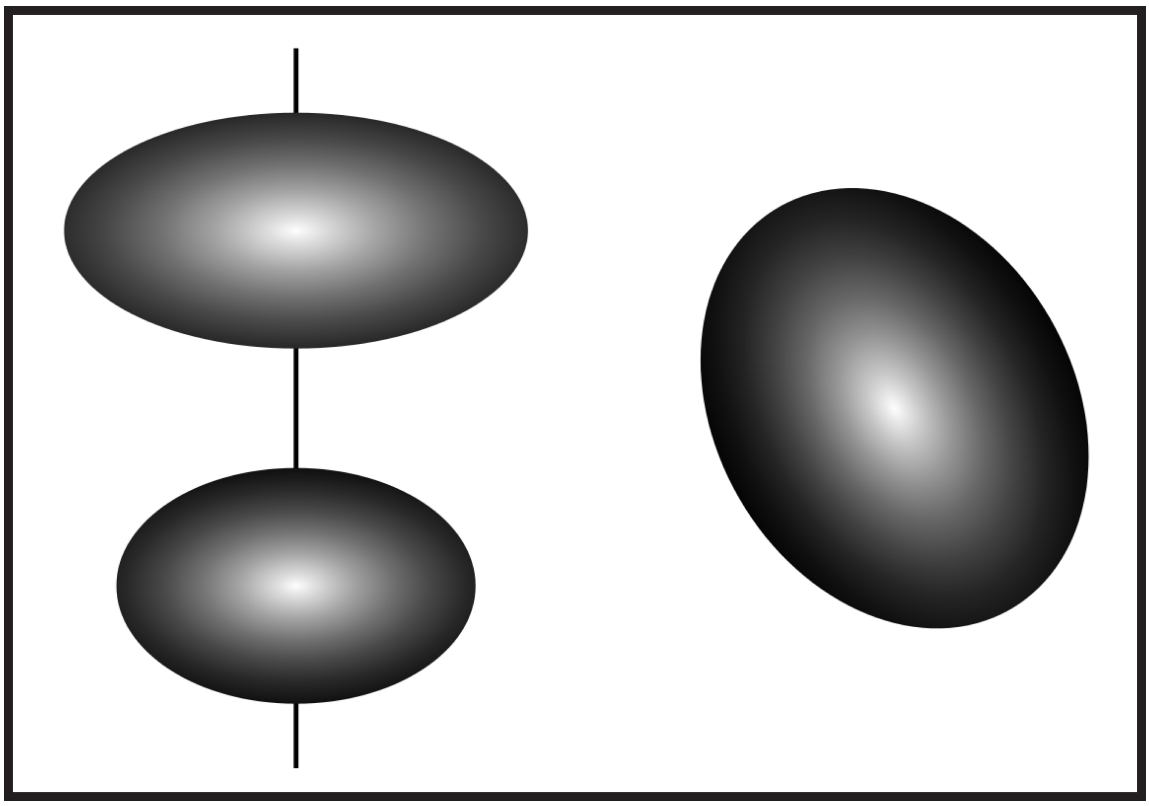

Figure 1.2: A Rotating Haumea, Equatorial View (Left) and Polar View (Right). The Equatorial View Produces a Light Curve, Whereas if Viewed Down the Line of Sight of the Polar Axis, the Presented Area Would Stay Constant and No Light Curve Would Be Produced (Adapted from `http://en.wikipedia.org/wiki/Haumea#/media/File:Haumea.svg`).

Haumea's magnitude over time exhibits a light curve, shown in Figure 1.1. R06 measured a double-peaked light curve for Haumea, from which they calculated its rotational period to be 3.9154 hours. This is the shortest rotation period measured for any Trans-Neptunian Body (TNO) (Sheppard & Jewitt 2002, 2004), as well as for any solar system body larger than 100 km in size (Pravec et al. 2002). The double-peaked light curve also suggests an oblong, ellipsoidal shape, because as an ellipsoid rotates it changes the amount of light-reflecting surface area, thereby changing its magnitude (Figure 1.2).

In working out Haumea's exact dimensions, two primary shapes are considered. The first is an ellipsoid of the type just described, a non-axially symmetric shape

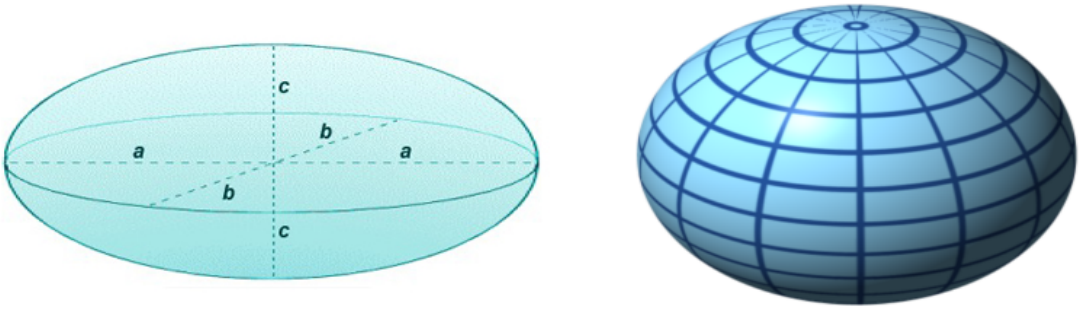

(a) Jacobi Ellipsoid: $a > b > c$. (b) Maclaurin Spheroid: $a = b > c$.

Figure 1.3: Two Possible Shapes of Haumea. (Figure (a) Is Adapted from `http://mathground.net/ellipsoid/`, and Figure (b) Is Adapted from `https://sciencequestionswithchris.wordpress.com/`.)

more accurately referred to as a triaxial ellipsoid. If an ellipsoid's three semimajor axes or radii are referred to as a, b, and c, then a triaxial ellipsoid is defined as one in which $a > b > c$. A special type of triaxial ellipsoid whose surface is in hydrostatic equilibrium is more technically called a Jacobi ellipsoid, shown in Figure 1.3(a). The other shape considered in modeling Haumea is an oblate spheroid, in which the equatorial axes a and b are equal and greater than c, the polar axis. A type of oblate spheroid whose surface is in hydrostatic equilibrium is known as a Maclaurin spheroid, one of which is shown in Figure 1.3(b). A rotating Jacobi ellipsoid will produce the double peaked light curve but a Maclaurin spheroid will not, unless there are albedo changes on the surface. Because of the symmetry displayed by Haumea's light curve, the ellipsoid shape is favored in the models. It is unlikely that Haumea is a binary because its light curve amplitude is too small and its angular velocity too high (R06). A binary configuration would also require an unrealistically high density (Lacerda & Jewitt 2007). Details of how Haumea's dimensions have been determined are covered toward the end of this chapter in Section 1.4.

1.2.2 Surface Properties

Haumea is one of the most reflective TNOs, with an albedo anywhere from 0.6 to 0.85, depending on its surface scattering properties (Lellouch et al. 2010). Trujillo et al. (2007) found that water ice dominates Haumea's spectrum, and that its surface is a close fit to a mixture of roughly 81% crystalline water ice and 19% kaolinite (Figure 1.4). The kaolinite in this case is acting as a blueish neutral absorber. Pinilla-Alonso et al. (2009) found the most probable surface composition to be an intimate mixture of half crystalline and half amorphous water ice (Figure 1.5). Any other component would comprise less than 10% of the surface. There is a particular absorption feature at 1.65 μm which is found only in crystalline water ice and not in amorphous or high-temperature crystalline ice. This poses a mystery, as crystalline water ice is unstable on 10-Myr timescales, due to cosmic and solar ray fluxes and also by the fact that amorphous ice is favored by the extremely cold temperatures found in that part of the solar system (T07). Despite this, crystalline H_2O ice has been reported for many other solar system bodies, including Charon, Quaoar, Orcus, and many icy outer satellites (T07). The rate of micrometeorite impacts in the outer solar system may cause annealing of the ice, adequately enough to explain the amount of crystalline water ice seen (Porter et al. 2010). Haumea's surface composition is unusual, though, since nearly all Pluto-size KBOs have methane-rich surfaces (Lacerda et al. 2008). Trujillo et al. found no methane ice, and with their resolution, no more than 10% of Haumea's surface could be covered with methane ice without detection. There has also been no evidence for N_2 ice, which has an absorption band at 2.15 μm (Lacerda et al. 2008).

Due to the global H_2O coverage and a potentially additional blueish component, Haumea displays an optically blue color (Tegler et al. 2007). As discussed above,

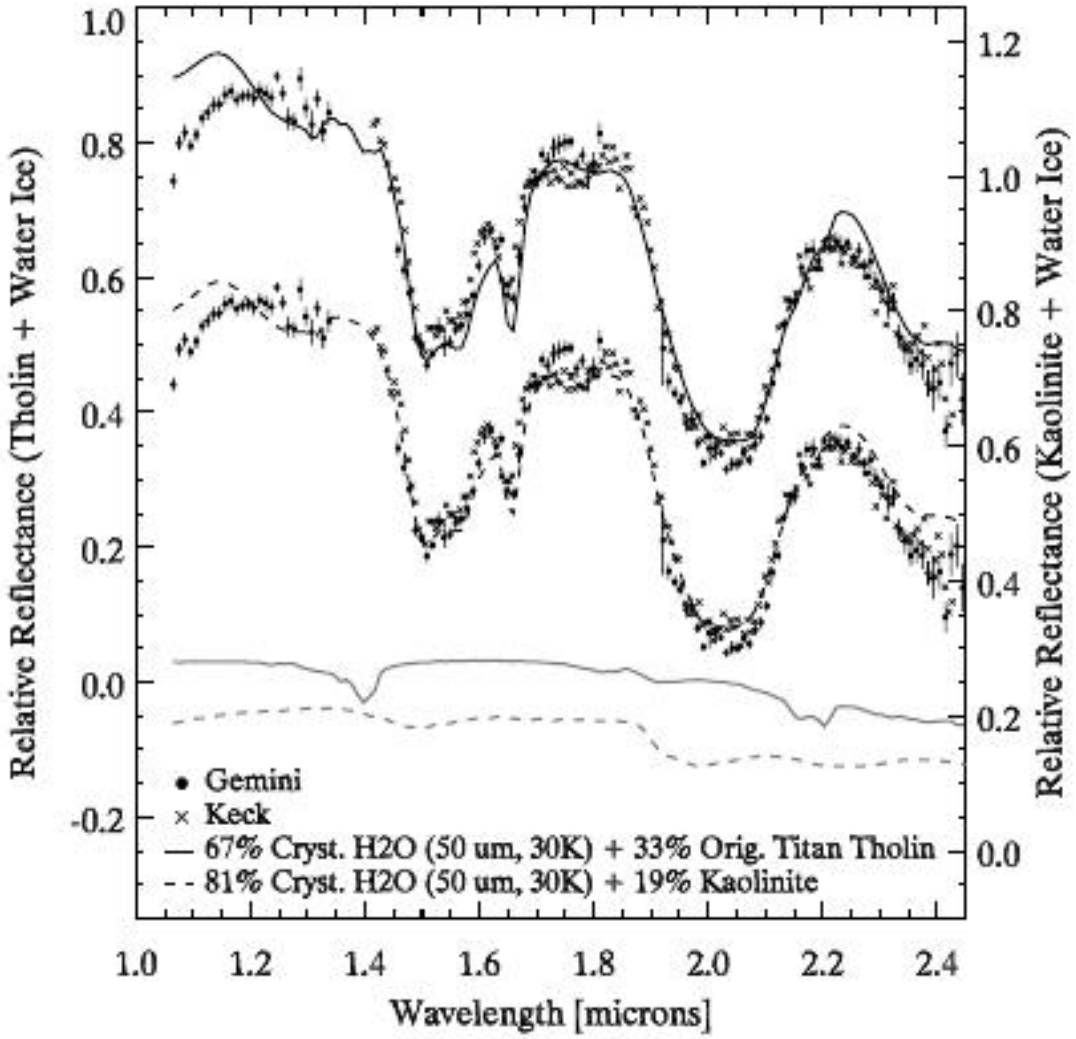

Figure 1.4: This Spectrum of Haumea Shows a Good Fit with Material Consisting Largely of Crystalline Water Ice with Kaolinite Mixed in (Trujillo et al. 2007).

Haumea displays a two-peaked light curve; however, the two peaks are not equal, as the second peak is smaller by roughly 0.08 mag (Lacerda et al. 2008). This implies a spot on Haumea's surface that is darker than the rest. This asymmetry shown in Figure 1.6 is difficult to produce with a symmetric ellipsoid. Figure 1.6 shows that the asymmetry is less at red (J-band) wavelengths, hence the patch is also redder than elsewhere on the surface. Thus, Lacerda et al. (2008) propose a Dark Red Spot (DRS) on Haumea. According to their light curve, the DRS must lie in a leading quadrant

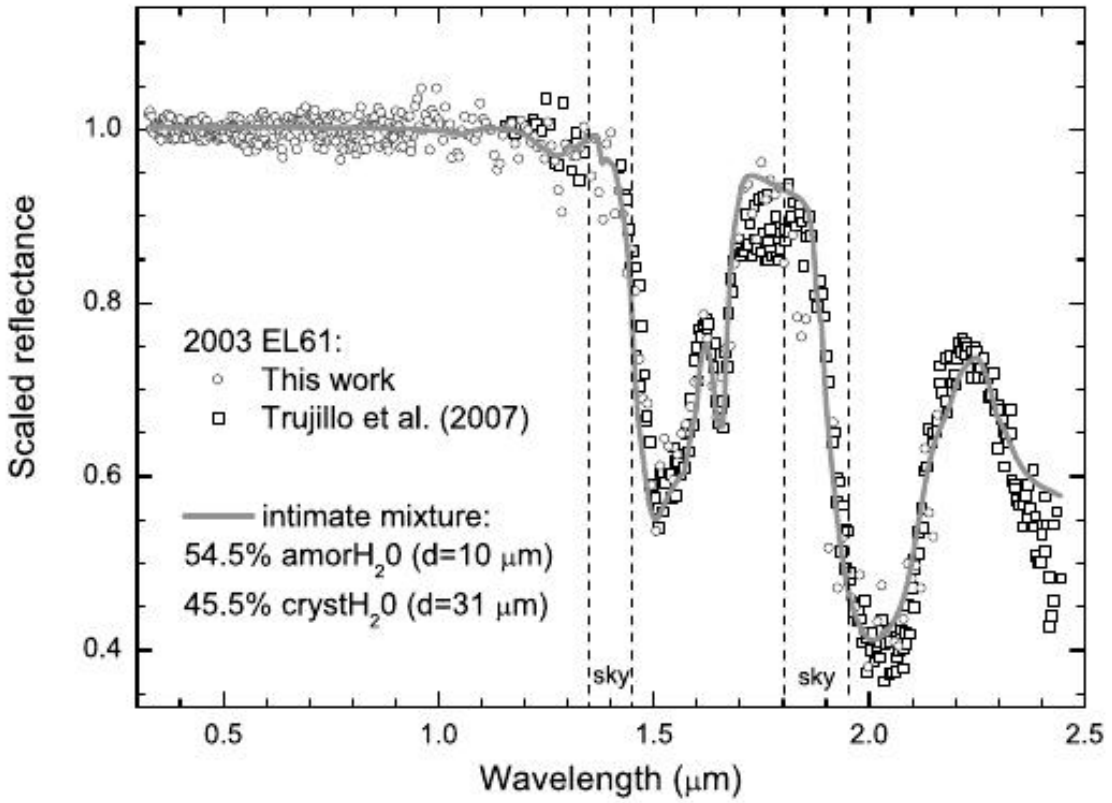

Figure 1.5: Haumea's Spectrum Is Well Fit By an Intimate Mixture of Crystalline and Amorphous Water Ice (Pinilla-Alonso 2009).

with respect to both Haumea's rotation and one of its semimajor axes (Lacerda et al. 2008), as shown in Figure 1.7. Thermal mid-infrared lightcurve observations by both Lellouch et al. (2007) and Lockwood et al. (2014) were unable to confirm the existence of this spot. The visible data set of Lockwood et al. (2014) does agree with a Dark Red Spot though. Constraints on the size of the DRS are broad: it may be as small as a few percent of the maximum cross sectional area of Haumea if it is 20% as reflective as the rest of the surface; alternatively, if it is 5% less reflective than the rest of the surface, it may cover an entire hemisphere (Lacerda 2010). Most probably, according to Lacerda (2010), the size is between 20–60% of Haumea's maximum cross sectional area, with an albedo of 0.55 – 0.65. This albedo would be consistent with Eris and Makemake, as well as the bright regions on Pluto and Iapetus. It would be

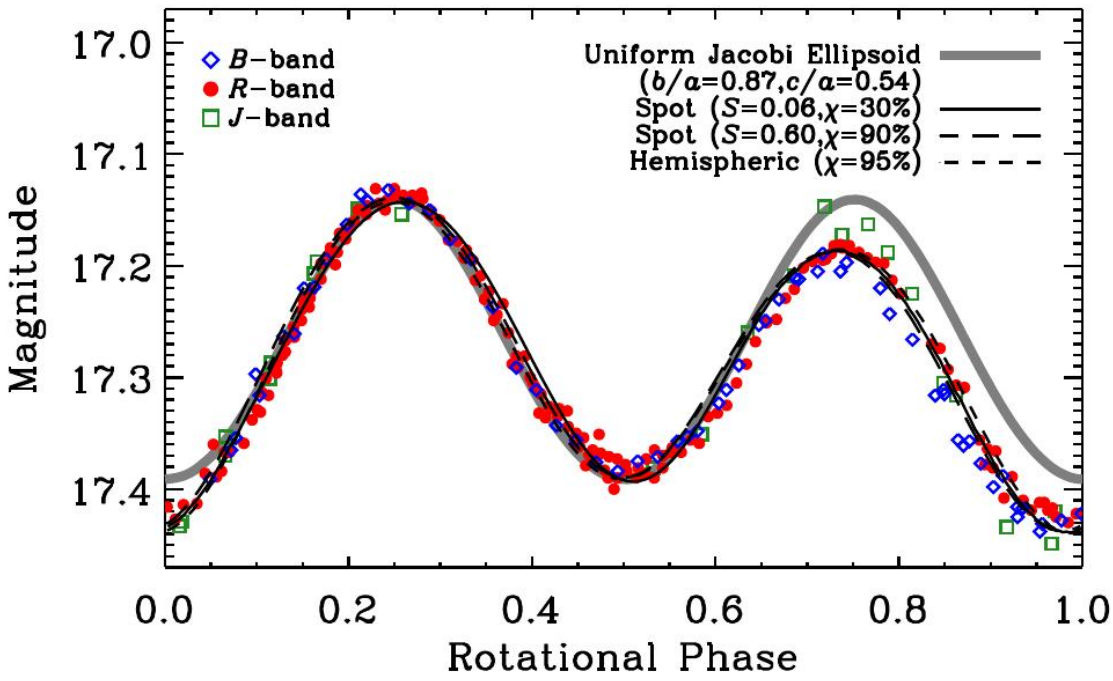

Figure 1.6: Light Curves for Haumea, Superimposed with Four Different Model Curves. If Haumea Were a Symmetric, Uniform Albedo Ellipsoid with the Axial Ratios $p = b/a = 0.87$ and $q = c/a = 0.54$, the Solid Line Would Be the Resultant Curve. The Remaining Three Fit Lines Correspond to a Dark Spot (Located on the Equator and Leading a by 45°), of Varying Size (S) and Albedo (χ) as Follows: 6% of the Maximum Cross-Sectional Area and 30% Albedo of the Surrounding Terrain; 60% of the Maximum Cross Section and 90% the Albedo of the Surroundings; and Covering One Entire Hemisphere (Largest Cross Section) With 95% Albedo of the Rest of the Surface (Lacerda et al. 2008).

inconsistent with the albedos of Charon, Phoebe, Chiron, Pholus, and darker regions on Pluto's surface (Lacerda 2010). Lacerda (2010) rules out the possibility of this spot being due to surface relief, such as a mountain or valley, and he also speculates that the DRS may be richer in crystalline H_2O ice than the rest of the surface.

In their thermal lightcurve analysis, Lellouch et al. (2010) point out that the large amplitude of the lightcurve implies a low thermal inertia, according to their surface scattering models. If this is the case, Haumea may have a porous surface, inconsistent with a compact water ice surface. The possibility of a loose regolith covering the surface may be due to past collision events (Lellouch et al. 2010).

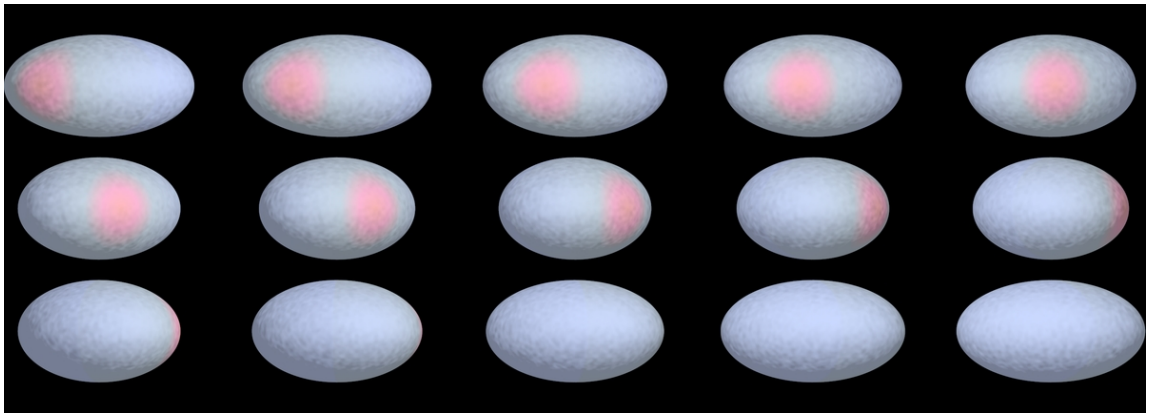

Figure 1.7: Computer-Modeled Images Showing the Dark Red Spot's Location on Haumea as It Rotates (Adapted from `http://www.space.com/7289-strange-dwarf-planet-red-spot.html`).

1.2.3 Satellites

In 2005, a team using the Keck II Telescope discovered two satellites around Haumea (Brown et al. 2006). This makes the Haumea system the only known ternary or higher system in the Kuiper Belt, aside from Pluto (Weaver et al. 2005). The larger outer satellite, named Hi'iaka, orbits with a period of 49.46 days, with a semimajor axis of 49,880 km. The inner smaller satellite is named Namaka, and it has a semimajor axis of 25,657 km with an orbital period of 18.28 days (RB09). Haumea rotates more than 100 times during a single orbit of Namaka (RB09). The orbits of the satellites are very close to an 8:3 resonance, and RB09 surmise that the moons have possibly passed through a 3:1 resonance from time to time. Orbital analysis allows a calculation of the masses of Haumea and its moons, which are reported in RB09 as 4.006×10^{21} kg for Haumea, 1.79×10^{19} kg for Hi'iaka, and 1.79×10^{18} kg for Namaka. This gives Haumea a mass of roughly 32 percent that of Pluto (R06). Hi'iaka is ten times more massive than Namaka and is massive enough that its orbital plane is expected to be coincident with Haumea's equatorial plane (RB09). Hi'iaka's orbital plane is inclined only 4° to our line of sight, and this gives a likely aspect angle of

Haumea's rotational axis to be close to 90° (R06). This may be important when calculating the shape of Haumea below.

Haumea's satellites are much fainter when compared to their primary than any other known KBO satellites (Brown et al. 2006). Hi'iaka is roughly ten times fainter than Haumea, while Namaka is about 3.7 times fainter than Hi'iaka (RB09). All three have similar spectral (Barkume et al. 2006) and photometric properties (Fraser & Brown 2009). Barkume et al. (2006) obtained a near-IR spectrum of Hi'iaka and found that it shows strong water ice absorption features at 1.5 μm and 2 μm. The features seen are deeper than typically observed on KBOs, so Barkume et al. conclude that Hi'iaka's surface is covered with smooth H_2O ice, and that it is even purer water ice than on Haumea. Dumas et al. (2011) later confirmed a strong 1.65 μm crystalline water ice band in Hi'iaka's spectrum. A grain size of 250 μm provides a good model fit to the absorption lines (Barkume et al. 2006). The albedos of Haumea, Hi'iaka, and Namaka should all be similar because of their similar spectral properties, and if both moons have mostly water ice composition, their sizes can be determined. RB09 calculated Hi'iaka's radius to be roughly 160 km, and Namaka's radius to be about 80 km.

1.2.4 Collisional Family

Given Haumea's rapid rotation rate, its anomalously high density for a KBO, and its satellites which display nearly matching surfaces of ice, many suspected that an impact stripping the ice mantle of a proto-Haumea could offer the best explanation to all of these phenomena (Brown et al. 2007). Brown et al. (2007) announced the discovery of a family of KBOs with surface properties nearly identical to that of Haumea and orbital elements which very closely align with Haumea's orbit. When KBOs are graphed with respect to their orbital elements (semimajor axis a, orbital

eccentricity e, and orbital inclination i), those few with optical colors indicative of water ice are found to cluster together, compared to all other KBOs in their survey. They form a unique group with similar surface characteristics and small dynamical dispersion with respect to their orbital elements, clustering very close together in a, e, and i. Amongst the six objects Brown et al. (2007) observed to cluster, the spread in semimajor axes is 2.15 AU, the spread in eccentricities is 0.08, and the spread in orbital inclination is 1.4°. Their conclusion is that these objects, combined with Haumea and its satellites, form a collisional family like those in the asteroid belt, and all came from the same progenitor body, of which Haumea is the primary remnant. An impact which imparted Haumea's rapid spin rate easily could have ejected much of its icy mantle, raising its bulk density and also throwing out many icy fragments, which then became Hi'iaka, Namaka, and the rest of the family. On the basis of orbital parameters, 36 potential candidates eventually were identified, of which 11 are now confirmed to have the icy surfaces unique to this family (Carry et al. 2012), each with a diameter between 70 and 365 km (Leinhardt et al. 2010).

This is the first and only collisional family known in the Kuiper Belt (Ragozzine & Brown 2007; hereafter RB07). While the existence of this family seems to fit well into the puzzle about Haumea's past, many more questions arise from studying these fragments. For example, when estimating the amount of mass loss Haumea must have experienced in a collision which could have caused the observed velocity spread in the family, there is a major discrepancy. The total mass of the family members, plus Haumea's satellites, is less than 2% of Haumea's mass and less than 6% of the total amount of ice predicted to have been ejected (Cook et al. 2011). With simulations of thermal evolution, Desch et al. (2009) show that KBOs with a radius in the range of 500 to 1000 km only partially differentiate, so that a thick undifferentiated rock/ice crust can end up overlaying a differentiated icy mantle and rocky core beneath. This

undifferentiated crust would be ejected in a collision event along with much of the icy mantle. Lacking pure ice surfaces, these objects would not have been identified as family members. If such a population were out there, it would make up much of the missing mass. Cook et al. (2011) identify 7 possible candidates for what they term "Black Sheep", family members, and they argue that there may be many other family members that remain to be discovered.

1.3 Theories on Haumea's Origin

Many simulations have been done to constrain what type of impact caused the observed features of Haumea and its collisional family, as well as what the proto-Haumea and the impactor looked like before the collision. Brown et al. (2007) state that if proto-Haumea had a density of 2000 kg m^{-3}, similar to Pluto, Triton, Eris, and Charon (other KBOs of comparable size), if its current density is taken to be 2600 kg m^{-3}, and if it were struck by a small body, then its radius was roughly 830 km, and around 20% of its mass was removed in the collision. Typical orbital velocities in the Kuiper Belt are around 5 km/s, as compared to roughly 20 km/s in the asteroid belt (RB07). Kuiper Belt collisional families therefore may have a wider spread of orbital parameters than do asteroid families. Brown et al. (2007) estimate that if the collision velocity was 3 km/s, then the impactor's radius was 60% of proto-Haumea's. From simulations, Brown et al. (2007) also calculated that ejection velocities of around 400 m/s can explain the observed spread in orbital parameters. Since Haumea is in a slightly different orbit from the other family members and also from where it was assumed to be before the collision, it may have fallen into the 12:7 orbital resonance with Neptune after the collision. This would have increased its eccentricity and changed other orbital parameters to match those of today (Brown et al. 2007).

The probability of a collision in the Kuiper Belt today is so low that the impact most likely occurred much earlier in the solar system's history, when the TNO population was much higher (Morbidelli et al. 2008). RB07 support the idea of an oblique impact, followed by debris disk formation to explain the satellites. According to RB07, a minimum ejection velocity of 150 m/s from a Haumea impact would create a collisional cloud that contains all the known family members. Resonance diffusion causes changes in eccentricity over time, and studies of this process may provide a constraint on the age of the family (Milani & Farinella 1994). RB07 report with 90% confidence from resonance diffusion analysis that the Haumea family is older than 1 Gy, with an age estimate of 3.5±2 Gy. It is likely that the family is not only ancient but also primordial with respect to the age of the solar system (RB07).

While Brown et al. (2007) favored a catastrophic impact, Leinhardt et al. (2010) argue that the velocity dispersion is too small to allow that sort of collision. They claim that a graze and merge impact between two similar sized bodies is the most likely scenario, as it results in the most closely matching orbital parameters for all post-impact objects. In a graze and merge scenario, the impactor hits the target at an oblique angle, separates, and then recollides and merges with the target. The ice mantles would experience severe deformation and subsequently fragment. After the merge, the remnant undergoes solid state differentiation quickly. The satellites and family members would then derive from the icy mantle of the merged, differentiated body. Leinhardt et al. (2010) are able to achieve a close match to Haumea's collisional family with a graze and merge with an impact velocity of 800-900 m/s, if both the impactor and the target were of equal size and density (2000 kg m^{-3}).

Schlichting and Sari (2009) have a different idea for what caused Haumea's collisional family. They propose a double impact event: the first was a giant impact which imparted to Haumea its high angular momentum and ejected a debris disk

which then accreted into a satellite of radius 260 km. This satellite underwent tidal evolution during which its orbit drifted further away from Haumea. The second collision event was between another KBO and the satellite, which subsequently broke apart the satellite and distributed the material into a collisional cloud with a velocity dispersion of around 190 m/s. This model has the benefits of explaining the observed velocity dispersion and the total mass of the family members (including Hi'iaka and Namaka), but it is a little more complex. Schlichting and Sari argue that if the first impact occurred very early on in the Kuiper Belt when it was more crowded and collisions were much more likely, then the second collision could have occurred much later, when the neighborhood was emptier. This could allow the collisional fragments to spread out while retaining similar orbital parameters.

Simulations performed by Cook et al. (2011) led them to propose the idea of the Black Sheep and a partially undifferentiated proto-Haumea. According to their simulations, the target had a radius of 850 km and the impactor a radius of 450 km, both with equal densities (2000 kg m^{-3}). Due to these sizes, the target (proto-Haumea) will have fully differentiated after around 1 Gyr (almost fully completing differentiation after only 70 Myr), while the impactor underwent differentiation within 600 Myr of formation (Cook et al. 2011). Their target had a rocky core mass of 3.21×10^{21} kg, an icy mantle mass of 1.05×10^{21} kg, and a rock/ice outer crust mass of 0.87×10^{21} kg. The impactor was given a rocky core mass of 0.37×10^{21} kg, an ice mantle mass of 0.12×10^{21} kg, and an outer crust mass of 0.27×10^{21} kg. After the merge, the total ice mass would be 1.18×10^{21} kg and the total rock/ice crust mass 1.14×10^{21} kg. Most importantly, the total rock mass would have been 3.58×10^{21} kg, which is close to the mass of rock inferred to be in Haumea today (Cook et al. 2011). In the simulations done in my project, I will more accurately constrain the most likely core mass for comparison.

Further understanding Haumea and its collisional family will provide many important insights. First, it will help us understand the surface processes on KBOs. Why is there so much crystalline water ice and little or no reddening or surface darkening, as expected for surfaces in the outer solar system (RB07)? It may also help us constrain number densities in the Kuiper Belt in the past, in studying when in the past such a collision was probable (RB07). Finally, understanding details of proto-Haumea's differentiation and combining this with studies of its surface, moons, and collisional family objects, may possibly be our best chance at seeing the inside of a KBO.

1.4 The Shape of Haumea

In analyzing an object's light curve such as Haumea's, there are a few assumptions that are used to derive the object's dimensions. The first case is if Haumea is assumed to have dimensions of a Jacobi ellipsoid. If the angle between our line of sight and Haumea's rotational axis, defined as the aspect angle ϕ, were 90°, then as Haumea rotates, the peak magnitude will occur when we see it displaying the size of its longest axis, when it is showing its maximum cross-sectional area. So the maximum magnitude corresponds to the a axis, while the minimum magnitude corresponds to the b axis. Relating the equatorial radii a and b with the change in apparent magnitude, we have

$$m_1 - m_2 = 2.5 \log \frac{a}{b}. \tag{1.2}$$

Then the peak-to-peak amplitude $m_1 - m_2 = \Delta m$ of the light curve (0.28 mag according to R06) gives a lower bound for a/b:

$$\frac{a}{b} \geq 10^{0.4\Delta m}. \tag{1.3}$$

The inequality in the above equation is dependent on the aspect angle, ϕ. For lower angles of ϕ, we would be looking at Haumea's axis closer to head on, there

would be less magnitude variation from a changing surface area, and so a/b would have to be larger to account for this. If ϕ is 90° then a/b is minimized, and both sides of Equation 1.3 are then equal.

Once the ratio a/b is obtained, the next step is to consult the equation defining equilibrium constraints for Jacobi ellipsoids,

$$\frac{\omega^2}{\pi G\rho} = 2abc \int_0^\infty \frac{u\ du}{[(a^2+u)(b^2+u)(c^2+u)]^{1/2}(a^2+u)(b^2+u)}. \tag{1.4}$$

Chandrasekhar (1987) used this equation to constrain the axial ratios $p = b/a$ and $q = c/a$ for given angular velocity ω and density ρ.

Combining the above two equations with the ellipsoidal mass-volume relationship,

$$M = \frac{4}{3}\pi abc\rho, \tag{1.5}$$

we now have three equations and three unknowns (a, b, and c) for a given ω and ρ.

Using the rotation period of 3.9154 ± 0.0002 hours measured by R06, the angular velocity ω must be $(2\pi)/(3.9154\text{ hr}) \times (1\text{ hr})/(3600\text{ s}) = 0.000446$ rad/s. As for the mass M, Ragozzine and Brown (2009) calculated Haumea's mass to be 4.022×10^{21} kg, using observations of its satellites' orbits. Haumea's bulk density is taken from Lockwood et al. (2014) to be 2600 kg m^{-3}.

To address the dependence of the shape on the aspect angle ϕ, Binzel et al. (1989) describe a relationship between ϕ, the axial ratios, and Δm:

$$\Delta m = 2.5\Big[log\Big(\frac{a}{b}\Big) - log\Big(\frac{r_1}{r_2}\Big)\Big], \tag{1.6}$$

where

$$r_1 = \sqrt{a^2\cos^2\phi + c^2\sin^2\phi} \tag{1.7}$$

and

$$r_2 = \sqrt{b^2\cos^2\phi + c^2\sin^2\phi}. \tag{1.8}$$

Another possibility is that Haumea has taken the shape of a Maclaurin spheroid, so that $a = b > c$. If this is the case, then instead of Equation 1.4, Maclaurin's formula (Chandrasekhar 1987) is consulted:

$$\frac{\omega^2}{\pi G\rho} = \frac{\sqrt{1-e^2}}{e^3} 2(3-2e^2)\sin^{-1} e - \frac{6}{e^2}(1-e^2). \tag{1.9}$$

This equation relates the spheroid's eccentricity $e = [1-q^2]^{1/2}$ with angular velocity and density, where $q = c/a$ as before, and $p = b/a \equiv 1$. If Haumea exists in this type of shape, then Δm will only be due to surface albedo heterogeneities and not to the body's shape, so that Equation 1.3 is not valid.

If Haumea were a Maclaurin spheroid, then equilibrium requires its density to be greater than 2530 kg m^{-3}, via Maclaurin's formula (R06). At lower densities, only a Jacobi ellipsoid shape is stable, and since it is expected that KBOs have densities no greater than that of our Moon (3300 kg m^{-3}), the range of possible densities for Haumea is narrow (R06). R06 used the Jacobi and Maclaurin relations (Equations 1.4 and 1.9) to calculate four possible shapes of Haumea: two possible Jacobi ellipsoids at differing aspect angles, and two possible Maclaurin spheroids. Lacerda and Jewitt (2007) used a Lambert scattering law in their modeling of the light curve, which they took as representative of "icy-type" surfaces, to calculate a bulk density of 2551 kg m^{-3}. Lellouch et al. (2010) then used thermal lightcurve observations to calculate two different ellipsoidal shapes, one corresponding to a Lambert scattering law and the other corresponding to a Lommel-Seeliger law. The best fit they found to be with the Lommel-Seeliger law describing surface scattering. Lockwood et al. (2014) subsequently obtained the first light curve of Haumea apart from its satellites, both optical and thermal, and they confirmed Lellouch et al.'s previous shape calculation. Specifically, they derived axial ratios of $b/a = 0.80$ and $c/a = 0.52$, along with an overall density of 2600 kg m^{-3}. We used this value for bulk density in our models,

and the dimensions of Haumea according to these values would then be $a = 960$ km, $b = 770$ km, and $c = 495$ km. To investigate the most likely equilibrium shape in our models with respect to gravity and rotation, we consider as inputs five possible shapes: the four Rabinowitz shape models and the shape confirmed by Lellouch et al. (2010) and Lockwood et al. (2014). These five shapes are listed in Table 1.1.

Shape	a (km)	b (km)	c (km)	p	q	ϕ	Reference
1	980	759	498	0.77	0.51	90°	R06
2	1250	540	430	0.43	0.34	$> 47°$	R06
3	870	870	500	1	0.57	n/a	R06
4	750	750	524	1	0.70	n/a	R06
5	960	770	495	0.80	0.52	90°	Lockwood et al. 2014

Table 1.1: Five Different Shapes for Haumea Used in This Work.

In calculating shape 1, R06 assumed that Haumea's rotational axis is aligned with the orbital plane of Hi'iaka. This would give a strong constraint on the aspect angle ϕ. Since Hi'iaka's orbit is inclined to our line of sight by 4° (R06), this means the aspect angle ϕ must be 86°. At this angle, there is minimal error in assuming that $\phi = 90°$. Then there is no angular lessening of the magnitude of the equatorial radii. Therefore the ratio $a/b = 1/p$ is precisely equal to $10^{0.4\Delta m}$ (Equation 1.3), which is 1.294, so that $p = 0.773$ and $a = 1.294b$. Using the mass-volume relationship (Equation 1.5) and taking the bulk density to be 2600 kg m^{-3}, we then find that $c = 2.8426 \times 10^{17} b^{-2}$. Plugging these expressions for a and c into the Jacobi ellipsoid equation (Equation 1.4), gives, according to R06, $(a, b, c) = (980, 759, 498)$ km. Because we are assuming that we are viewing Haumea's equatorial plane nearly edge on in this example, a/b is at a minimum. Thus a will be no less than 980 km, b will be no greater than 759 km,

and c will be no greater than 498 km. This shape is considered by R06 to be the most likely shape for Haumea, and it is very close in dimensions to the shape calculated by Lellouch et al. (2010).

In the unlikely event that we are viewing Haumea's rotation axis closer to pole-on, then its calculated shape must be different. In particular, a/b will have to be larger, to accommodate the fact that the light curve will be shallower with greater aspect angle tilt. According to R06, the upper stability limit for a/b occurs at $\phi = 47°$ and with a density no greater than $\rho = 3340$ kg m^{-3}. If this is the case, then we will find a Jacobi ellipsoid with an upper limit of $a = 1250$ km, a lower limit of $b = 540$ km, and a lower limit for c as 430 km. This leads to $(p, q) = (0.43, 0.34)$, and this is shape 2.

In calculating shapes 3 and 4, now the attention is shifted to whether Haumea could possibly be a Maclaurin spheroid. At Haumea's rotation rate, for a Maclaurin spheroid the lowest the density could possibly be is 2530 kg m^{-3}, for any lower density and the object is unstable and will undergo fission (Farinella et al. 1981). Using this density in Maclaurin's formula (Equation 1.9), $q = 0.58$ is the only solution. Using $a = b$ and the mass-volume relationship, we find the approximate axes for shape 3: $(a, b, c) = (870, 870, 500)$ km.

For shape 4, a Maclaurin spheroid with an upper density limit of 3300 kg m^{-3} (since we are not expecting Haumea to be denser than our Moon), Maclaurin's formula then requires that q take on the value 0.7. With this value and using the method above for shape 3, we find that the axes according to these constraints will be approximately $(a, b, c) = (750, 750, 524)$ km.

Shape 5 was derived by Lellouch et al. (2010) in a similar manner to shape 1 and 2 above by R06. The difference was that Lellouch et al. found the best model fit to the light curve to be a surface described by the Lommel-Seeliger function. They

subsequently updated the axes to be:

$$\begin{aligned} a &= 960 \text{ km} \\ b &= 770 \text{ km} \\ c &= 495 \text{ km}. \end{aligned}$$

The axial ratios for shape 5 are then $(p, q) = (0.80, 0.52)$. Lockwood et al. (2014) obtained the first light curve of Haumea separate from its moons, and they then used their data to confirm these axial dimensions. It is this shape for the outer surface of Haumea that we focus on as the most likely shape.

In summary, we estimate from Haumea's axial dimensions (from the light curve) and mass (from orbital observations of its satellites) that the bulk density is 2600 kg m^{-3} and the axial ratios are $(p, q) = (0.80, 0.52)$. These values seem consistent with Haumea in the shape of a Jacobi ellipsoid, but because of its ice surface, clearly it is not of homogeneous density.

The primary question investigated in this work involves finding the most likely density of Haumea's core. This will then determine the size and shape of the core, which will in turn shed light on the thickness of the ice mantle and its variation throughout the surface, as well as provide constraints on the collision Haumea suffered in the past. Finding the most likely core density will allow a complete determination of the configuration of Haumea as a two-phase body.

With Haumea's backstory and its likely properties discussed, I will next investigate some of the theory of rotating ellipsoids in equilibrium in Chapter 2. In Chapter 3 I will explain the considerations taken in building the code. In Chapter 4, I will then delve into the panoply of results which were obtained and how we used those results to predict Haumea's most likely configuration. Finally, I conclude in Chapter 5 by discussing the most likely configuration of the interior and exterior of Haumea.

Chapter 2

REVIEW OF ELLIPSOIDS

In this chapter, I delve into the theory regarding what shape a rotating fluid object will take in an equilibrium state, where the object's self-gravity and rotation are the only contributing effects. Chandrasekhar (1987) collected and expanded upon much of this theory, and much of his work is paraphrased and fleshed out in this chapter. It should be kept in mind that ultimately none of the following equations can directly apply to Haumea, since they apply exclusively to homogeneous bodies and Haumea is being treated in this work as a two-phase body. However, much insight may come from examining the possibilities for homogeneous bodies.

2.1 The Case for an Equipotential Shape

As determined from its light curve, Haumea is probably oblong in shape and not axially symmetric. It is probably a Jacobi ellipsoid (a triaxial ellipsoid in hydrostatic equilibrium), similar to a flattened football. When a homogeneous spheroid is set rotating, then for a given mass, volume, and angular velocity there exists a particular equilibrium spheroidal shape. Because of Haumea's large size, we assume that its outer surface must align with that of a gravitational equipotential.

Though we assume that Haumea is in a state of hydrostatic equilibrium with respect to its outer surface and its core-mantle boundary, this is not assured. Saturn's moon Iapetus, which is just larger than Haumea ($R_{\text{mean}} \approx 736$ km), displays a shape that is extremely out of equilibrium (Thomas et al. 2007). Iapetus has an oblate spheroidal shape that suggests relaxation at a spin rate of around 16 hours,

much larger than its current angular velocity, as it is now tidally locked to Saturn (Thomas et al. 2007). Iapetus has thus retained a shape which it took very early on and it has frozen in that shape, despite being in a very different dynamical situation today (Thomas et al. 2007). Jupiter's moon Callisto also may not be in hydrostatic equilibrium, as it is much larger than Haumea with $R_{\rm mean} = 2410$ km, yet it has only partially differentiated (Anderson et al. 2001). However, the assumption of hydrostatic equilibrium for Haumea may be justified if its strain rates $\dot{\epsilon}$ are significantly fast (i.e., $\dot{\epsilon} \gtrsim 10^{-17}$ s^{-1}, so that $\dot{\epsilon}^{-1} \leq 10^{17}$ s $= 3$ Gyr).

To be more precise about finding what the strain rate $\dot{\epsilon}$ is, if we first take the internal stress σ as proportional to the central pressure P_c inside Haumea, then

$$\sigma \sim P_c = \frac{3}{8\pi}\frac{GM^2}{R^4}, \tag{2.1}$$

where M is Haumea's mass, R is its mean effective radius, and G is the universal gravitational constant. Plugging in the values of each, $M = 4.006\times10^{21}$ kg (Ragozzine & Brown 2009), $R \approx 7.15 \times 10^5$ m (R06), and $G = 6.67 \times 10^{-11}$ N $\cdot$ m^2/kg^2, we then find that $\sigma \approx 5$ MPa. Since viscosity η is described by

$$\eta = \frac{\sigma}{2\dot{\epsilon}}, \tag{2.2}$$

we find that $\dot{\epsilon}$ depends on both σ and η. However, η also depends on temperature. Thomas et al. (1987) describe viscosity with the following formula:

$$\eta(T) = 10^{14}\exp\Big[25\Big(\frac{273}{T} - 1\Big)\Big] \text{ Pa} \cdot \text{s}. \tag{2.3}$$

Though viscosity depends on other factors such as grain size and flow rate (Rubin et al. 2014), we will use Equation 2.3 in the following calculations for strain rate.

At ice's melting point, $T = 273$ K, we find $\eta \sim 10^{14}$ Pa $\cdot$ s. This then yields $\dot{\epsilon} \simeq (5 \times 10^6 \text{ Pa})/(2 \times 10^{14} \text{ Pa} \cdot \text{s}) = 2.5 \times 10^{-8}$ s^{-1}, an extremely fast strain rate

as expected. Of course, at $T \sim 40$ K, we may have an effectively infinitely large viscosity, which implies $\dot{\epsilon} \simeq 0$ Pa $\cdot$ s, and thus there would be no flow. Somewhere in between these two temperature extremes, there is a temperature (~ 160 K) for which $\eta = 3.5 \times 10^{21}$ Pa$\cdot$s. This is the critical viscosity below which convective overturn can effectively operate within a Charon-like body (Rubin et al. 2014). At this viscosity, $\dot{\epsilon} \sim 7 \times 10^{-16}$ s^{-1}, which allows flow on timescales of $\dot{\epsilon}^{-1} \sim 1.4 \times 10^{15}$ s ~ 45 Myr. For flow to proceed on the order of 3 Gyr ($\dot{\epsilon} = 10^{-17}$ s^{-1} as discussed above), a viscosity no greater than 2.5×10^{23} Pa $\cdot$ s is needed, which occurs at a temperature of ~ 150 K. Using the same argument yet again, a temperature of ~ 170 K is critical to flow on the order of 10 Myr.

This argument brackets the temperatures needed within Haumea for convective flow necessary to achieve hydrostatic equilibrium to the range 150 – 170 K. However, when considering Haumea's origin, it has experienced significant heating over its lifetime. It originated as the core of a larger progenitor body, at the time of impact it probably experienced temperatures $\gg 200$ K or more, and then it stayed hot for more than 10 Myr (Desch & Neveu 2015). Therefore Haumea would have experienced flow on short timescales, and thus it would have assumed a state of hydrostatic equilibrium.

2.2 Uniform Density Case

Isaac Newton, in his Principia Mathematica (1687), was the first to attempt a theory of a rotating object's shape, and the main subject of his theory was the Earth. Newton predicted that if the Earth were a homogeneous body of uniform density, then its shape would be flattened at the poles due to a larger centrifugal force at the equator exerting a larger outward force. This oblateness of the Earth was confirmed in 1738 when Maupertuis and Clairaut took geodetic measurements in extreme northern Lapland (Chandrasekhar 1987).

A few years later, in 1742, Colin Maclaurin expanded on the oblateness of homogeneous spheroids, and the culmination of his work is known as Maclaurin's formula. The three axes of a spheroid (or ellipsoid) will be referred to often as a, b, and c. Let i be an axial index ranging from 1 to 3 so that $a_1 = a$, $a_2 = b$, and $a_3 = c$. (These are how the axes will in general be referred to in this chapter, but I will make use of both conventions.) Maclaurin's formula states the following:

$$\frac{\omega^2}{\pi G\rho} = \frac{\sqrt{1-e^2}}{e^3} 2(3-2e^2)\sin^{-1} e - \frac{6}{e^2}(1-e^2), \tag{2.4}$$

where ω is the angular velocity, ρ is the bulk density, and $e = [1-(a_3^2/a_1^2)]^{1/2}$ is the eccentricity of the meridional (polar, a-c plane) cross section. Oblate spheroids, which are defined by $a = b > c$, are known also as Maclaurin spheroids if they are in hydrostatic equilibrium. This equation exclusively applies to Maclaurin spheroids. (The derivation of Maclaurin's formula is shown in Appendix A.)

In 1834, Carl Gustav Jacob Jacobi argued that if a hole were drilled through each axis of a spheroid and each were filled with fluid, then the weights of each fluid column would be equal. He found that if $a_1 \neq a_2 \neq a_3$ (in other words, if we had an ellipsoidal shape rather than a strictly spheroidal shape), then the relationship between the axes, the body's angular velocity, and the density would be

$$\frac{\omega^2}{\pi G\rho} = 2a_1a_2a_3 \int_0^\infty \frac{u\,du}{(a_1^2+u)(a_2^2+u)\Delta}, \tag{2.5}$$

where $\Delta = \sqrt{(a_1^2+u)(a_2^2+u)(a_3^2+u)}$. This equation will be referred to in this work as Jacobi's formula, as it exclusively applies to Jacobi ellipsoids. Jacobi was the first to maintain that an ellipsoid is a possible equilibrium shape for a rotating homogeneous fluid body. Triaxial ellipsoids, in which $a_1 > a_2 > a_3$, are also known as Jacobi ellipsoids if in hydrostatic equilibrium. (The derivation of Jacobi's formula is shown in Appendix B.)

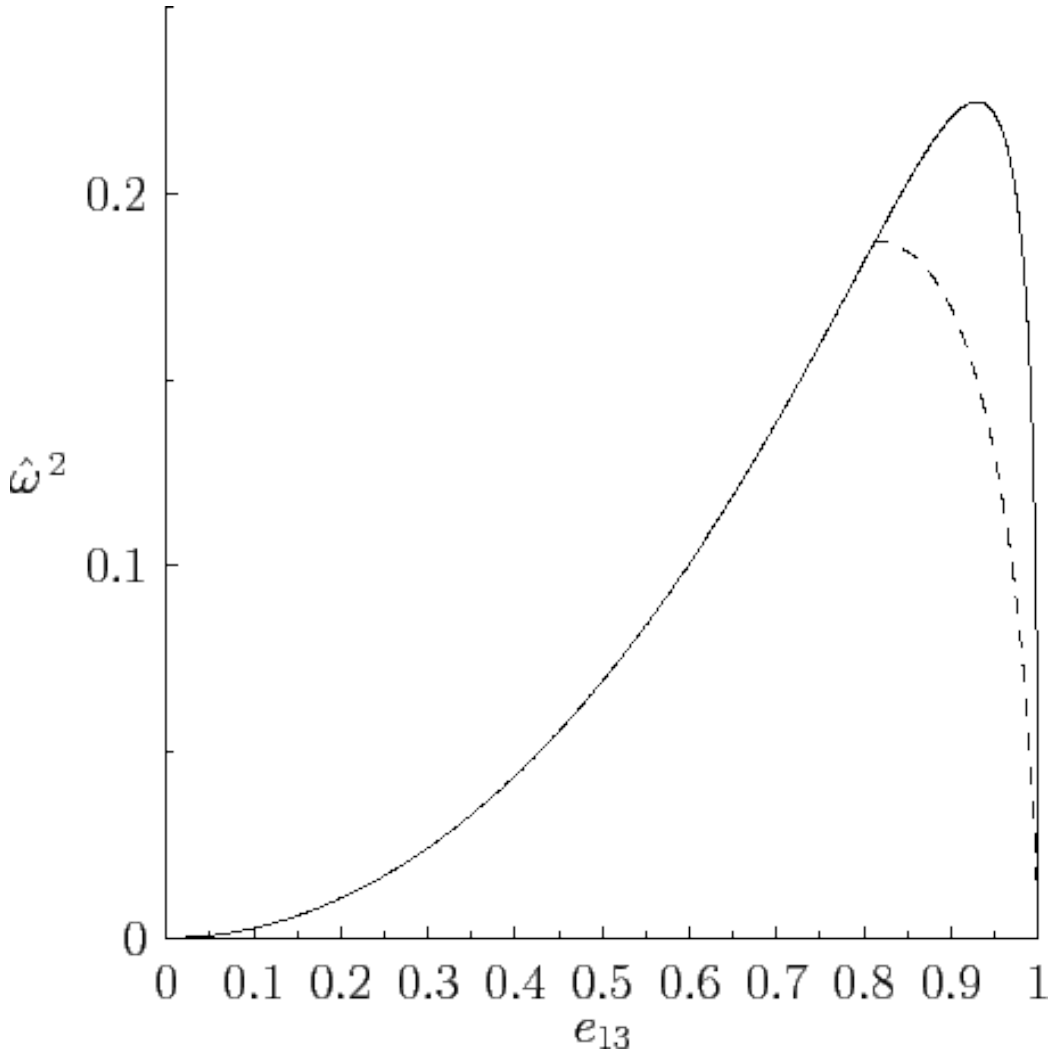

Figure 2.1: The Square of Normalized Angular Velocity, $\hat{\omega}^2$, Versus Polar Cross-Sectional $(a - c)$ Eccentricity e_{13}, for a Maclaurin Spheroid (Solid Line) and a Jacobi Ellipsoid (Dashed Line). (Adapted from `http://farside.ph.utexas.edu/teaching/336L/Fluidhtml/node39.html`.)

In 1842, C.O. Meyer was the first to show a connection between Maclaurin spheroids and Jacobi ellipsoids, in that one shape can transform into the other with a changing angular velocity. Later, in 1846, Joseph Liouville decided to examine the axial ratios' relationship to angular momentum (L), instead of angular velocity. He showed that for Maclaurin spheroids, L can range from 0 to ∞. But Jacobi ellipsoids are only possible as equilibrium shapes above a critical value of L (Chandrasekhar 1987).

The relationship between Maclaurin spheroids and Jacobi ellipsoids is illustrated in Figure 2.1. If we define $\omega^2/(\pi G\rho) = \hat{\omega}^2$ as normalized angular velocity (since $(\pi G\rho)^{1/2}$ has angular velocity-equivalent units of s^{-1}), Figure 2.1 shows $\hat{\omega}^2$ versus the eccentricity e_{13} in the polar $(a - c)$ direction. This graph can be interpreted as follows: when a homogeneous fluid sphere ($e_{13} = 0$) is set rotating, it soon takes on an oblateness ($e_{13} > 0$) and becomes a Maclaurin spheroid. This oblateness increases for increasing angular velocity, so that the Maclaurin spheroid will flatten out. If the spin rate continues to increase beyond a certain point ($\hat{\omega}^2 = 0.187$), then if there is any dissipative mechanism such as viscosity or internal friction, the Maclaurin spheroid shape becomes dynamically unstable. The body will then evolve into a Jacobi ellipsoid as it grows equatorial bulges (the a axis) and its spin rate will slow (Tassoul 1978). The solid line in Figure 2.1 represents the sequence of polar cross-sectional shapes that a Maclaurin spheroid will take with increasing spin, while the dashed line represents the changing polar cross sections of a Jacobi ellipsoid. The deformation into the Jacobi ellipsoid lowers the rotational kinetic energy and increases the gravitational potential energy. The loss in kinetic energy is greater than the gain in potential energy, and this is the cause of the spheroid's instability (Binney & Tremaine 2008). The Jacobi ellipsoid shape is the lower energy configuration at these spin rates. If no dissipative mechanisms are present when the body exceeds the transformation spin rate, then as can be seen from the rest of the solid line in Figure 2.1, the object will remain a Maclaurin spheroid and flatten further until it reaches a maximum angular velocity. It will then slow its spin while it continues to flatten.

In his treatise on ellipsoidal figures of equilibrium, Chandrasekhar (1987) also addresses Maclaurin's Theorem, which deals with gravitational potentials of nested ellipsoids. First, two definitions of nested ellipsoids must be made. Two ellipsoids that have identical axial ratios (i.e. are geometrically similar) and which share the

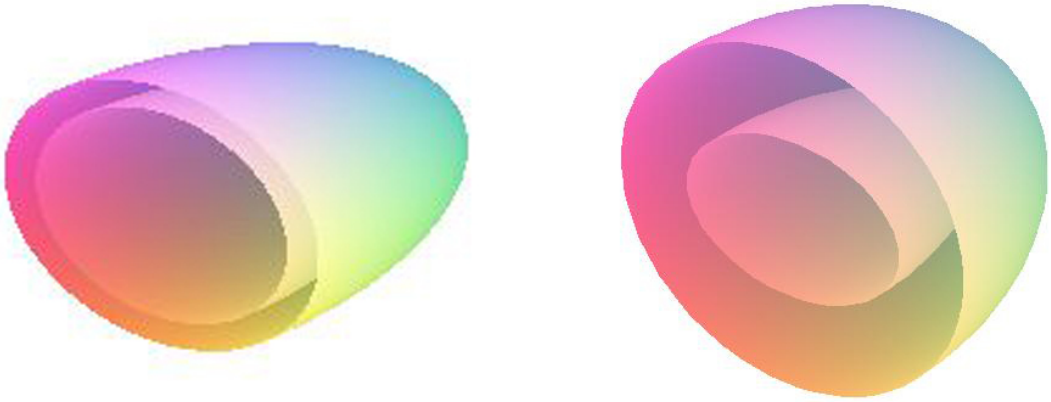

(a) Homeoidal Ellipsoids, Also Known as a Homeoid.

(b) Confocal Ellipsoids, Also Known as a Focaloid.

Figure 2.2: Two Different Ellipsoidal Configurations. Homeoidal Ellipsoids Are Geometrically Similar, and Confocal Ellipsoids Have the Same Foci. (Figure (a) Adapted from `http://en.wikipedia.org/wiki/Homoeoid#/media/File:Homoeoid3d.jpg`, Figure (b) Adapted from `http://en.wikipedia.org/wiki/Focaloid#/media/File:Focaloid3d.jpg`.)

same center are defined as homeoidal ellipsoids. The shape described by the space between them is called a homeoid, shown in Figure 2.2(a). If two concentric ellipsoids instead share the same foci, they will not be geometrically similar. Such ellipsoids are defined as confocal ellipsoids. The space between two confocal ellipsoids is called a focaloid, shown in Figure 2.2(b). It is the confocal ellipsoids to which Maclaurin's Theorem applies.

Maclaurin's Theorem states that the gravitational attraction on a point external to two nested confocal ellipsoids as in Figure 2.2(b) is in the same direction for both ellipsoids, as well as proportional to both masses. This theorem could make it difficult to detect Haumea's internal structure with a spacecraft flyby through purely gravitational means, as it says that an inner ellipsoid which is confocal to the outer surface will have its true shape masked. Fortunately, the method we have

implemented considers every possible shape of two nested ellipsoids, of which the confocal case is just one.

While the possible outer surface dimensions of Haumea have been calculated via the Jacobi formula (for ellipsoids of uniform density) and the Maclaurin formula (for homogeneous spheroids), our model sets up Haumea as a heterogeneous body with a dense rocky core and a less dense icy mantle. If the silicate fraction ends up being high enough, these approximations will still be valid.

2.3 Nonuniform Density Case

Haumea is being modeled in this work as a heterogeneous ellipsoid, a two phase ellipsoid with a mantle of ice and a core composed of some silicate rock. This will look like a higher density ellipsoid nested inside a lower density ellipsoid. Since our model of Haumea has nonuniform density, the ellipsoid relationships above may not be directly applicable. If we find that the bulk of Haumea is rock, though, with only a small amount of ice, then it may yet be treated as a roughly homogeneous object.

There is also a second constraint: the core-mantle boundary (CMB) must be an equipotential. We expect the CMB to conform to an equipotential surface just as we expect the same of Haumea's outer surface. Modeling the size and shape of the core is crucial to understanding Haumea's interior. If the CMB is not an equipotential, then a baroclinicity must exist at the CMB that will drive vortical flows in the ice. In other words, if any part of the CMB surface is not level with the local equipotential surface, it is expected to be unstable and to flow so that it becomes level.

Since Haumea is in hydrostatic equilibrium, it follows that the pressure gradient ∇P is parallel to $\nabla \Phi$, the effective gravitational force vector. But the density gradient $\nabla \rho$ is normal to the CMB because it is a surface of sharp density change. Therefore,

if the CMB is not an equipotential, then $\nabla\Phi \times \nabla P \neq 0$, from which it follows that

$$\frac{d\vec{\Omega}}{dt} = \frac{1}{\rho^2}(\nabla\rho \times \nabla P) \neq 0, \tag{2.6}$$

where $\vec{\Omega}$ is the vorticity (Holton 1992). So the CMB not coinciding with an equipotential would generate vorticity in the ice and rock at the boundary and the energy would dissipate until the CMB aligned with an equipotential surface.

Whether or not the CMB can retain topography is unknown, but the timescale over which the flow may happen is probably very short. The viscosity and timescale of CMB adjustment in Haumea would be extremely temperature dependent. If the temperature is not high enough at the CMB presently to allow for flow, it would have been high enough after the impact that Haumea underwent, as discussed earlier in Section 2.1. The relaxation timescale then is expected to have been short enough and the viscosity low enough to allow for the CMB to flow and resolve itself to an equipotential.

In summary, we are modeling Haumea's outer surface and CMB surface assuming they are in hydrostatic equilibrium. The timescales upon which each surface will align with an equipotential are expected to be short, at least immediately following the impact that created Haumea.

Chapter 3

METHODS

We have written a code (in Python) to calculate the gravitational potential in a multilayered ellipsoid, with an icy outer layer and a denser rocky core. The way the code works is described through the sequence of this chapter.

3.1 Step 1: Generating Different Core Shapes

We discretize the volume around a two-phase ellipsoid, with a rocky density assigned to the inner ellipsoid and an icy density assigned to the outer ellipsoid. Cells in a three-dimensional grid are populated with mass. A Monte Carlo method is used to randomly generate points in cells that straddle the core-mantle boundary (CMB). The outer surface is assumed to correspond with particular axis ratios given in R06 and Lockwood et al. (2014), and these five outer shapes (listed in Table 1.1) were tested, each with a range of different core densities. For a fixed outer surface shape, different shapes of the core were tested, covering the entire possible range of shapes for triaxial ellipsoids.

The values for axes that we use for the surface of Haumea (i.e. shapes 1 through 5 from Table 1.1) were calculated using either Jacobi's formula (Equation 1.4) or Maclaurin's formula (Equation 1.9). These equations provide an equilibrium restriction for the c (rotational) axis. However, in calculating the core axes a_c, b_c, and c_c, we relax this particular constriction that there must be one and only one value of $q_c = b_c/a_c$ for each value of $p_c = c_c/a_c$. Instead, our calculations of the metric are

tested over every possible combination of p_c and q_c, subject only to the constraint that $0.43 < q_c < p_c$.

Fixed quantities input to the code included axes of the outer surface, as well as the angular velocity of Haumea's spin, equal to 0.000446 rad/s. This corresponds to one rotation every 3.9154 hours, as observed by R06. Also input was the measured mass of Haumea of 4.006×10^{21} kg (Ragozzine & Brown 2009), along with the universal gravitational constant. Additionally, the measured average density of 2600 kg m^{-3} (Lellouch et al. 2010) was input, as well as a core density and a mantle density. The mantle density was kept constant and was assumed to be water ice. For this ice mantle, we exclusively used a density of 935 kg m^{-3} (Rubin et al. 2014), but the core density was tested in the range 2700–3300 kg m^{-3}, at intervals of 100 kg m^{-3}. Each of the quantities just described were held fixed for each run.

The primary variables built into the code were the axes of the core, which determine the core-mantle boundary (CMB). Many different shapes of the core were tested. First a core that is homeoidal in shape to the outer surface was tested for a range of core densities. In this construction, each core axis is a particular fraction of the corresponding outer axis, and this fraction is the same for all axes. A second configuration tested for a range of core densities was for a case in which the core is confocal to the outer surface, so that the CMB surface and the outer surface share the same foci, but are not similar shapes.

Ultimately, the code that was used most frequently set up the CMB axes as follows. When we focus on the simple mass-volume-density relationship that must hold for a two-phase Haumea (dense rocky core surrounded by less dense icy mantle), we find the following:

$$M = \frac{4}{3}\pi a_c b_c c_c \, \rho_{\text{rock}} + \frac{4}{3}\pi(abc - a_c b_c c_c)\rho_{\text{ice}}, \tag{3.1}$$

where a_c, b_c, and c_c are the axes of the core, ρ_{rock} is taken to be the density of the

core, and ρ_{ice} is the density of the mantle. Collecting terms in $a_c b_c c_c$ and rearranging,

$$\frac{M}{(4/3)\pi} = a_c b_c c_c(\rho_{\text{rock}} - \rho_{\text{ice}}) + abc\ \rho_{\text{ice}}. \tag{3.2}$$

If $a_c b_c c_c$ were rewritten in terms of the core axial ratios $p_c = b_c/a_c$ and $q_c = c_c/a_c$, then

$$a_c b_c c_c = a_c^3 p_c q_c \tag{3.3}$$

and

$$a_c^3 p_c q_c = \frac{3M/4\pi - abc\ \rho_{\text{ice}}}{\rho_{\text{rock}} - \rho_{\text{ice}}}. \tag{3.4}$$

Finally, solving for a_c, we end up with the following non-restrictive formula for the longest core axis:

$$a_c = \Big[\frac{1}{p_c q_c(\rho_{\text{rock}} - \rho_{\text{ice}})}\Big(\frac{3M}{4\pi} - abc\ \rho_{\text{ice}}\Big)\Big]^{1/3}. \tag{3.5}$$

This equation was used in our code. We combined it with the expressions $b_c = p_c \times a_c$ and $c_c = q_c \times a_c$ to calculate the full shape of the core.

To visualize the shape of the core changing via the axial ratios, when p of an ellipsoid is changed, it alters the ellipticity of the equatorial plane. When p is 1, the equatorial plane is a circle, and the planet is then an oblate spheroid. As p gets smaller, the equatorial plane narrows to more of a sausage shape at the extreme. Since the ratio q involves an axis coincident with the rotational axis, then as q gets smaller, the entire planet will flatten out from top to bottom. We limited the range of p to [0.43, 1] and the range of q to [p, 1], because this is the range restricted for Jacobi ellipsoids (triaxial ellipsoids in hydrostatic equilibrium), even though we are not restricting the core shapes to Jacobi ellipsoids.

3.2 Step 2: Equipotential Test: the Metric $\mathcal{M}$

The primary goal of this work is to ascertain the density of Haumea's core and the most likely shapes of its core and outer surface. The crux of this problem lies in

the gravitational potential. If Haumea is assumed to be a body in gravitational and rotational equilibrium, then its outer surface should be coincident with an equipotential surface, taking into account both gravity and the centrifugal force, or else the fluid would flow parallel to the surface. The same is also assumed for the core-mantle boundary's shape. What is needed is a way to test whether or not a surface is an equipotential, and if not, how close to an equipotential it is.

If the surface is an equipotential, then the surface normal vector $\vec{n}$ will be parallel to the gravitational acceleration vector $\vec{g}_{\text{eff}} = \vec{g} + \omega^2 r\hat{e}_\rho$, where ω is the angular velocity and $r\hat{e}_\rho$ is the radius perpendicular from the rotation axis. Likewise, the unit vector of the surface normal $\hat{n} = \vec{n}/|\vec{n}|$ should be parallel along the effective gravity unit vector $\hat{g}_{\text{eff}} = \vec{g}_{\text{eff}}/|\vec{g}_{\text{eff}}|$. Therefore, the dot product between these two unit vectors will be 1, and the average of this quantity around each surface is the primary metric we use to test the surface stability.

We define the "metric" $\mathcal{M}$ as the quantity $\hat{n} \cdot \hat{g}_{\text{eff}}$ averaged over the surface (either the outer surface or the CMB):

$$\mathcal{M} \equiv \frac{\oint\limits_S \hat{n} \cdot \hat{g}_{\text{eff}}\, dS}{\oint\limits_S dS}. \tag{3.6}$$

Whichever shape configuration of the core and mantle maximizes $\mathcal{M}$ should be the most stable shape.

3.3 Step 3: Generating Points Along the Surface

The metric $\mathcal{M}$ is calculated using spherical coordinates (r^*, θ, ϕ), where * denotes points on the surface. The code generates points along the core surface by generating a grid of angles θ on [0, π] and angles ϕ on [0, 2π], thereby creating an array of vectors

$\vec{r}^*$, where

$$\begin{aligned} \vec{r}^* &= x^*\,\hat{e}_x + y^*\,\hat{e}_y + z^*\,\hat{e}_z \qquad (3.7) \\ &= a\cos\phi\sin\theta\hat{e}_x + b\sin\phi\sin\theta\hat{e}_y + c\cos\theta\hat{e}_z. \qquad (3.8) \end{aligned}$$

When dealing with the CMB rather than the outer surface, then a, b, and c are replaced by a_c, b_c, and c_c.

3.4 Step 4: The Surface Normal

At each point on the surface (i.e. for each $\vec{r}^*$), $\hat{n}$ is readily found. The surface of the ellipsoid is defined mathematically by the following function:

$$f(x^*, y^*, z^*) = \frac{(x^*)^2}{a^2} + \frac{(y^*)^2}{b^2} + \frac{(z^*)^2}{c^2} = 1. \qquad (3.9)$$

Then the surface normal is defined as the gradient of the function f:

$$\begin{aligned} \vec{n} &= \nabla f(x,y,z)\big|_{x^*,y^*,z^*} \\ &= \nabla\Big(\frac{x^2}{a^2} + \frac{y^2}{b^2} + \frac{z^2}{c^2}\Big)\Big|_{x^*,y^*,z^*} \\ &= \left(\frac{\partial f}{\partial x}\hat{e}_x + \frac{\partial f}{\partial y}\hat{e}_y + \frac{\partial f}{\partial z}\hat{e}_z\right)\Big|_{x^*,y^*,z^*} \\ &= \frac{2x^*}{a^2}\hat{e}_x + \frac{2y^*}{b^2}\hat{e}_y + \frac{2z^*}{c^2}\hat{e}_z. \qquad (3.10) \end{aligned}$$

The surface normal we use here is the downward facing surface normal to align with the downward acceleration vector, so each component is multiplied by -1. Using the notation $\vec{n} = n_x\hat{e}_x + n_y\hat{e}_y + n_z\hat{e}_z$, then it follows that the components of the surface

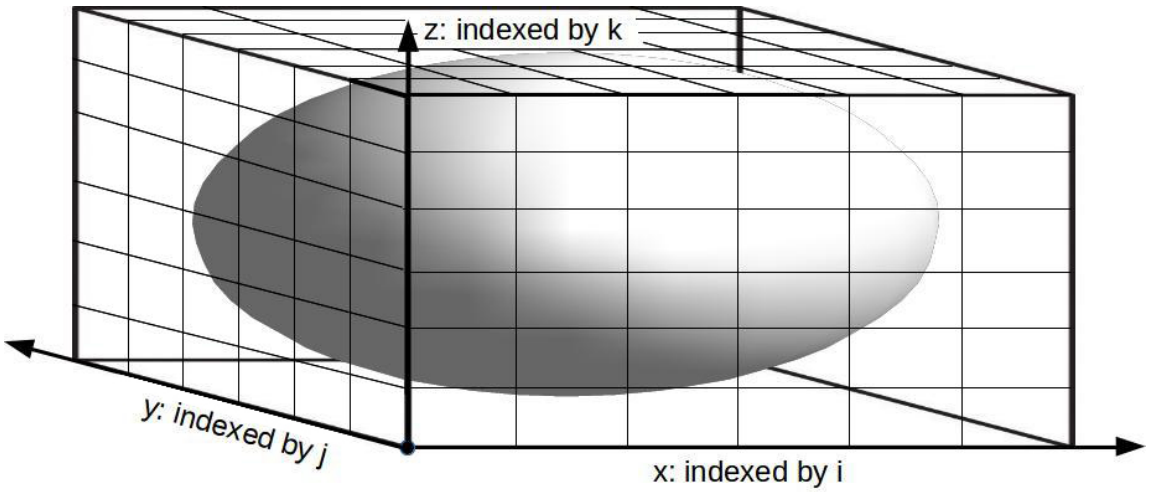

Figure 3.1: The Discretized Volume of Our Code, Encompassing the Ellipsoid Representing Haumea.

normal are

$$n_x = -\frac{2x^*}{a^2} \tag{3.11}$$

$$n_y = -\frac{2y^*}{b^2} \tag{3.12}$$

$$n_z = -\frac{2z^*}{c^2}. \tag{3.13}$$

Then the unit normal vector $\hat{n}$ is obtained by dividing each component of $\vec{n}$ by its magnitude, $|\vec{n}| = \sqrt{n_x^2 + n_y^2 + n_z^2}$. The final forms of the components of the downward unit normal vector which the code uses are

$$\hat{n}_x = -\frac{2x^*}{a^2|\vec{n}|} \tag{3.14}$$

$$\hat{n}_y = -\frac{2y^*}{b^2|\vec{n}|} \tag{3.15}$$

$$\hat{n}_z = -\frac{2z^*}{c^2|\vec{n}|}. \tag{3.16}$$

3.5 Step 5: Finding $\vec{g}$

To calculate the acceleration vector due solely to gravity, $\vec{g}$, we have to integrate over the whole mass:

$$\vec{g}(\vec{r}^{*}) = -\int \frac{G\rho(\vec{r}\,')}{|\vec{r}^{*} - \vec{r}\,'|^3}\left[\vec{r}^{*} - \vec{r}\,'\right] d^3\vec{r}\,'. \tag{3.17}$$

To do this we discretize a computational volume including the ellipsoid, as shown in Figure 3.1. First a three-dimensional cartesian grid is defined for only positive values, in one octant. The cartesian grid is divided into N_x, N_y, and N_z zones in the x, y, and z directions, respectively. We define axes and indices according to Figure 3.1, so that the x axis is indexed by i, the y axis is indexed by j, and the z axis is indexed by k. The mass in each grid cell is calculated and a density ρ_{ijk} calculated for each cell. For cells that straddle the core and mantle, we use a Monte Carlo method (Press et al. 1992) to find the average density in the cell. Once the two-phase solid is constructed within one octant (including zero density in all grid cells beyond the outer surface), the grid space is then extended by mirroring over each of the axes. Mass and density values assigned to points from the one-octant space are also extended into the full mirrored space. In this way, the entire solid of Haumea is created as an ellipsoid with a rocky core and an icy mantle. Because the outer surface ends up being pixellated, the outer boundary of the grid space is extended a small distance away from the outer surface to accommodate all of the solid material (as can be somewhat seen in Figure 3.1). The space is extended by 5 percent of the ellipsoidal radius beyond the outer surface, and this extra room provides enough space for all of the non-zero density points created. With this construction in mind, our gravitational acceleration vector then becomes

$$\vec{g} = -\sum_i \sum_j \sum_k \frac{G(dM)_{ijk}}{|\vec{r}^{*} - \vec{r}_{ijk}\,'|^3}\left[|\vec{r}^{*} - \vec{r}_{ijk}\,'|^3\right], \tag{3.18}$$

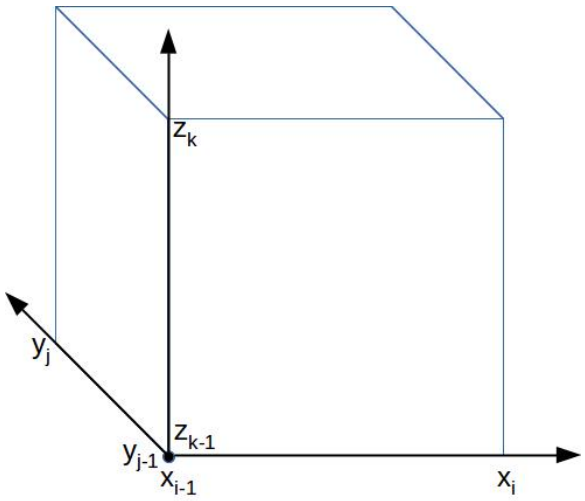

Figure 3.2: The Setup of the ijk^{th} Cell of Our Code.

where dM_{ijk} represents the mass in cell ijk, and $\vec{r}_{ijk}\ '$ is the radius vector to the center of the ijk^{th} cell.

If a cell contains uniform density ρ, then (referring to Figure 3.2),

$$dM_{ijk} = \rho(x_i - x_{i-1})(y_j - y_{j-1})(z_k - z_{k-1}). \tag{3.19}$$

Otherwise, if a cell straddles the CMB surface boundary, then dM_{ijk} is solved using a Monte Carlo method.

For those particular grid cells straddling the CMB, we randomly populated them with points in each axial direction, with those deemed inside the CMB assigned rock density and those deemed outside the CMB given ice density. Utilizing Monte Carlo methods this way, the precise location of points which make up the solid vary for each run, thus providing a more robust construction. To verify the accuracy of this method, we sum up the mass values of all the cells and then divide by the actual mass from Ragozzine and Brown (2009). The resulting mass error is reported for each run.

3.6 Step 6: Putting it All Together

To calculate the total acceleration vector, taking into account both gravitational and rotational forces, first the coordinates at the centers of each cell (shown in Figure 3.2) were defined by taking the average of the sum of the i^{th} and the $(i-1)^{th}$ coordinates:

$$x_c = \frac{x_i + x_{i-1}}{2} \tag{3.20}$$

$$y_c = \frac{y_i + y_{i-1}}{2} \tag{3.21}$$

$$z_c = \frac{z_i + z_{i-1}}{2}, \tag{3.22}$$

where the subscript c refers to "center." With these coordinates, the radius $\vec{r}$ pointing from each zone directly to the center of the ellipsoid can be defined. The components of $\vec{r}$ are defined as $|\vec{r_x}| = x_c - x^*$, and so on:

$$\vec{r} = (x_c - x^*)\hat{e}_x + (y_c - y^*)\hat{e}_y + (z_c - z^*)\hat{e}_z. \tag{3.23}$$

Again, (x^*, y^*, z^*) are components of the radial vector pointing from the ellipsoid's center to the outer surface. It follows that the magnitude of $\vec{r}$ is defined as

$$r = |\vec{r}| = \sqrt{(x_c - x^*)^2 + (y_c - y^*)^2 + (z_c - z^*)^2}. \tag{3.24}$$

Keeping in mind that the centrifugal acceleration only acts in the x and y directions, since the z axis is the rotational axis, the total effective acceleration vector $\vec{g}_{\text{eff}}$ due to both gravitational and rotational forces then has components:

$$g_{\text{eff,x}} = \frac{GM}{r^3}(x_c - x^*) + \omega^2 x^* \tag{3.25}$$

$$g_{\text{eff,y}} = \frac{GM}{r^3}(y_c - y^*) + \omega^2 y^* \tag{3.26}$$

$$g_{\text{eff,z}} = \frac{GM}{r^3}(z_c - z^*), \tag{3.27}$$

where G is the universal gravitational constant and M is the total mass. As for the surface normal components, these components are also normalized via division of the magnitude of $\vec{g}_{\rm eff}$: $|\vec{g}_{\rm eff}| = \sqrt{g_{\rm eff,x}^2 + g_{\rm eff,y}^2 + g_{\rm eff,z}^2}$.

Finally, we measure how well each unit area of the surface aligns with the local equipotential surface. This is defined with the inner product of $\hat{n}$ and $\hat{g}$:

$$\hat{n} \cdot \hat{g}_{\rm eff} = \hat{n}_x \hat{g}_{\rm eff,x} + \hat{n}_y \hat{g}_{\rm eff,y} + \hat{n}_z \hat{g}_{\rm eff,z}. \tag{3.28}$$

We find this quantity on each point generated on the surface by a combination of θ and ϕ, then we add up all the $(\hat{n} \cdot \hat{g}_{\rm eff})$'s and divide by the number of (θ, ϕ) combinations. Our metric is calculated as

$$\mathcal{M} = \sum_{N_\theta} \sum_{N_\phi} \frac{\hat{n} \cdot \hat{g}_{\rm eff}}{N_\theta N_\phi}, \tag{3.29}$$

where N_θ is the number of values of θ in which points were generated, and N_ϕ is the number of values of ϕ over which points were generated. Usually we picked ten values of each. It is this metric $\mathcal{M}$ which is then computed for each combination of CMB axial ratios $p_c = b_c/a_c$ and $q_c = c_c/a_c$. If the surface coincides with an equipotential surface, then $\mathcal{M}$ is equal to 1.

3.7 Sequence of Runs Done and Contour Plots

We define N_x as half the number of cells in the x direction, and similarly for N_y and N_z. In all of the runs, $N_x = N_y = N_z$, and I will usually just refer to N_x when discussing the resolution. A low-resolution run set $N_x = 15$, a medium-resolution run has $N_x = 30$, and a high-resolution set N_x equal to 60. Three low resolution runs ($N_x = 15$) were done for each of the four shapes calculated by R06, corresponding to core densities of 2700, 3000, and 3300 kg m^{-3}. During each run every possible triaxial ellipsoid p_c and q_c ratio for the core was tested. For each combination of p_c and q_c, $\mathcal{M}$ and the total mass error were calculated. We then calculated a quantity from the

metric that we call "fit angle":

$$\Theta = \cos^{-1} \mathcal{M}. \tag{3.30}$$

This represents the angle between $\hat{n}$ and $\hat{g}_{\text{eff}}$ averaged over the whole surface (either the outer surface or the CMB).

In our first formulation, the code described above took more than two weeks to complete a low-resolution run. We then took all of the functions and definitions in the code and, where possible, vectorized all array operations. As a result of this vectorization, the code was optimized greatly from its previous state, so that it now takes around ten days to complete a high-resolution run.

Two p_c vs. q_c contour plots in Θ were produced corresponding to each run, one plot for the outer surface and another for the CMB surface. This way, the plots can be visually scanned to look for which combination of p_c and q_c for the core best minimizes the metric for both the outer surface and CMB surface. Two particular shape configurations which looked promising were then run again at medium resolution ($N_x = 30$) and high resolution ($N_x = 60$). These shapes correspond to shape 1 (from Table 1.1), the Jacobi ellipsoid with its rotation axis perpendicular to our line of sight, with a core density of 2700 kg m^{-3}; and also to shape 4 (also from Table 1.1), the Maclaurin spheroid which is more spherical in shape, with a core density of 3300 kg m^{-3}.

A new way of displaying contour plots was created for many of our results. Contour lines for the surface fit angles were overlain onto a contour plot of the CMB fit angles, and markers were placed at the points on the plots corresponding to where the fit angle was minimized, for both the surface and the CMB. Using this type of combination plot overlay, we have the ability to see which configurations have ideal regions that overlap most closely. Those regions that show the best overlap between the surface

and CMB are considered to be the most stable solutions. This will tell us which is the most likely core density for a given outer surface shape. The core shape can then be calculated from the solution's location on the contour plot, and from the core's shape, dimensions, and density, we can then build a complete picture of what the interior of Haumea looks like.

We also focused on a fifth shape, from Lockwood et al. (2014). This shape is a Jacobi ellipsoid very similar to shape 1, but it was calculated in a more robust way, using data from the first observations of Haumea in which it was resolved from its satellites (Lockwood et al. 2014). This provided a pure light curve of Haumea alone, and Jacobi's formula was used in concert with the light curve to calculate this new shape (Lockwood et al. 2014). More attention was given to the low core density (2700 kg m^{-3}) case for shape 5 instead of shape 1, and most of our highest-resolution runs ($N_x = 60$) were performed for shape 5. The combination contour plot technique described above was used largely for this shape, as well as for shape 4.

Chapter 4

RESULTS

4.1 Initial Resolution Runs

Each time our code is run with a fixed value of core density ρ_c, it generates a series of calculations for each possible combination of p_c and q_c for the core, subject to the constraint $0.43 \leq q_c < p_c \leq 1$. Running through all values of p_c and q_c will morph the core's dimensions through all allowable shapes of a triaxial ellipsoid. A run also calculates the core's longest axis a_c, from which the other two core axes can be quickly calculated, as well as the mass error- how closely the code approximated Haumea's actual mass after the density distribution was discretized. The outer surface is held fixed for five different shapes: shapes 1 through 4 from R06, and shape 5 from Lellouch et al. (2010) and Lockwood et al. (2014). These shapes are relisted in Table 4.1 (repeated from Table 1.1). So a single run will calculate the average metric (and hence, average fit angle between potential and surface normal) on both the outer surface and the core-mantle boundary (CMB), for all possible shapes of the core.

Before embarking on all of the runs we thought we needed, the code was tested for speed and for numerical convergence as a function of resolution. Two factors determine the code's resolution. The first, N_x, is the number of grid spaces in a particular dimension, in this case, x. Though the axes are of different lengths, N_x was set equal to both N_y and N_z, so that each axis contained the same number of grid spaces. Table 4.2 shows the results of the average outer surface fit angle (Θ_{surf}) for two trials each of five different values of N_x, in which the entire body of Haumea was set at a uniform density of 2551 kg m^{-3} and the outer surface was defined by

Shape	a (km)	b (km)	c (km)	p	q	ϕ	Reference	N_x
1	980	759	498	0.77	0.51	90°	R06	15, 30
2	1250	540	430	0.43	0.34	$> 47°$	R06	15
3	870	870	500	1	0.57	n/a	R06	15
4	750	750	524	1	0.70	n/a	R06	15, 30, 60
5	960	770	495	0.80	0.52	90°	Lockwood et al. 2014	30, 60

Table 4.1: Five Different Shapes for Haumea Tested in This Work.

shape 1. This density is taken from Lacerda and Jewitt (2007), assuming the angle between the rotational axis and our line of sight (the aspect angle) was 90°. Since this is an analytic solution, we expect this uniform density case to produce a fit angle of 0°. Due to imperfect resolution, the outer surface is not smooth; therefore, Θ_{surf} will not be exactly zero, but it is expected to more closely approach zero with higher resolution. The table shows the generally expected pattern, as the fit angle lessens with higher resolution, although a question mark hangs over the $N_x = 120$ resolution runs, in which the fit angle seemed to increase. In any event, the $N_x = 120$ resolution was prohibitively time consuming. Thus, $N_x = 60$ was taken as our highest resolution cases and considered sufficiently converged, at the 0.5° level.

$N_x = N_y = N_z$	8	8	15	15	30	30	60	60	120	120
Trial	1	2	1	2	1	2	1	2	1	2
Θ_{surf} (°)	7.87	7.84	5.52	4.86	1.79	2.09	0.47	0.42	1.16	1.24

Table 4.2: The Relationship Between Resolution (N_x) and Θ_{surf}, the Fit Angle (in Degrees) Between the Gravity Vector and the Surface Normal, Averaged Over the Outer Surface. N_x Is the Number of Grid Spaces Along Each Axis, and $N_x = N_y = N_z$.

The second factor determining resolution is N, the number of Monte Carlo points used to calculate the density in grid cells straddling the core-mantle boundary. This value was varied between 10 and 10^4, and the results of varying both N and $N_x = N_y = N_z$ are shown in Table 4.3. For each resolution case, three runs were performed (with the exception of the $(N_x, N) = (15, 10^4)$ case, for which four runs were performed). The average of the outer surface fit angle for the three runs and the standard deviation σ of the three runs from the mean are listed for each case. Due to time constraints, we ultimately chose $(N_x, N) = (60, 10^2)$ as our highest resolution runs, $(N_x, N) = (30, 10^2)$, as our medium resolution runs, and $(N_x, N) = (15, 10^2)$ as our lowest resolution runs. For each value of N_x, especially $N_x = 60$, there is very little difference in Θ_{surf} average between the $N = 10^2$ and the $N = 10^4$ cases, so we considered the $N = 10^2$ case sufficiently converged. At the lowest resolution, the average of Θ_{surf} was constant only to within 5°; at medium resolution, the precision of Θ_{surf} is about 2°; and at highest resolution the average Θ_{surf} is converged to within about 0.5°. The majority of our runs will employ $N_x = 60$ and $N = 10^2$. Given the mismatch of 0.5° from the analytic solution for this resolution, we consider $\hat{g}$ and $\hat{n}$ aligned if $\Theta_{\text{surf}} \leq 0.5°$. This is then our finest sensitivity of checking how closely aligned are the gravitational potentials and the surface normals around each surface.

4.2 $p_c - q_c$ Contour Plots

In this section I present the graphical outputs of my simulations. As explained above, each figure graphs the axial ratios of the core p_c vs. q_c, and within this region representing all possible ellipsoidal shapes of the core, a color coded contour plot is overlain, which represents the values of the average fit angles over the respective surface (either the outer surface, Θ_{surf}, or the CMB, Θ_{cmb}). This representation allows for a visual verification of the minimum Θ_{surf} (or Θ_{cmb}) between the surface normal

N_x	N	Average Θ_{surf} (°)	σ
15	10^1	4.7033	0.9094
	10^2	4.9133	0.1007
	10^3	4.8900	0.0529
	10^4	4.7925	0.0340
30	10^1	1.6167	0.0751
	10^2	2.0267	0.1677
	10^3	2.0067	0.0404
	10^4	2.0000	0.0000
60	10^1	0.4993	0.0872
	10^2	0.4370	0.0030
	10^3	0.4467	0.0058
	10^4	0.4457	0.0006

Table 4.3: Fit Angle Computed in Test Runs with Various Resolutions of the Analytic Case for $\rho = 2551$ kg m^{-3}. N_x Is the Number of Grid Spaces in Each Direction, While N Is the Number of Monte Carlo Points Populating Each Grid Space. For Each Value of N_x, Five Runs Were Produced. The Average Fit Angle (in Degrees) of These Runs Is Θ_{surf}, and σ Is the Standard Deviation for Each Set of Three Runs.

(or CMB normal) and effective gravity over the surface, to within a precision of 0.5°. If the optimal (lowest fit angle) (p_c, q_c) combination for the CMB matches the optimal (p_c, q_c) for the outer surface, and the optimal fit angle for each is $\leq 0.5°$, then that set of p_c and q_c is a solution for the shape of both the CMB and the outer surface. This minimum fit angle gives the core shape required for the most stable surface. Therefore, when the optimal Θ ($\leq 0.5°$) appears in the same spot on both the outer surface and CMB plots, there is a stable configuration for Haumea.

I performed runs on each of the five shapes by changing the density of the core throughout the range 2700 kg m^{-3} to 3300 kg m^{-3}. The first set of runs were all low-resolution ($N_x = 15$), to survey the parameter space and determine which configurations merited higher-resolution runs. Shapes 1-4 were each run at low resolution for core densities of 2700 kg m^{-3}, 3000 kg m^{-3}, and 3300 kg m^{-3}.

The results for shape 1 are shown in Figures 4.1-4.3. All of these figures show that the match of the CMB to an equipotential surface is much more insensitive to changes in core shape than is the outer surface's match to an equipotential surface. The CMB plots also reveal spots of poor equipotential match in places, but these spots diminish with increasing resolution. When the core density is 2700 kg m^{-3}, Θ_{surf} shows a minimum and most stable point in the region around $(p_c, q_c) = (0.88, 0.5)$. This corresponds to a core that is highly pole-flattened and has a moderately elliptical equator. The axial ratios for the outer surface of shape 1 are $(p, q) = (0.774, 0.508)$. Also, it is apparent that for a core density ρ_c of 2700 kg m^{-3}, the minimum Θ core shape is very similar for both the surface and the CMB plots as expected, as the simulation approaches the analytic solution. Figures 4.2 and 4.3 show that as the core density increases, there is less of an overlap between the surface and CMB plots. While there is a decent optimized Θ overlap between the plots for $\rho_c = 3000$ kg m^{-3}, the overlap appears stronger for $\rho_c = 2700$ kg m^{-3}. There appears to be little to no optimized Θ overlap for when $\rho_c = 3300$ kg m^{-3}. This suggests that a low core density of 2700 kg m^{-3} with an outer surface corresponding to shape 1 and a core shape of around $(p_c, q_c) = (0.88, 0.5)$ is a valid solution.

Figures 4.4-4.6 show the results from testing shape 2. These plots show practically no overlap in optimized Θ between the surface and CMB for any possible core shape or any feasible core density. This suggests that shape 2 does not provide a configuration in which Haumea can reach interior and exterior equilibrium, and therefore shape 2

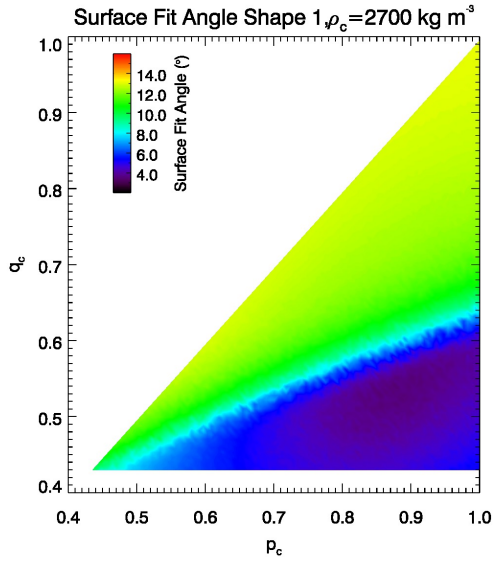

(a) Contour pq Plot for Shape 1.

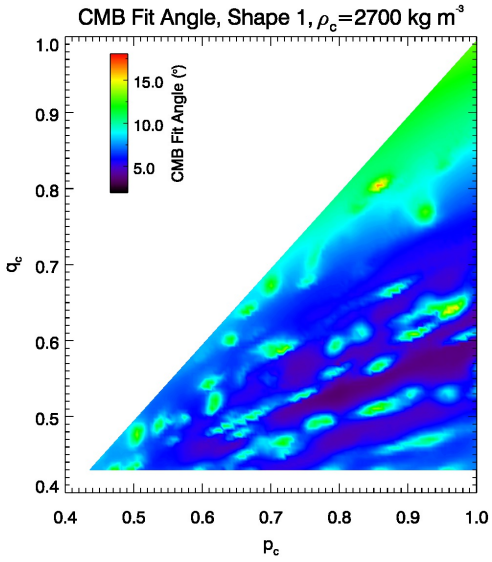

(b) Contour CMB pq Plot for Shape 1.

Figure 4.1: Contour Plots of Fit Angle at CMB and Fit Angle at Surface Versus Core Axis Ratios p_c and q_c with Core Density 2700 kg m^{-3}.

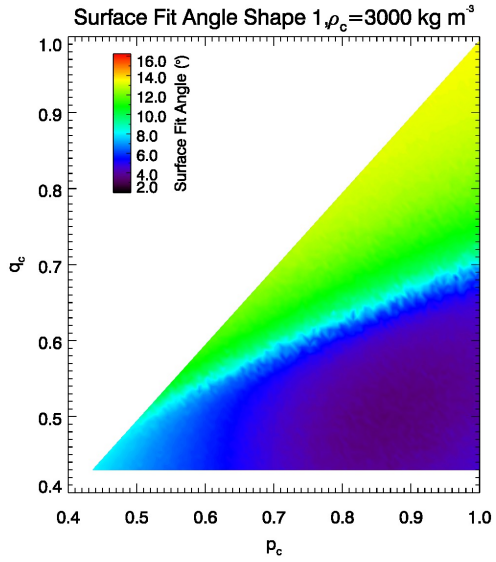

(a) Contour pq Plot for Shape 1.

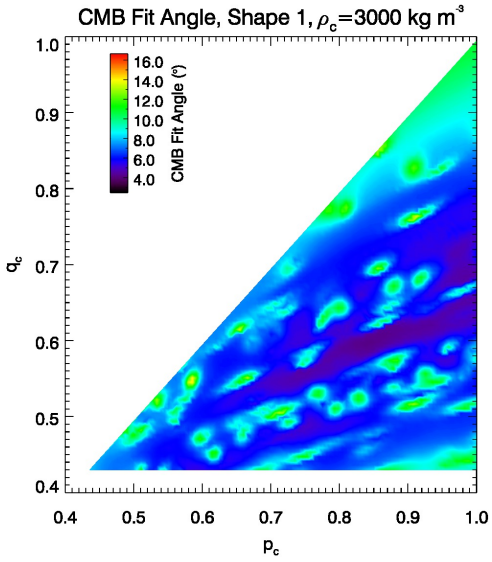

(b) Contour CMB pq Plot for Shape 1.

Figure 4.2: Same as Figure 4.1, Except for a Core Density of 3000 kg m^{-3}.

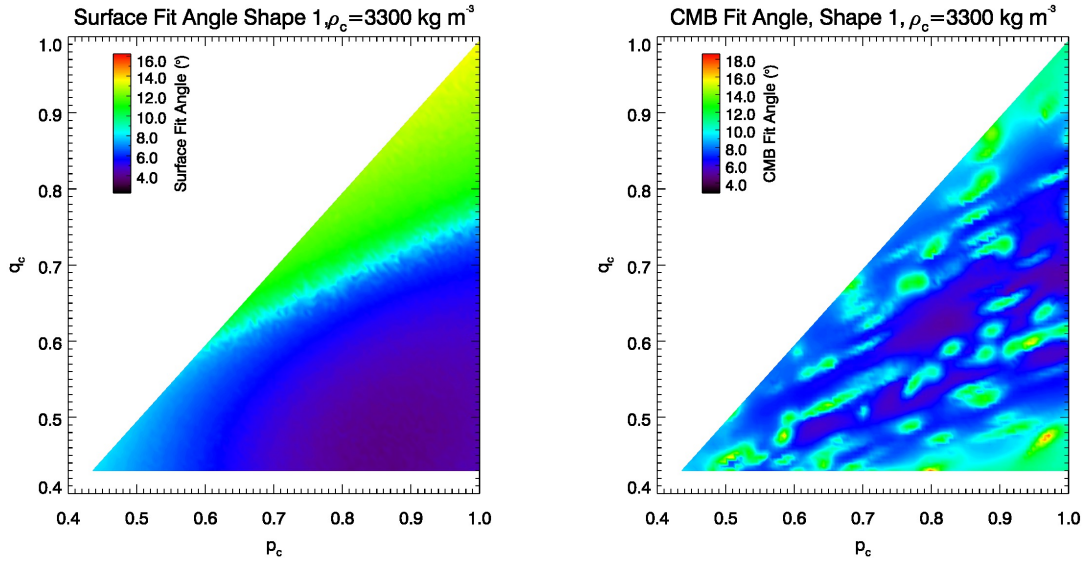

(a) Contour pq Plot for Shape 1. (b) Contour CMB pq Plot for Shape 1.

Figure 4.3: Same as Figure 4.1, Except for a Core Density of 3300 kg m^{-3}.

is not a solution. Shape 2 is the alternate Jacobi ellipsoid calculated by R06; however its outer axial ratios are $(p, q) = (0.432, 0.344)$. Neither axial ratio can take values less than 0.43 and still fall in the realm of a stable Jacobi ellipsoid. Thus, it might be mathematically expected that shape 2 would not provide a stable solution for any core density or shape.

Shape 3 and 4 correspond to Maclaurin spheroids, in which $p = 1$. The ratio $c/a = q$ describes the polar flattening ratio for these equatorially symmetric shapes. Figures 4.7-4.9 show contour plots for shape 3, which has axial ratio $q = 0.545$. There appears to be slight optimized fit angle (Θ) overlap between the surface and CMB plots when $\rho_c = 2700$ kg m^{-3}, but for higher core densities, there is no apparent overlap.

Shape 4 is a Maclaurin spheroid with $q = 0.699$, a rounder spheroid than shape 3. The contour plots for shape 3 show that when the core shape is made more spherical in the polar direction (i.e. when polar flattening decreases), the match to

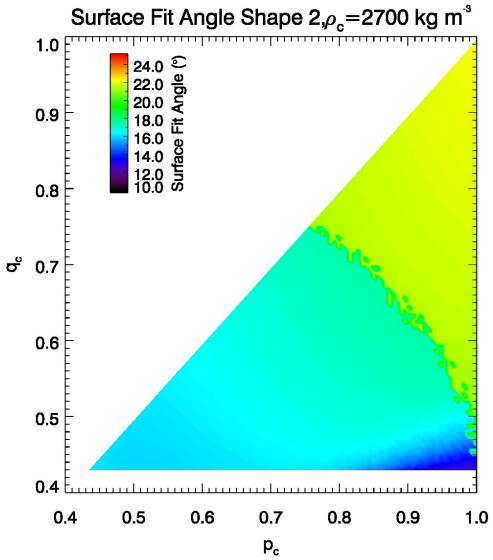

(a) Contour pq Plot for Shape 2.

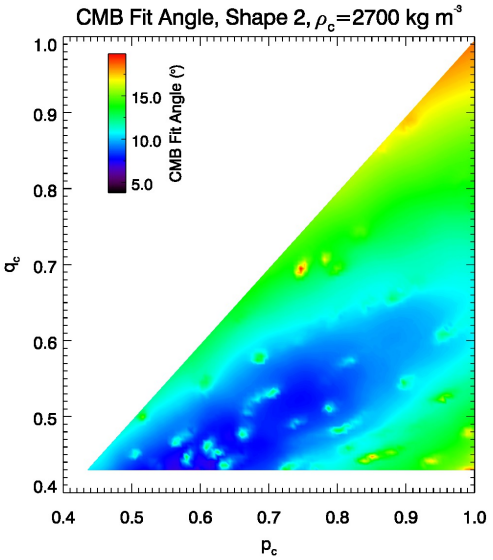

(b) Contour CMB pq Plot for Shape 2.

Figure 4.4: Same as Figure 4.1, but for Shape 2, with Core Density 2700 kg m^{-3}.

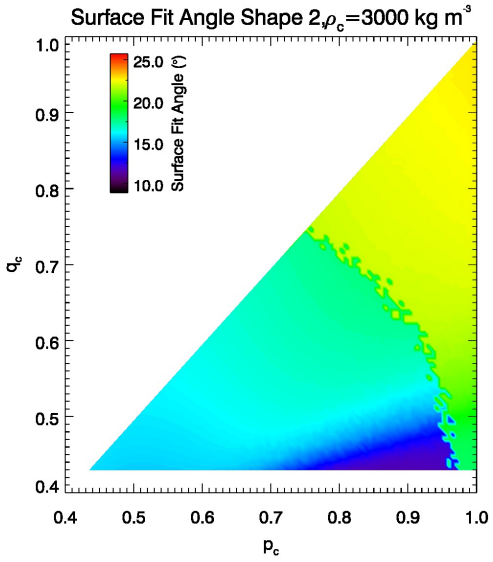

(a) Contour pq Plot for Shape 2.

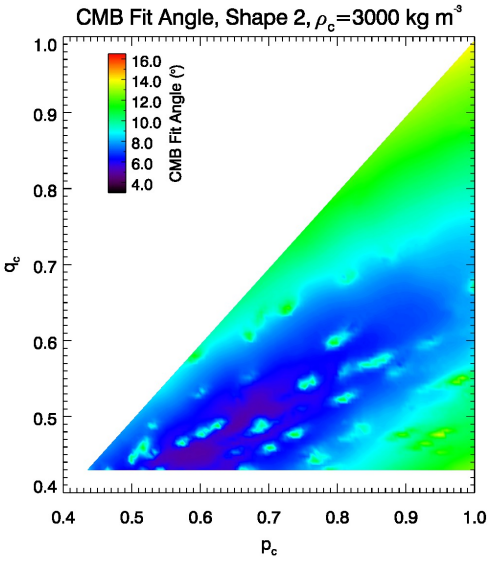

(b) Contour CMB pq Plot for Shape 2.

Figure 4.5: Same as Figure 4.4, Except for a Core Density of 3000 kg m^{-3}.

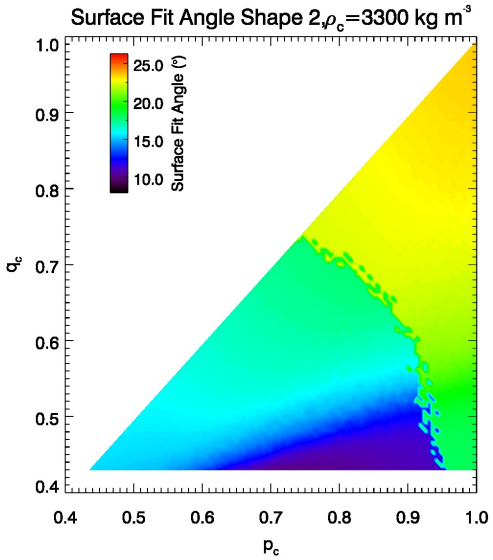

(a) Contour pq Plot for Shape 2.

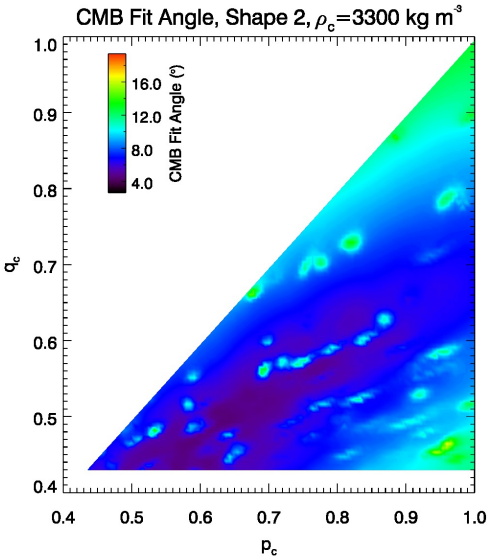

(b) Contour CMB pq Plot for Shape 2.

Figure 4.6: Same as Figure 4.4, Except for a Core Density of 3300 kg m^{-3}.

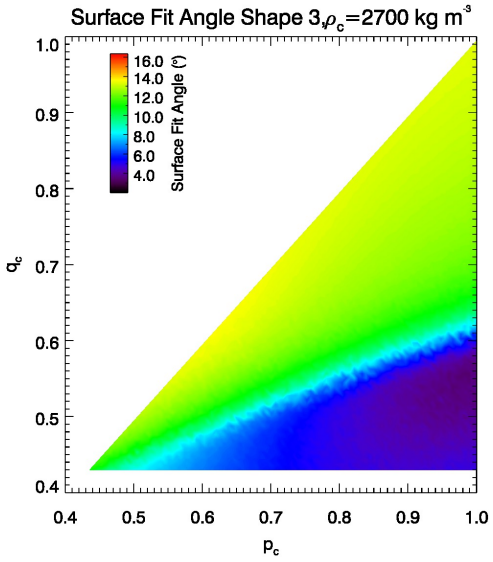

(a) Contour pq Plot for Shape 3.

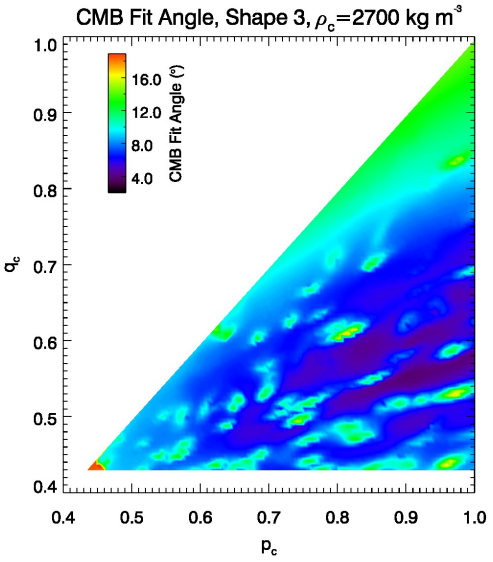

(b) Contour CMB pq Plot for Shape 3.

Figure 4.7: Same as Figure 4.1, but for Shape 3, with Core Density 2700 kg m^{-3}.

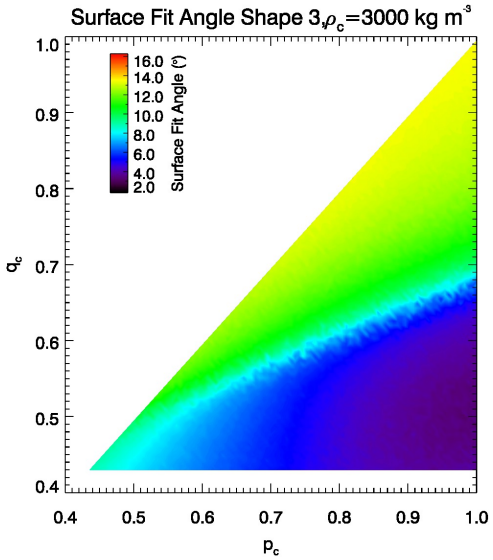

(a) Contour pq Plot for Shape 3.

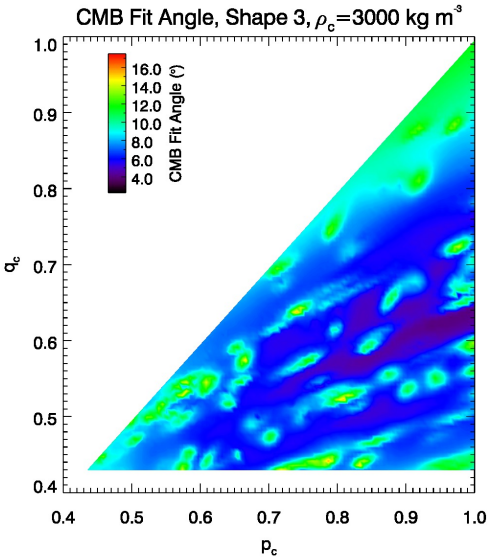

(b) Contour CMB pq Plot for Shape 3.

Figure 4.8: Same as Figure 4.7, Except for a Core Density of 3000 kg m^{-3}.

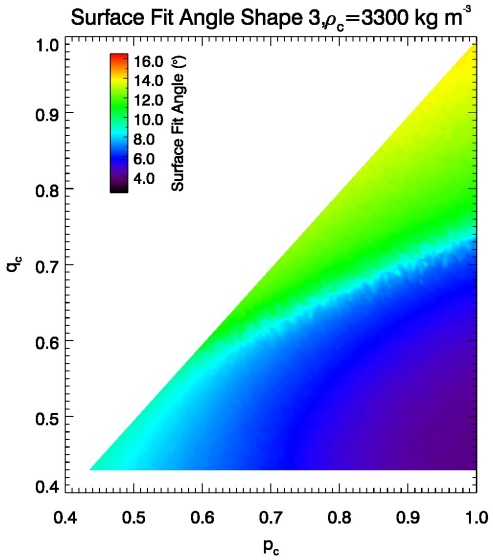

(a) Contour pq Plot for Shape 3.

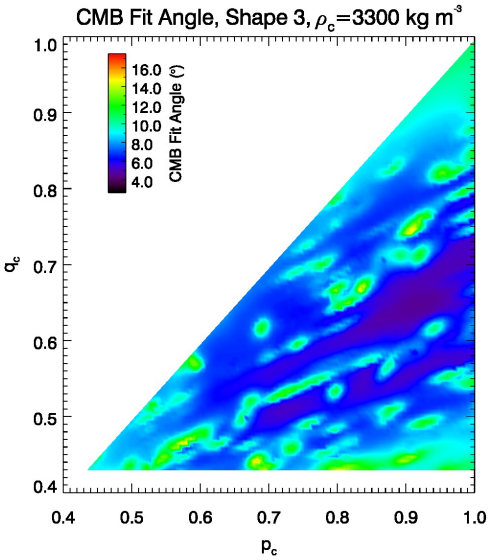

(b) Contour CMB pq Plot for Shape 3.

Figure 4.9: Same as Figure 4.7, Except for a Core Density of 3300 kg m^{-3}.

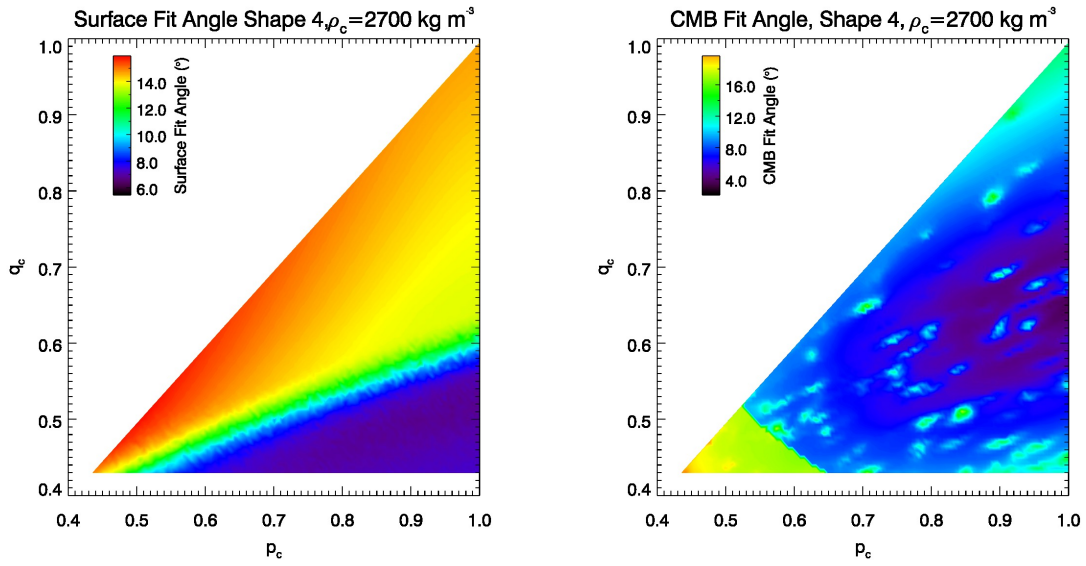

(a) Contour pq Plot for Shape 4. (b) Contour CMB pq Plot for Shape 4.

Figure 4.10: Same as Figure 4.1, but for Shape 4, with Core Density 2700 kg m^{-3}.

an equipotential surface of Haumea's outer surface largely decreases. shape 4 shows this effect is only more pronounced in Figures 4.10-4.12, as the match is extremely low when the core is more spherical. While there is little to no overlap between outer surface and CMB optimized Θ regions for low to medium core densities, there seems to be a fairly good overlap for $\rho_c = 3300$ kg m^{-3}. This overlap occurs around the region where the core has a shape $(p_c, q_c) = (1, 0.64)$, quite similar in shape to the outer surface but flatter.

Between shapes 1-4 and all of the core density cases, the two most stable configurations appear to be shape 1 with a low density, 2700 kg m^{-3} core, and shape 4 with a high density, 3300 kg m^{-3} core. These two configurations were then run at medium ($N_x = 30$) and high ($N_x = 60$) resolution, with an improved faster code which was optimized through vectorization. The results for shape 1 are shown in Figures 4.13 and 4.14. With higher resolution, the regions with optimized surface fit angle show up with much sharper detail in the same core shape location, roughly

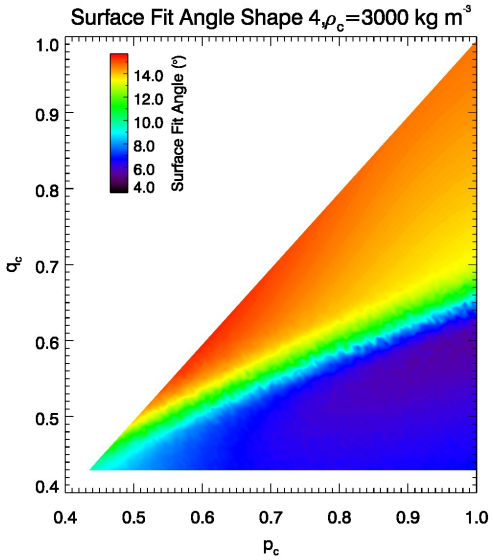

(a) Contour pq Plot for Shape 4.

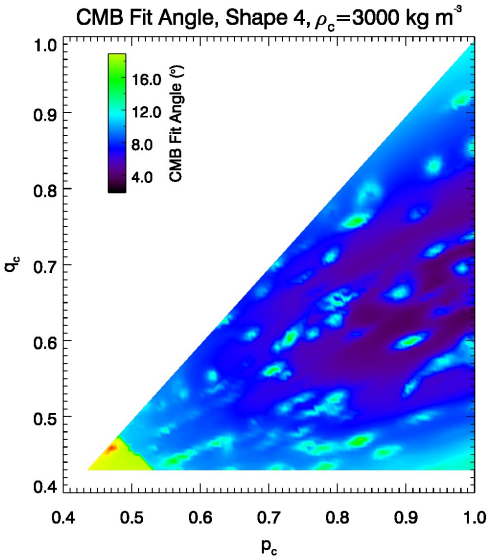

(b) Contour CMB pq Plot for Shape 4.

Figure 4.11: Same as Figure 4.10, Except for a Core Density of 3000 kg m^{-3}.

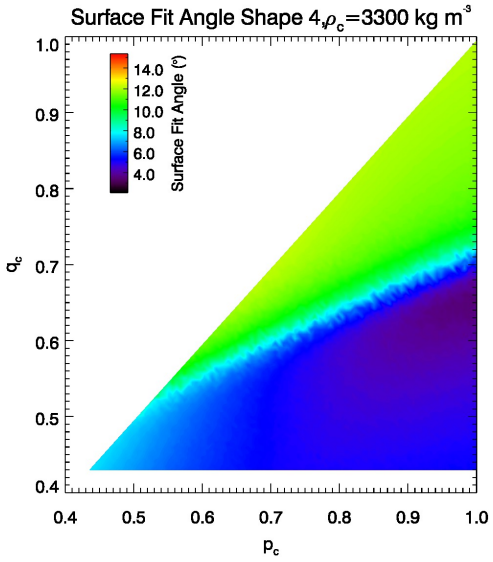

(a) Contour pq Plot for Shape 4.

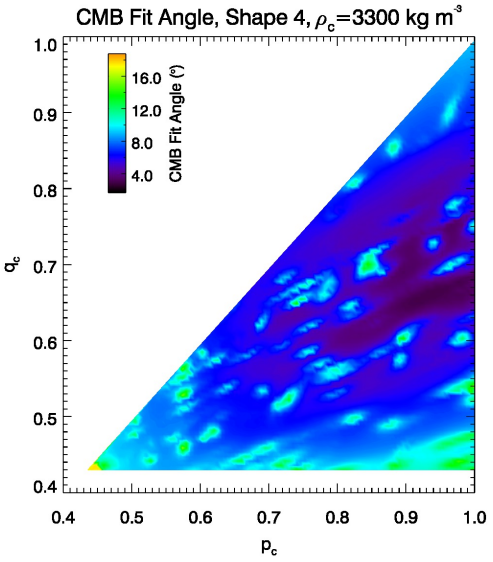

(b) Contour CMB pq Plot for Shape 4.

Figure 4.12: Same as Figure 4.10, Except for a Core Density of 3300 kg m^{-3}.

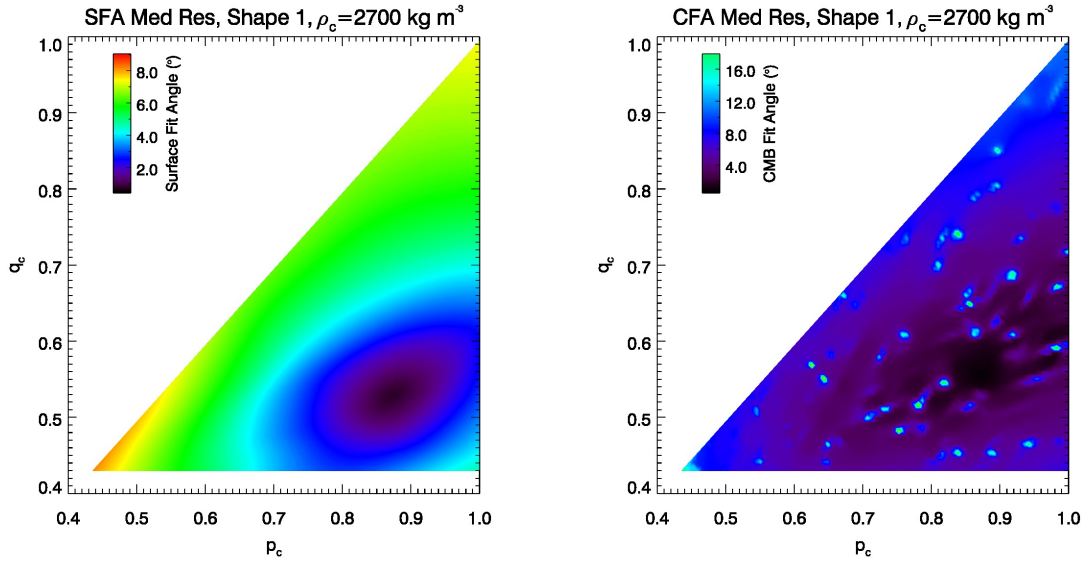

(a) Contour pq Plot for Shape 1. (b) Contour CMB pq Plot for Shape 1.

Figure 4.13: Same as Figure 4.1, but for Higher Resolution ($N_x = 30$).

around $(p_c, q_c) = (0.88, 0.50)$. Higher resolution also has an effect on all CMB plots to smooth out the field and to shrink all of the poor fit angle spots, which were often quite large and numerous at lower resolution. The region in the CMB plot containing the optimized Θ_{cmb} also is more easily seen, as that region of the plot contrasts more with its surroundings. The overlap between both plots' optimized Θ regions is seen more strongly with higher resolution. Higher resolution supports shape 1 with a low density core being a more stable configuration.

The higher resolution plots for shape 4 with a high core density are shown in Figures 4.15 and 4.16. A similar sharpening of the optimized minimum fit angle regions appears in these figures as for shape 1, and the core shape which most closely matches an equipotential surface here looks to be around $(p_c, q_c) = (1, 0.70)$, rather than (1, 0.64) as appeared in lower resolution.

As an additional case, we lastly considered the axes reported by Lockwood et al. (2014). Lockwood et al.ś observations are important because they captured the first

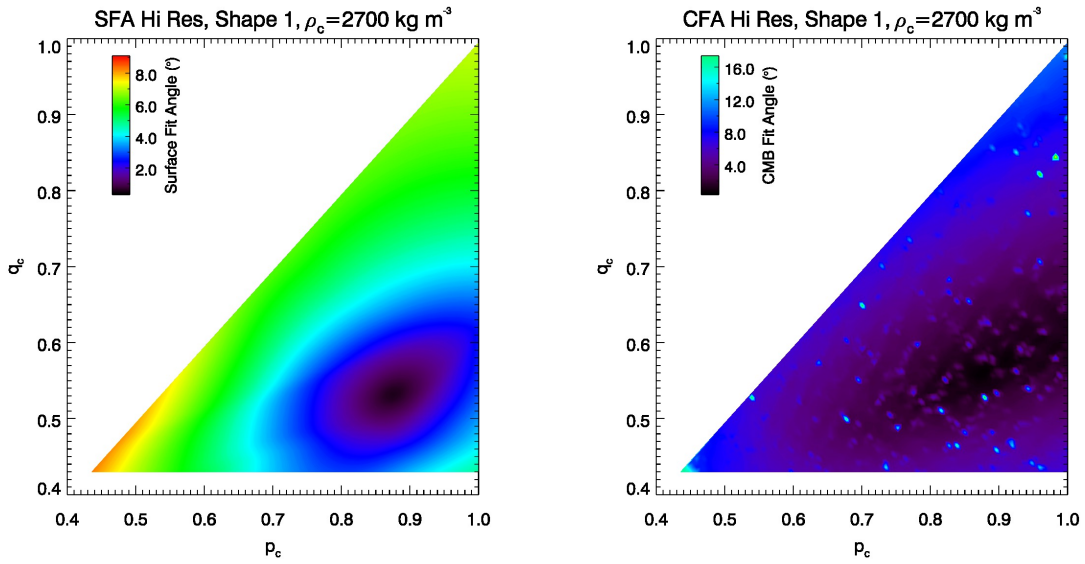

(a) Contour pq Plot for Shape 1. (b) Contour CMB pq Plot for Shape 1.

Figure 4.14: Same as Figure 4.13, but for Higher Resolution ($N_x = 60$).

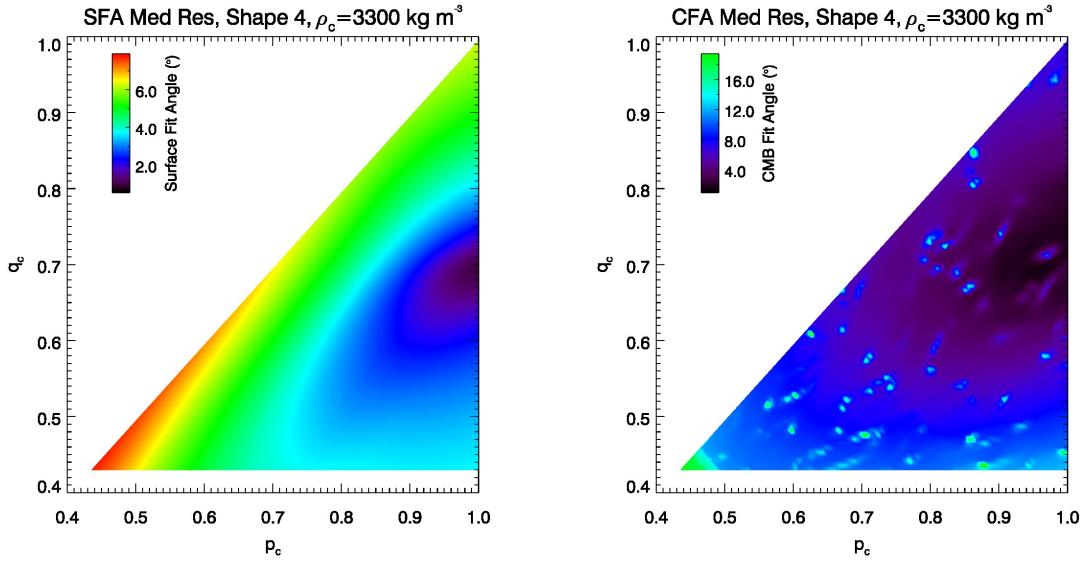

(a) Contour pq Plot for Shape 4. (b) Contour CMB pq Plot for Shape 4.

Figure 4.15: Same as Figure 4.12, but for Higher Resolution ($N_x = 30$).

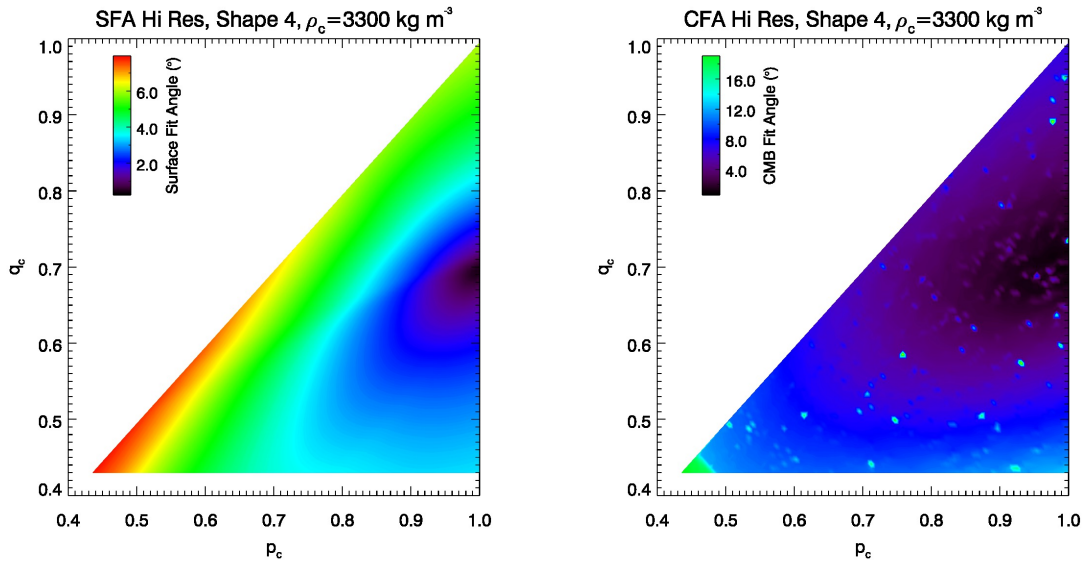

(a) Contour pq Plot for Shape 4. (b) Contour CMB pq Plot for Shape 4.

Figure 4.16: Same as Figure 4.15, but for Higher Resolution ($N_x = 60$).

light curve of Haumea in which Haumea was resolved separately from its satellites. From this light curve, more accurate dimensions are expected, and they confirmed the dimensions calculated by Lellouch et al. (2010) through thermal observations. These dimensions are then our shape 5 from Table 4.1, which is similar to shape 1. Shape 5 has axial ratios $(p, q) = (0.802, 0.515)$, as opposed to shape 1 having the dimensions $(p, q) = (0.774, 0.508)$. So shape 5 is a bit less flattened in the polar direction, but it is significantly rounder in the equatorial direction. From this point shape 5 was exclusively focused on instead of shape 1.

Medium and high resolution plots for both the surface and CMB of shape 5 are shown in Figures 4.17 and 4.18, for a core density of 2700 kg m^{-3}. Figures 4.19 and 4.20 show shape 5 with a core density of 3000 kg m^{-3} at medium and high resolution. Similarly, Figures 4.21 and 4.22 show shape 5 with $\rho_c = 3300$ kg m^{-3} at medium and high resolution. As expected due to its similarity with shape 1, shape 5 shows the best overlap between regions of optimized Θ for surface and CMB at low core density,

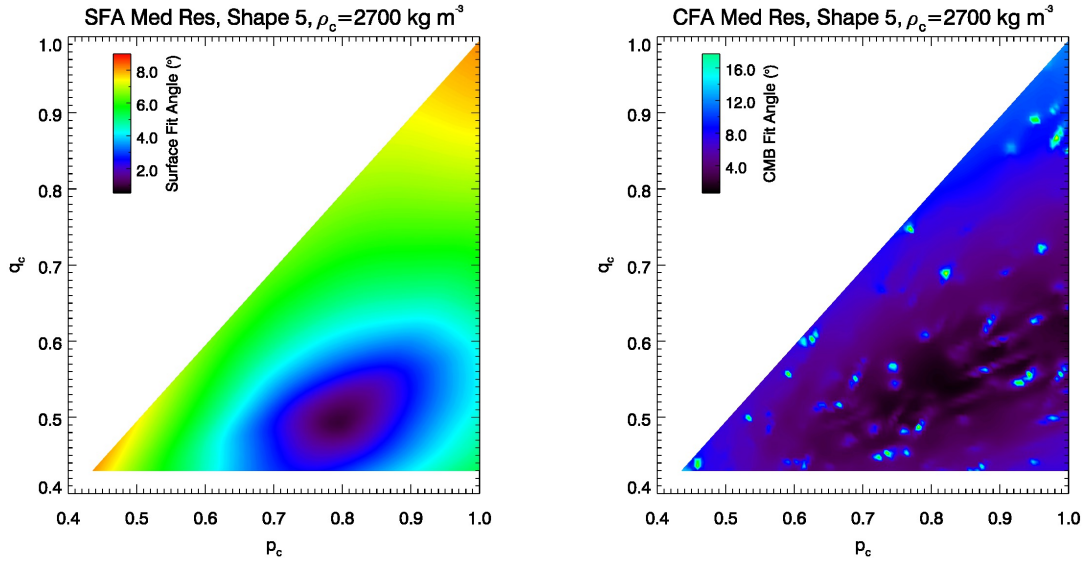

(a) Contour pq Plot for Shape 5. (b) Contour CMB pq Plot for Shape 5.

Figure 4.17: Same as Figure 4.13, but for Shape 5, with Core Density 2700 kg m^{-3} and $N_x = 30$.

$\rho_c = 2700$ kg m^{-3}. As the core density increases, these minimum fit angle regions between the outer surface and the CMB plots are seen to move away from each other more and more, signifying that Haumea is not stable with a higher core density in this shape. The most stable configuration at low core density appears to be at a core shape of around $(p_c, q_c) = (0.80, 0.50)$, almost exactly matching the shape of the outer surface.

Because shape 5 with low core density is such a promising candidate for overall gravitational and rotational stability for Haumea, we focus more in detail on this Jacobi ellipsoid by testing it out at seven different core densities, spanning the range from 2700 kg m^{-3} to 3300 kg m^{-3} in increments of 100 kg m^{-3}. As mentioned earlier, this range of core densities covers the entire range of feasible silicate densities expected in the Kuiper Belt.

In these seven high-resolution runs, we improved our ability to see how well (p_c, q_c) combinations yielding the optimized Θ match by superimposing the contour plots for

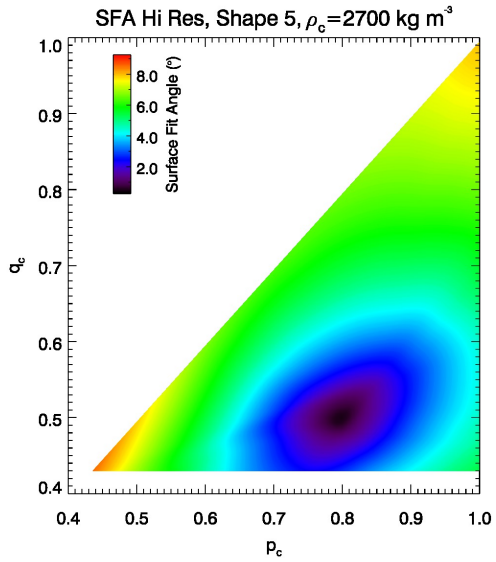

(a) Contour pq Plot for Shape 5.

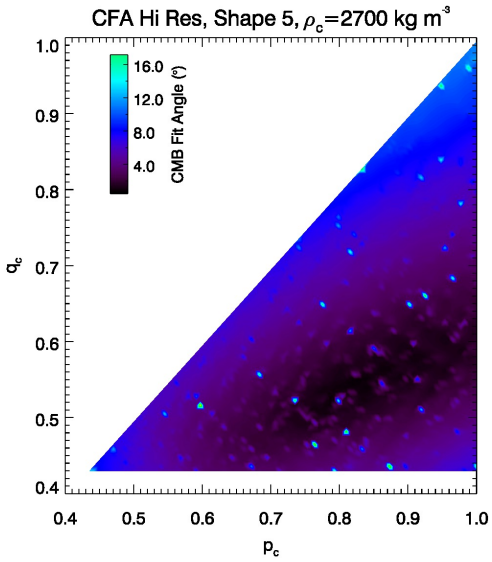

(b) Contour CMB pq Plot for Shape 5.

Figure 4.18: Same as Figure 4.17, but for Higher Resolution ($N_x = 60$).

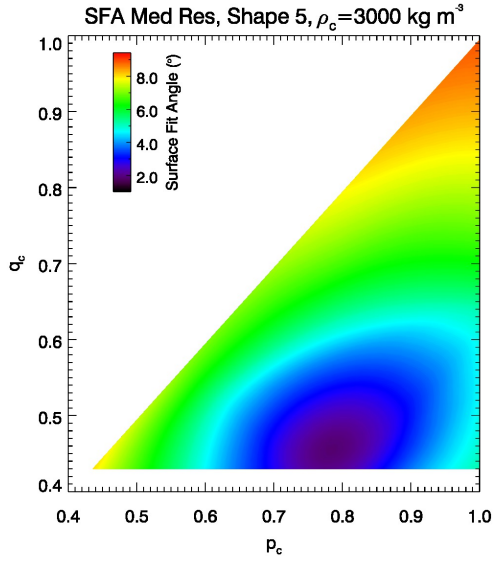

(a) Contour pq Plot for Shape 5.

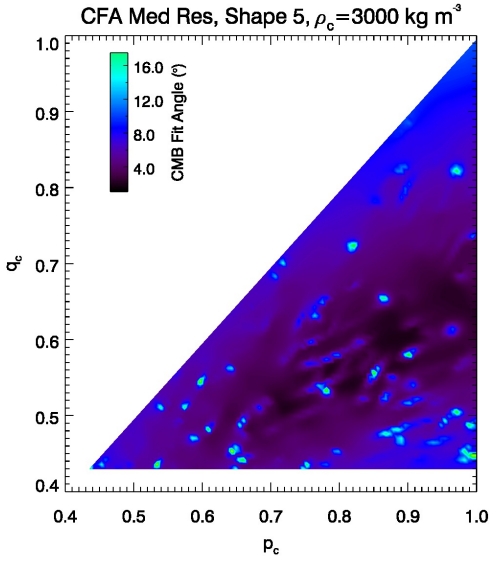

(b) Contour CMB pq Plot for Shape 5.

Figure 4.19: Same as Figure 4.17 ($N_x = 30$), Except for a Core Density of 3000 kg m^{-3}.

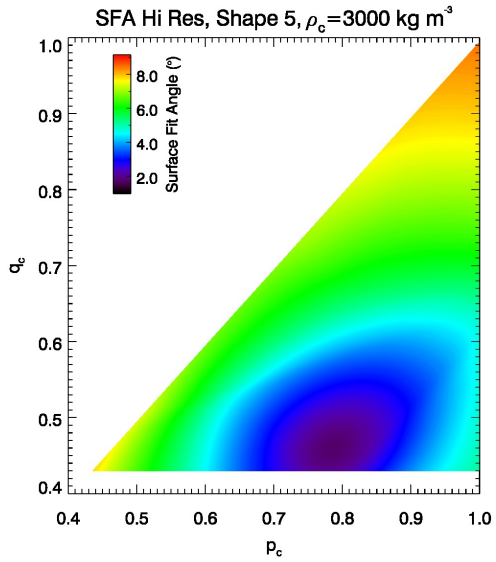

(a) Contour pq Plot for Shape 5.

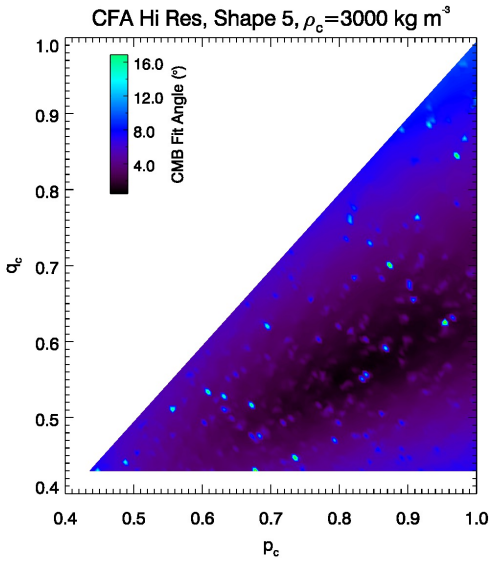

(b) Contour CMB pq Plot for Shape 5.

Figure 4.20: Same as Figure 4.19, but for Higher Resolution ($N_x = 60$).

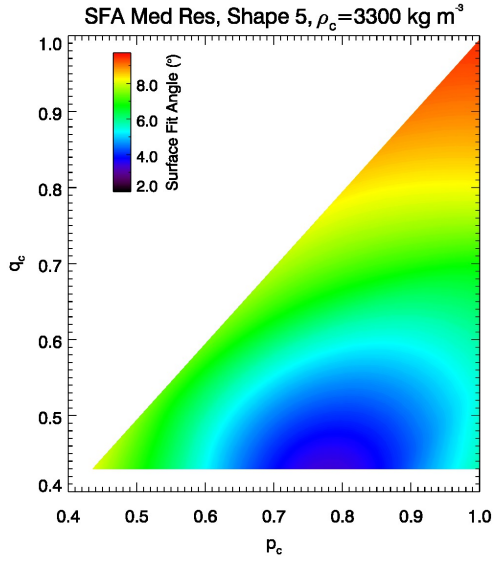

(a) Contour pq Plot for Shape 5.

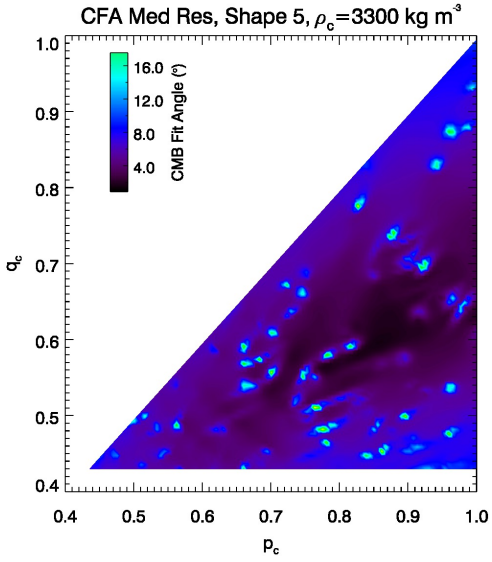

(b) Contour CMB pq Plot for Shape 5.

Figure 4.21: Same as Figure 4.17 ($N_x = 30$), Except for a Core Density of 3300 kg m^{-3}.

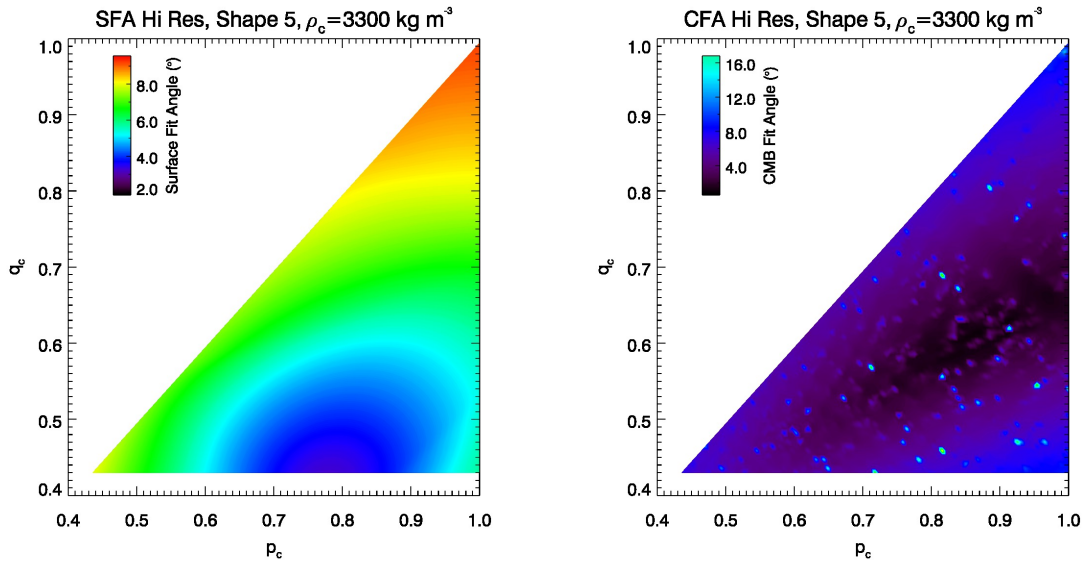

(a) Contour pq Plot for Shape 5. (b) Contour CMB pq Plot for Shape 5.

Figure 4.22: Same as Figure 4.21, but for Higher Resolution ($N_x = 60$).

the outer surface and the CMB. In these plots, shown in Figure 4.23 onward, the contour plot that forms the base color represents the CMB fit angle Θ_{cmb}, with values reported in the legend. Line contours for surface fit angle (Θ_{surf}) values were then overlain on top of this plot, with number values printed in the contours. Since the accuracy at this resolution is around 0.4°, contours were placed every 0.5°. A white star marks the particular core shape that gives a minimum fit angle for the outer surface, and a yellow star marks the corresponding minimum fit angle for the CMB. The closer these stars are, the closer is the configuration to equipotential surfaces. By analyzing these seven combination contour plots in Figures 4.23-4.29, the white and yellow stars do indeed separate further with increasing density beyond 2800 kg m^{-3}. Both stars are roughly the same distance away from each other at core densities of 2700 kg m^{-3} and 2800 kg m^{-3}, however. Also, the 0.5° contour circle around the white star shrinks with increasing core density, indicating a larger acceptable range of core shapes with lower core density. The minimum Θ_{surf} and the minimum Θ_{cmb}

are both less than 0.5° for ρ_c equal to both 2700 and 2800 kg m^{-3}. The (p_c, q_c) combination at optimized $\Theta_{\rm cmb}$ lies within 3 times the precision (0.5°) of the (p_c, q_c) combination for minimum $\Theta_{\rm surf}$ for both core densities, also.

High-resolution combination plots similar to those for shape 5 are shown for shape 4 in Figures 4.30-4.36. The (p_c, q_c) combinations which lead to the optimized fit angle Θ for surface and CMB plots are closest for shape 4 at a core density of 3300 kg m^{-3}, in Figure 4.36. In this example, they are within 0.5° of one another, which is a closer overlap than for shape 5 at ρ_c = 2700 kg m^{-3}. The minimum fit angle Θ for each plot in Figure 4.36 also has a value less than 0.5°, so that for this configuration, the outer surface and CMB both closely match equipotential surfaces. The optimized fit angles also seem to have these values and similarities for a core density of 3200 kg m^{-3}, as well, though they are not quite as close together in that case.

Here, I briefly address the marked splotchiness of the CMB contour plots. I suspect that these spots are caused by the random nature in which the grid cells straddling the CMB are populated. This leads to the code creating a bumpiness in the CMB surface. It can be seen from the figures in this chapter that the spots decrease in size with increasing resolution. While more spots appear with higher resolution, they obscure the fit angle trends much less than the larger but fewer spots at lower resolution. A convergence test was done to draw a relationship between the largest spot size and the resolution, and the result of this test is shown in Figure 4.37. Convergence occurs rapidly for increasing resolution.

In summary, only shape 4 with a core density of 3200–3300 kg m^{-3} has optimal (p_c, q_c) for the CMB and the outer surface that overlap to within the code's precision (0.5°). The only other case which comes close to this is shape 5 with a core density of 2700–2800 kg m^{-3}, although in that case the optimal (p_c, q_c) for the CMB and surface overlap only to within three times the precision of our code. Shape 5 with

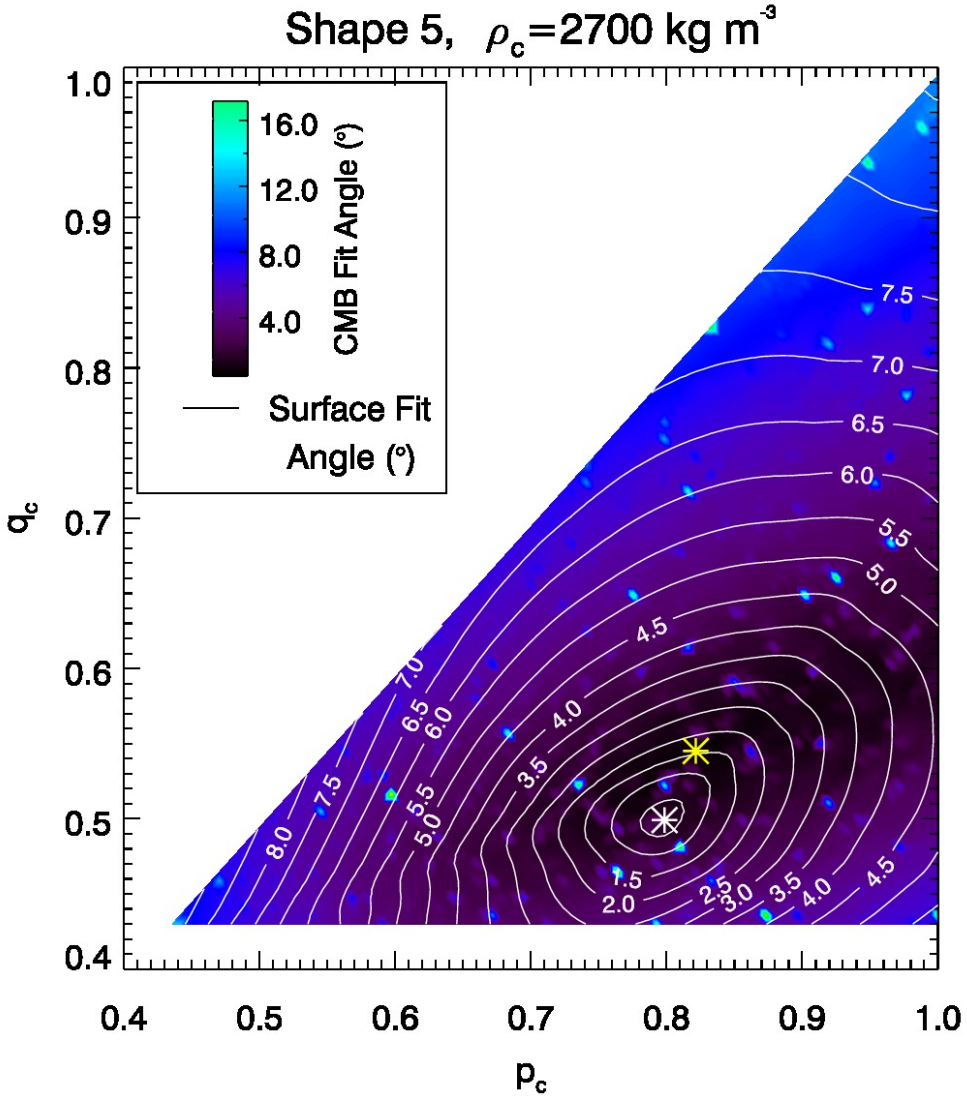

Figure 4.23: Contour Plot of Fit Angle at CMB Versus Core Axis Ratios p_c and q_c (Blue Color), and Fit Angle at Surface (White Contours).

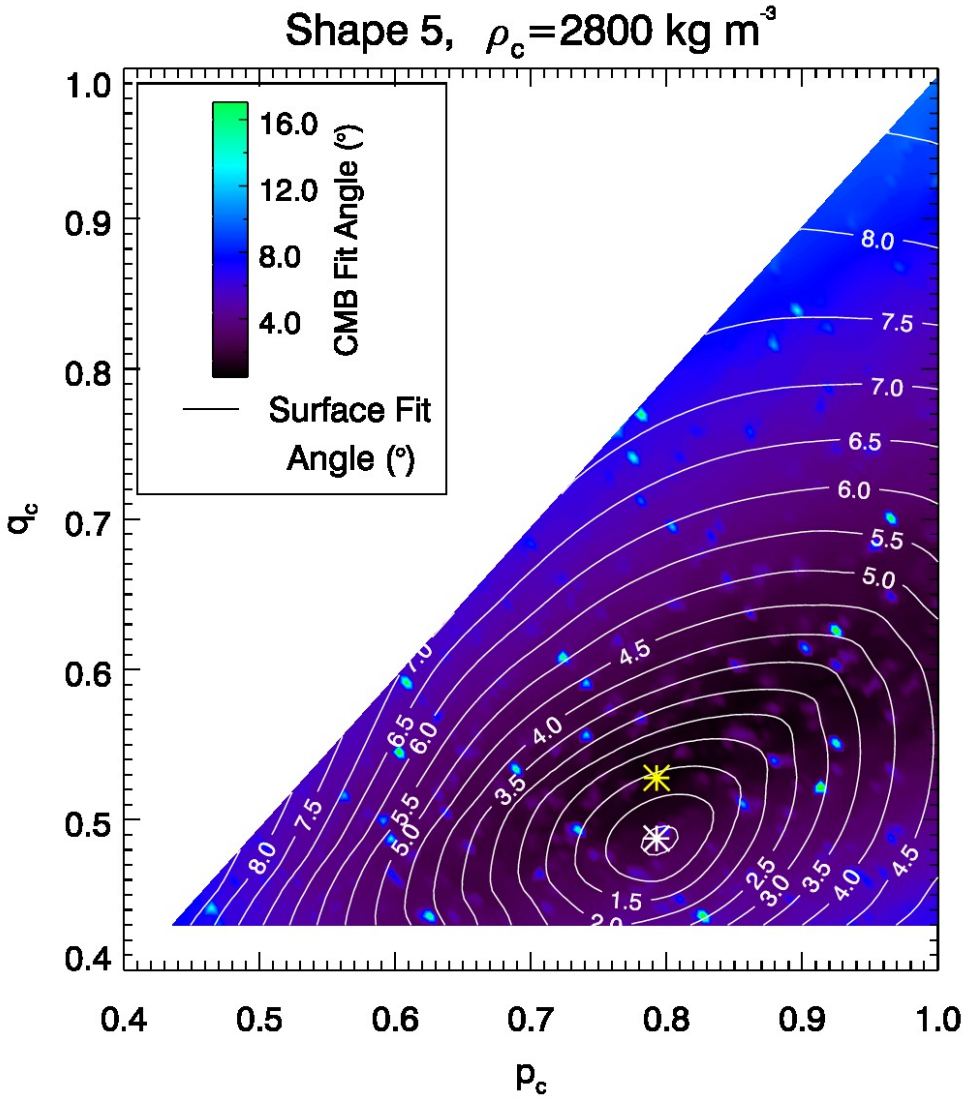

Figure 4.24: Same as Figure 4.23, Except for a Core Density of 2800 kg m^{-3}.

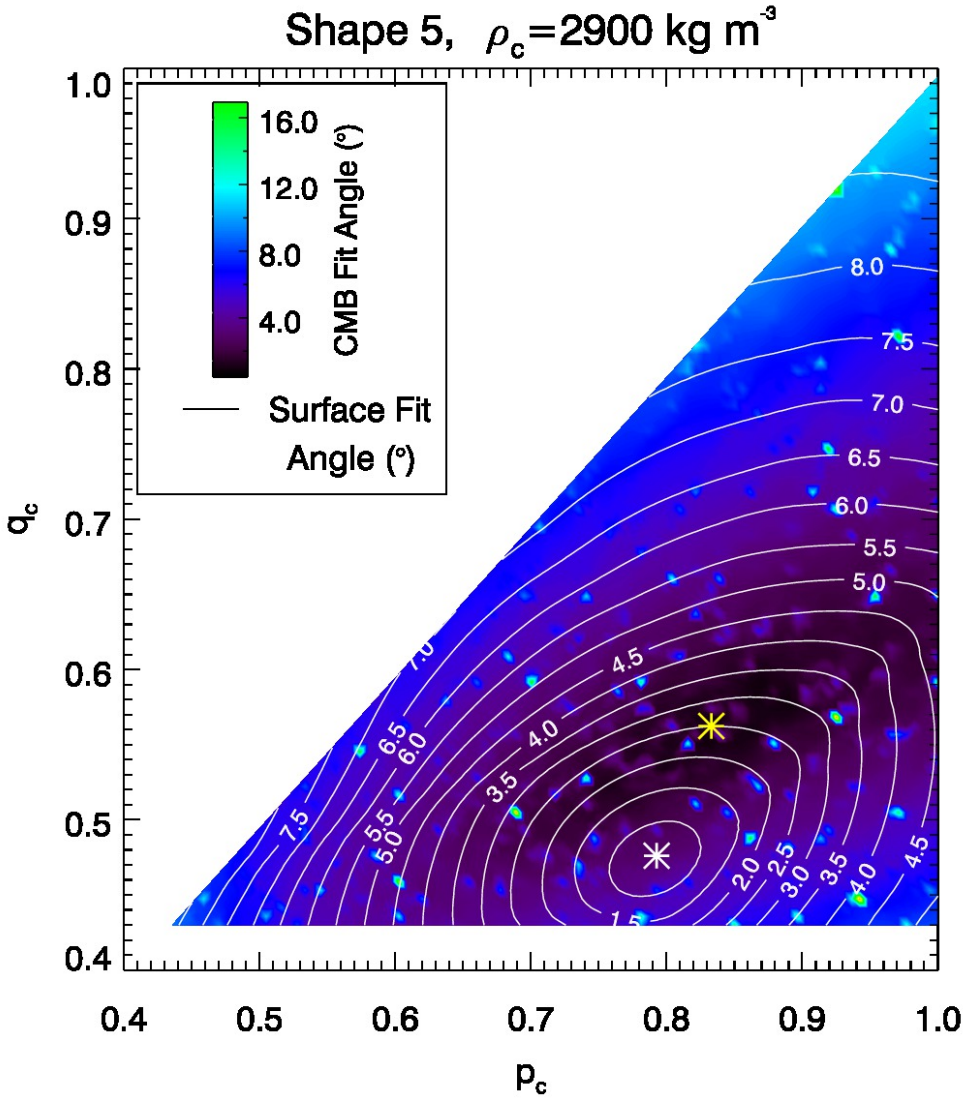

Figure 4.25: Same as Figure 4.23, Except for a Core Density of 2900 kg m^{-3}.

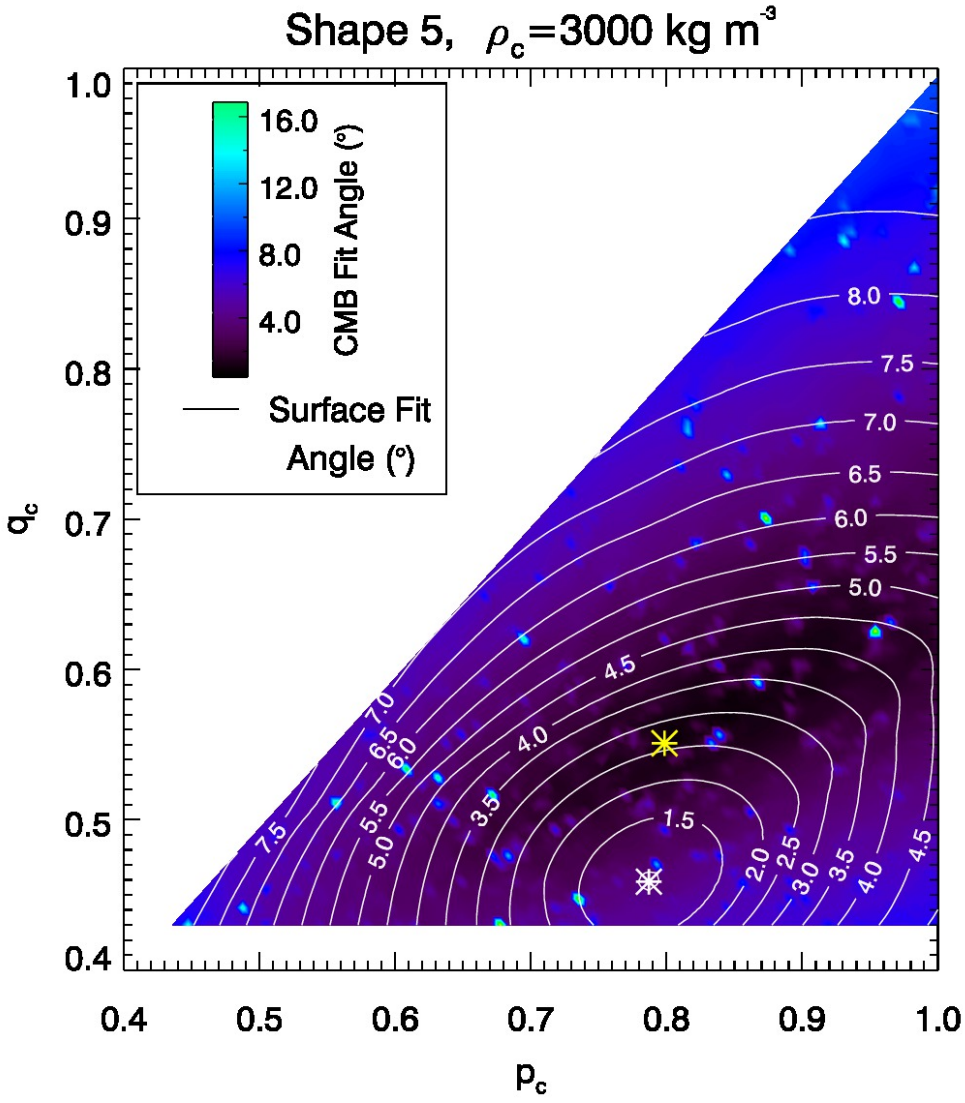

Figure 4.26: Same as Figure 4.23, Except for a Core Density of 3000 kg m^{-3}.

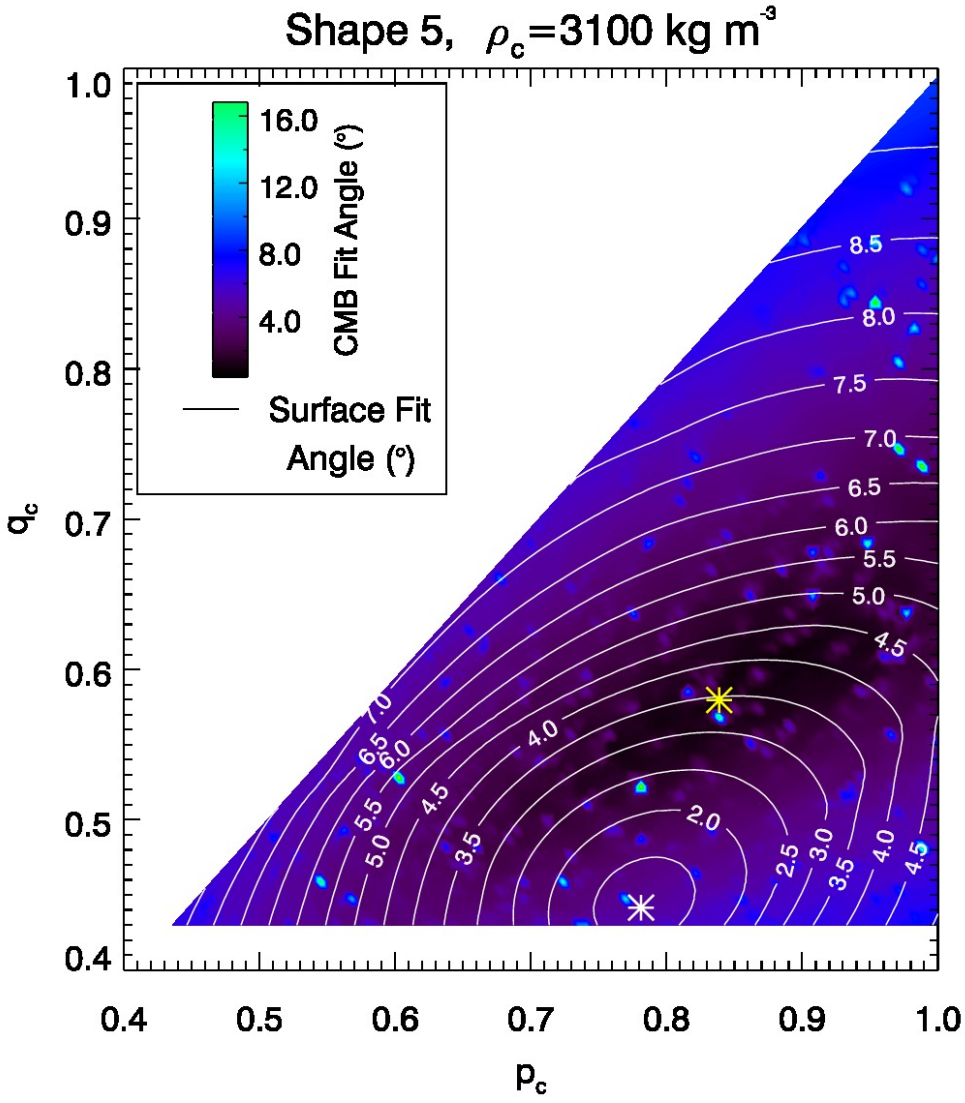

Figure 4.27: Same as Figure 4.23, Except for a Core Density of 3100 kg m^{-3}.

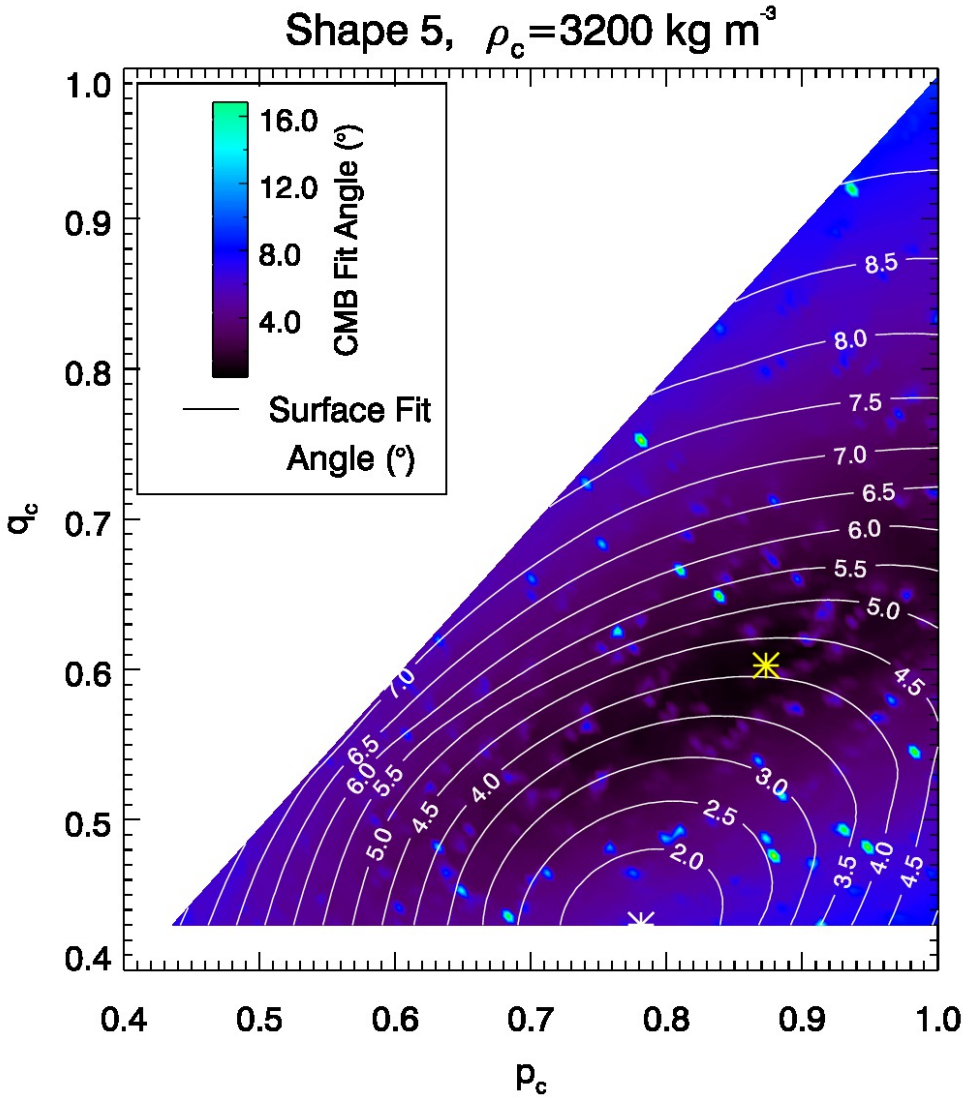

Figure 4.28: Same as Figure 4.23, Except for a Core Density of 3200 kg m^{-3}.

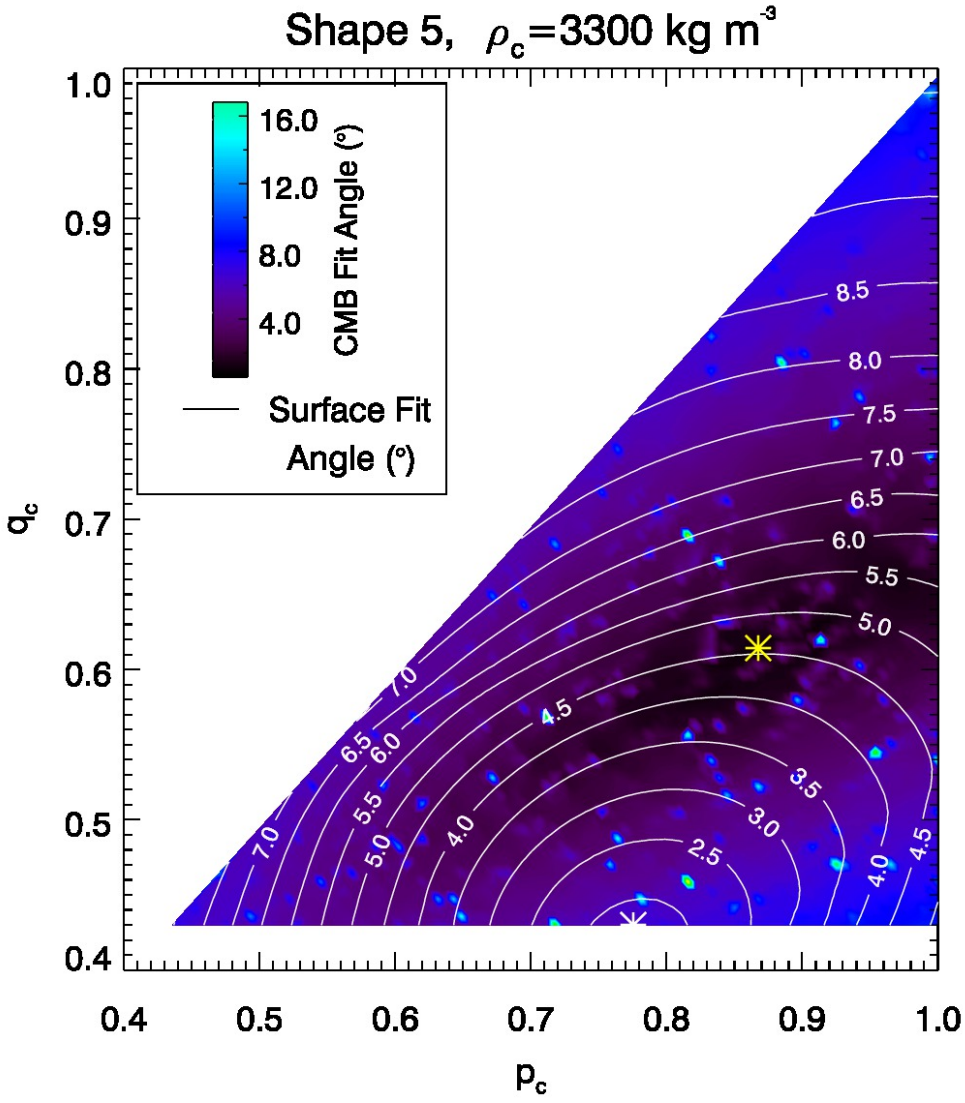

Figure 4.29: Same as Figure 4.23, Except for a Core Density of 3300 kg m^{-3}.

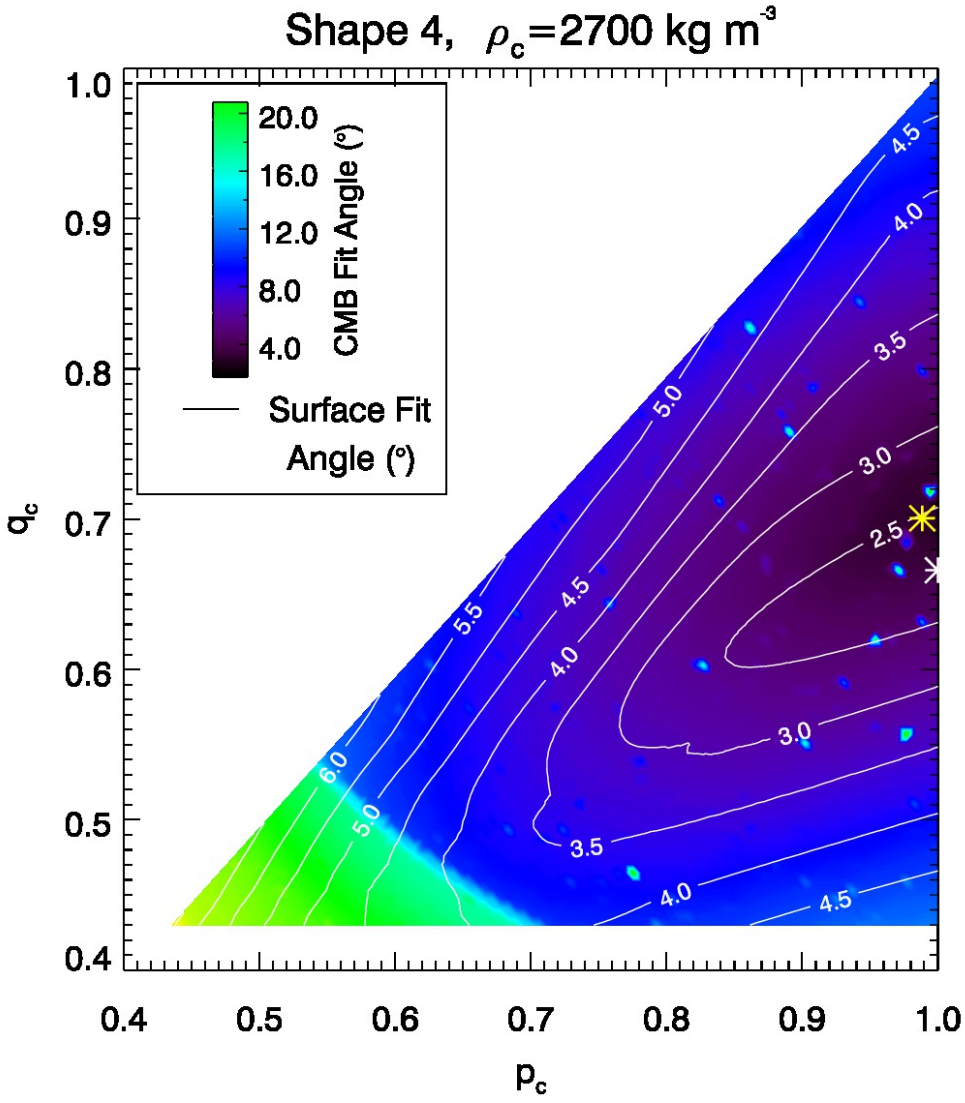

Figure 4.30: Same as Figure 4.23, but for Shape 4.

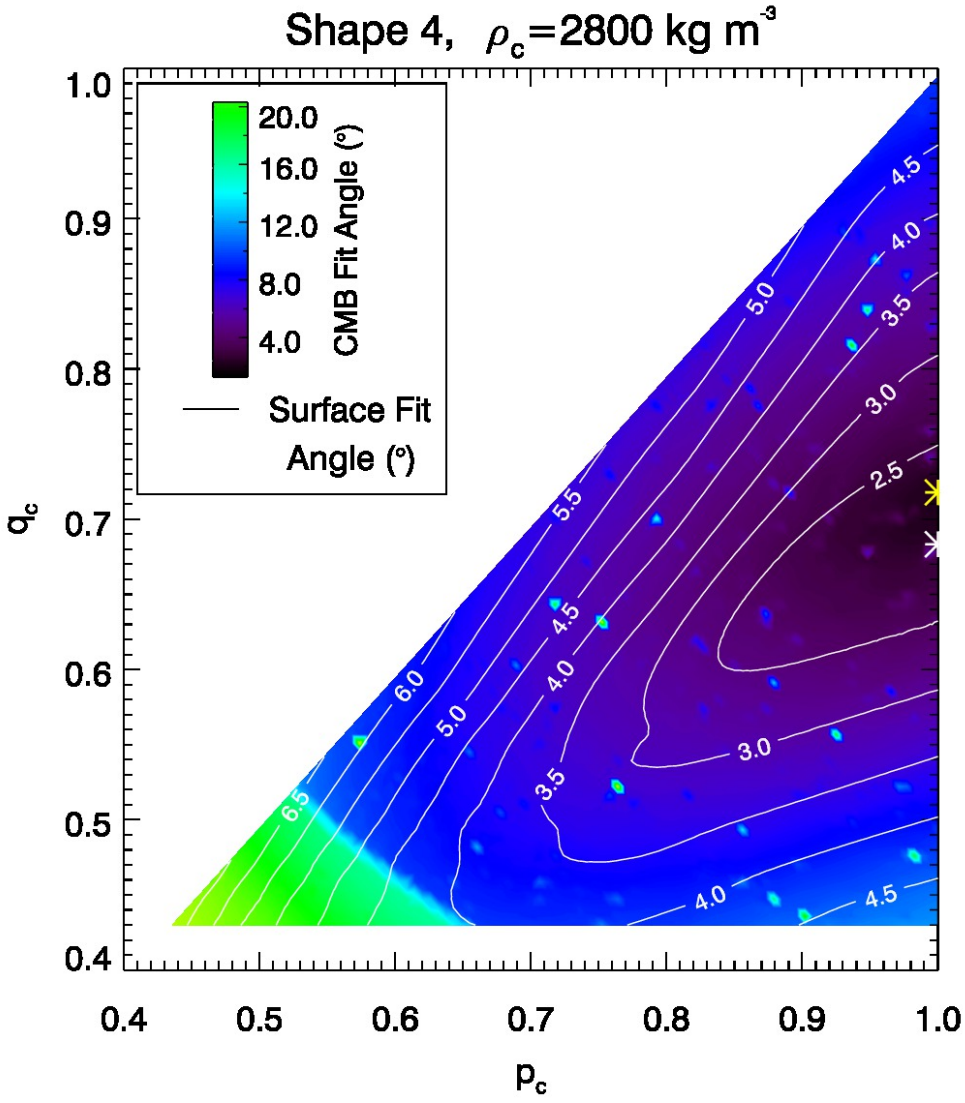

Figure 4.31: Same as Figure 4.30, Except for a Core Density of 2800 kg m^{-3}.

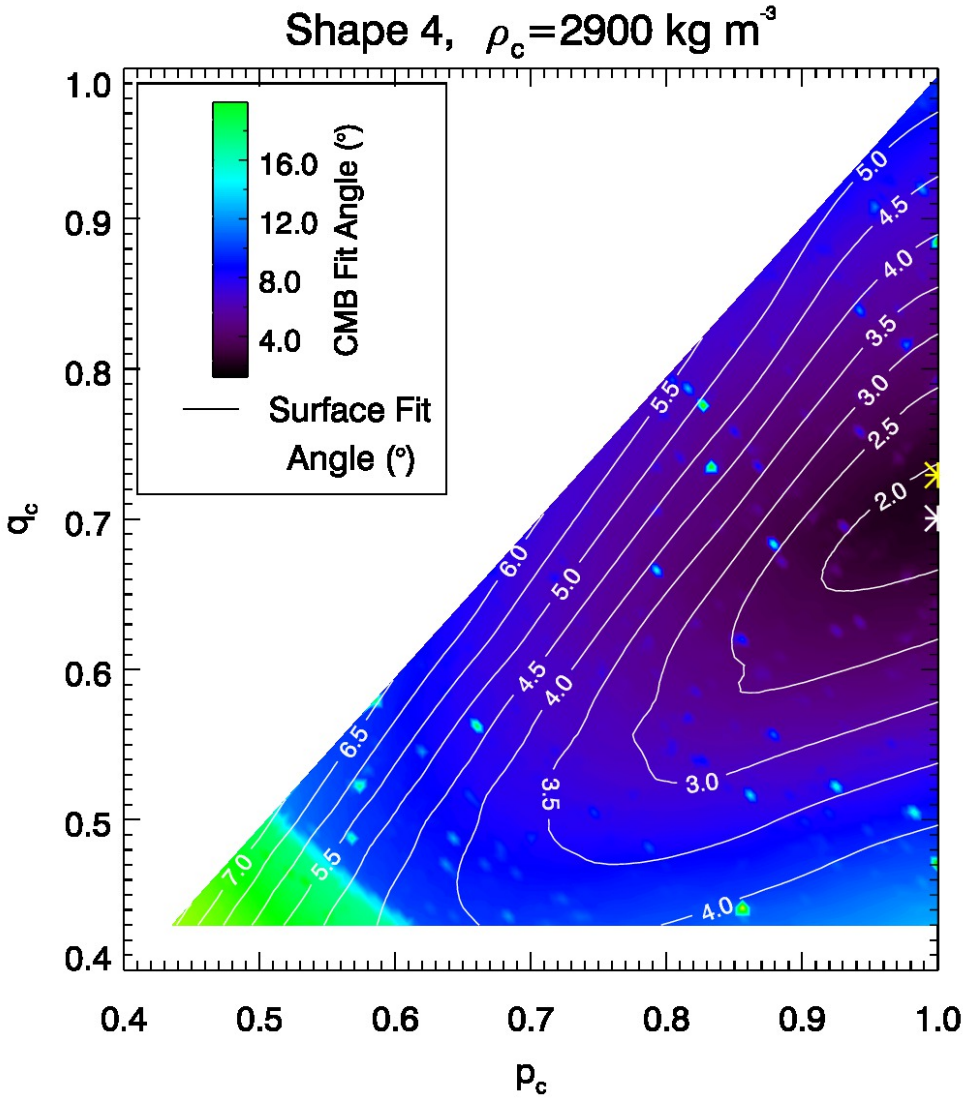

Figure 4.32: Same as Figure 4.30, Except for a Core Density of 2900 kg m^{-3}.

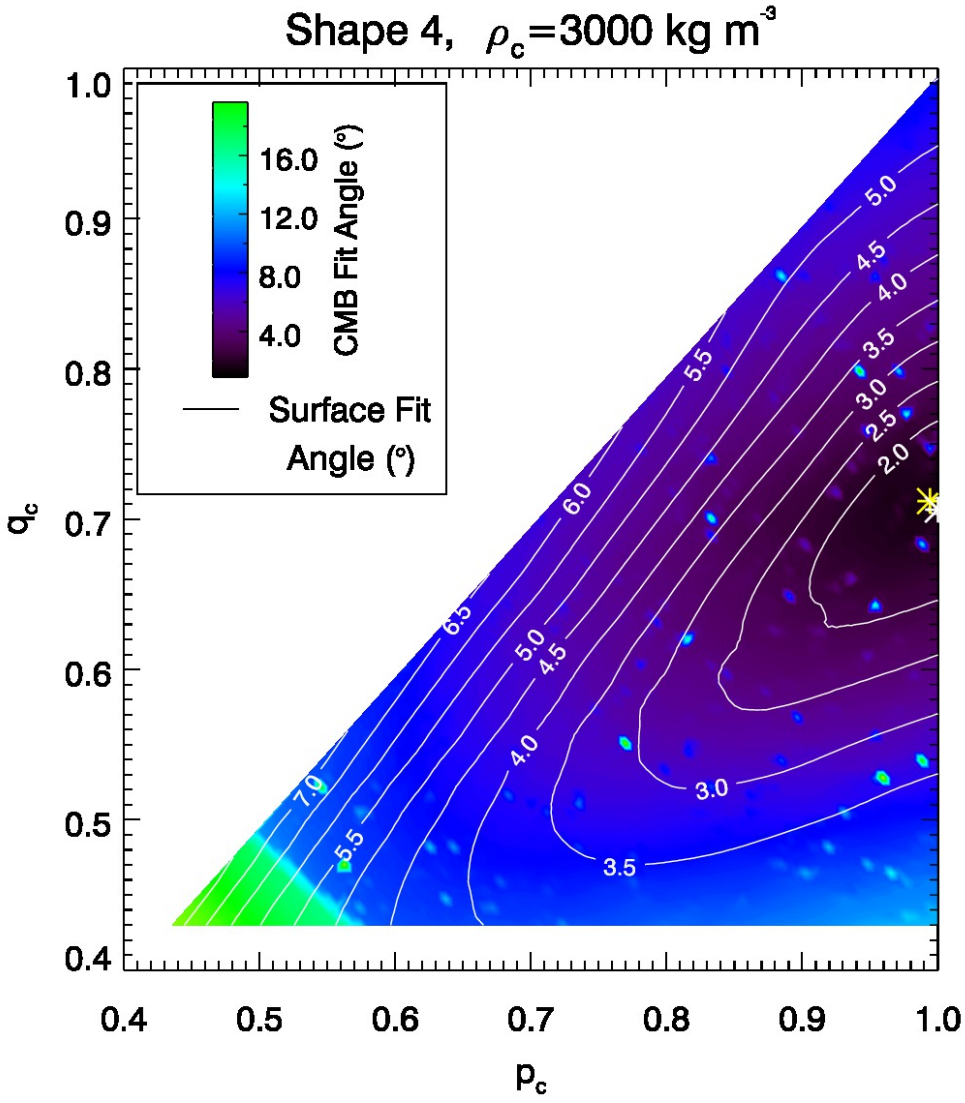

Figure 4.33: Same as Figure 4.30, Except for a Core Density of 3000 kg m^{-3}.

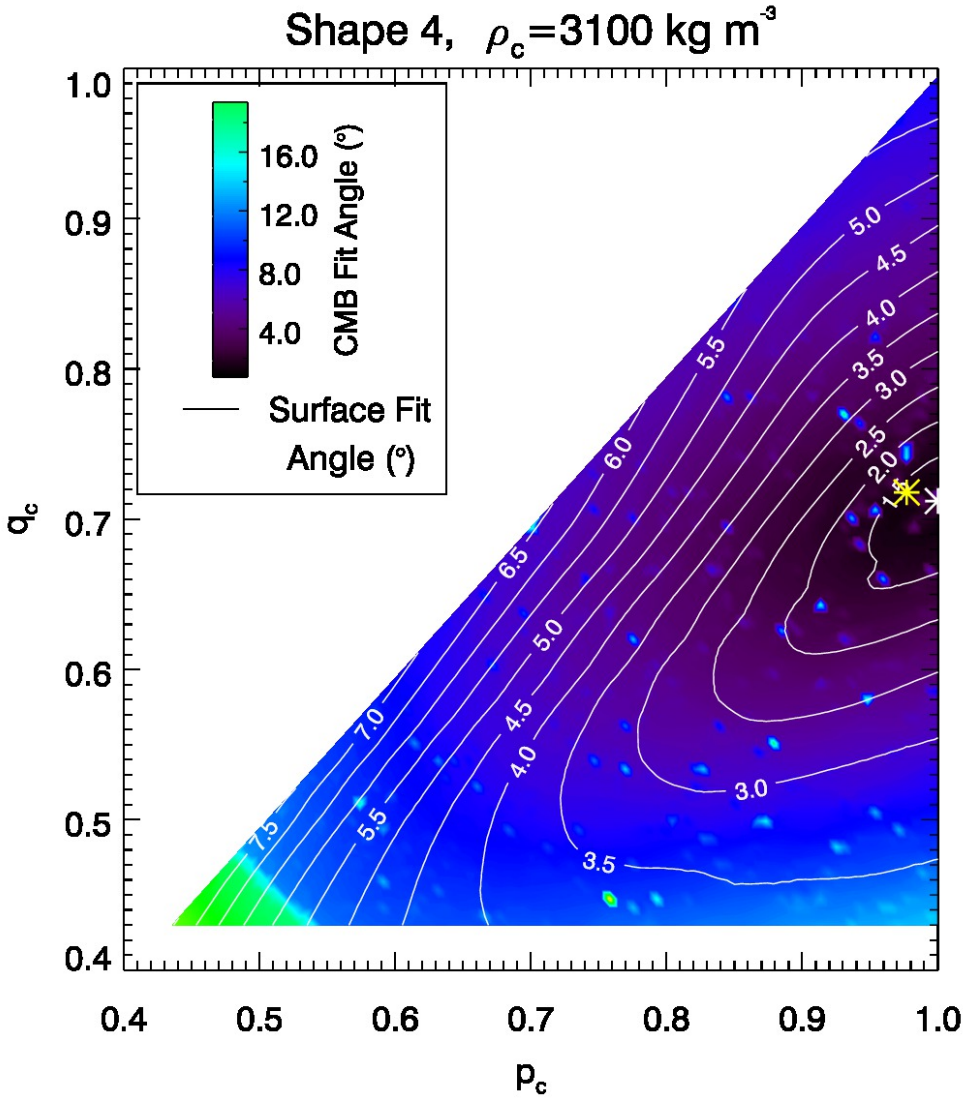

Figure 4.34: Same as Figure 4.30, Except for a Core Density of 3100 kg m^{-3}.

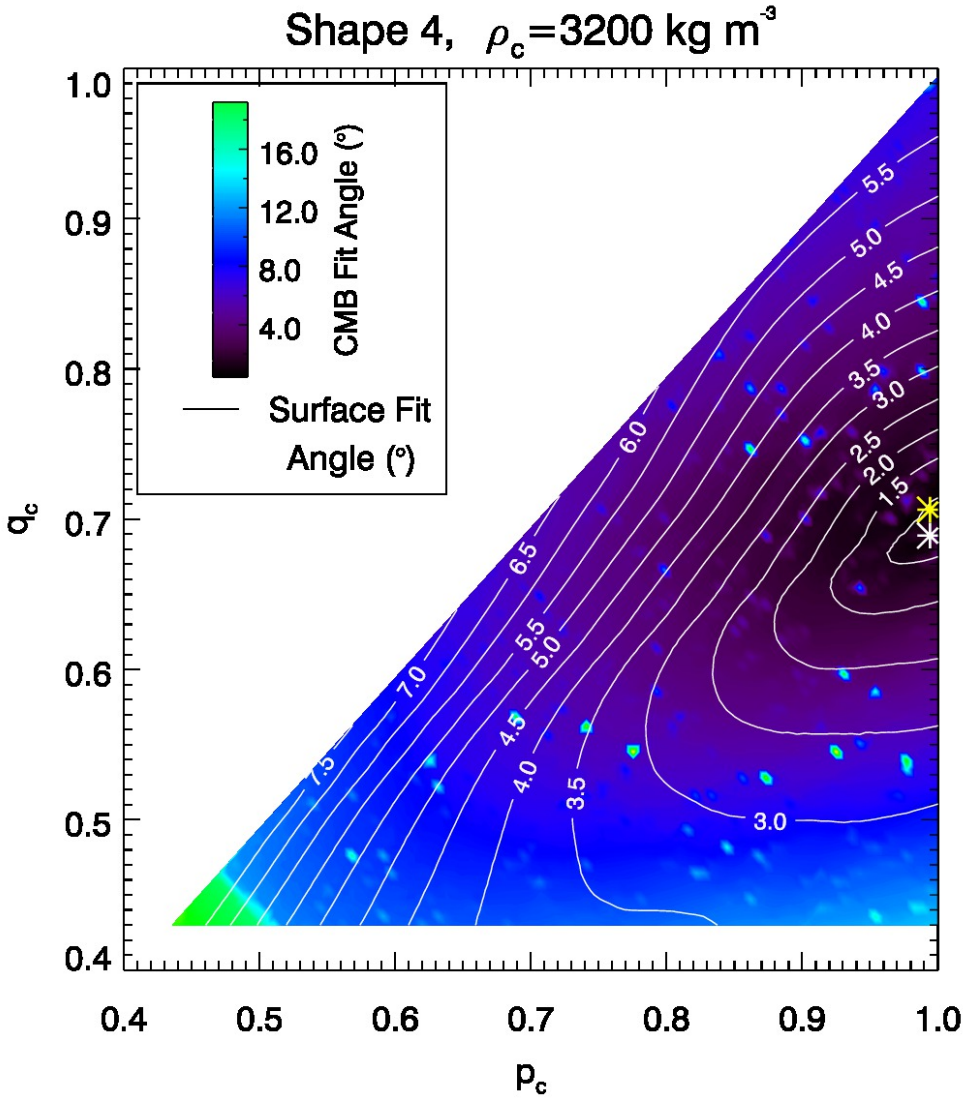

Figure 4.35: Same as Figure 4.30, Except for a Core Density of 3200 kg m^{-3}.

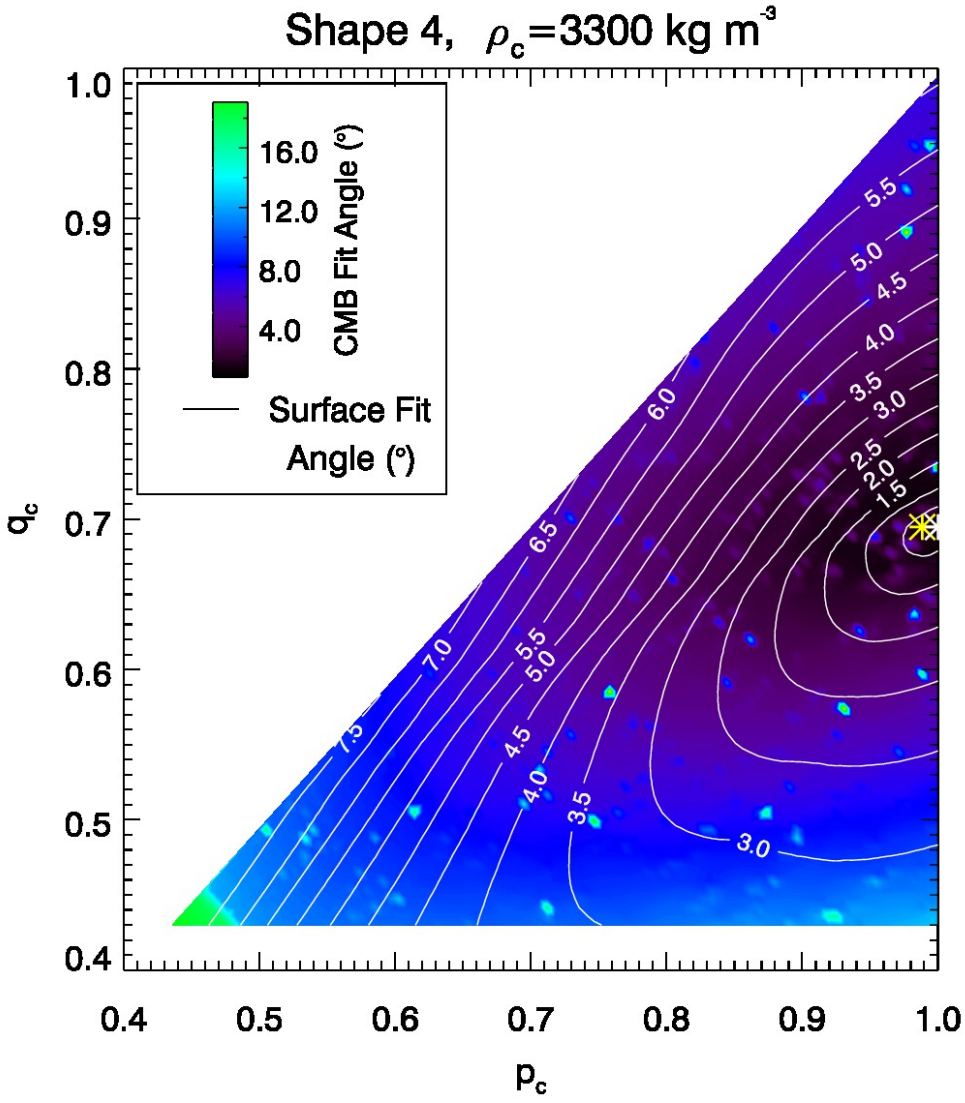

Figure 4.36: Same as Figure 4.30, Except for a Core Density of 3300 kg m^{-3}.

core densities ≥ 2900 kg m^{-3} do not present viable solutions. Shape 4, however, is unlikely to be the true shape of Haumea, because as a Maclaurin spheroid, it does not present varying areas to the observer as it rotates, like a Jacobi ellipsoid does, in order to produce a light curve like Haumea's, and it would require implausible albedo variations to mimic the light curve. For the ellipsoid cases that we investigated (shapes 1, 2, and 5), none show results to within the code's precision. This implies that for an ellipsoidal outer shape, only a very homogeneous body with near uniform density is a hydrostatic equilibrium solution.

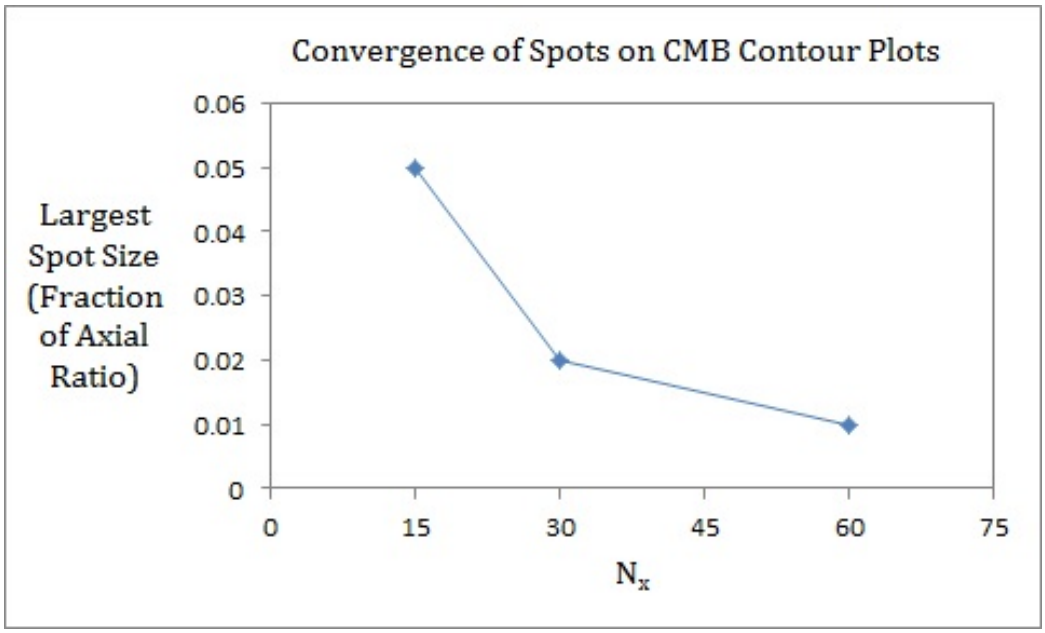

Figure 4.37: The Relationship Between Largest Spot Size (Measured in Terms of Axial Ratios from the Contour Plots) and the Resolution N_x. If the Spots Are Caused by the Bumpiness of the CMB, Then This Graph Shows a Convergence of the Surface with Higher Resolution.

Chapter 5

CONCLUSIONS

5.1 Review

Haumea's surface of pure water ice (Trujillo et al. 2007) and bulk density of 2600 kg m^{-3} (Lockwood et al. 2014) are surprising features, and seemingly contradictory at first glance. The surface ice must take up a very small amount of the bulk volume of Haumea, while the rest of it must be a core of denser rock. Its surface features apparently belie a very different interior.

Haumea displays a 3.1954-hour periodic light curve, which is double-peaked with a magnitude variation of $\Delta m = 0.28$ (R06). Because its surface displays a lack of significant spectral variation and uniformly deep water-ice absorption features (Pinilla-Alonso et al. 2009), its light curve must be the result of Haumea having an oblong shape, specifically one consistent with a Jacobi ellipsoid in hydrostatic equilibrium. This shape presents a changing area to the observer as it rotates, and its equatorial axial ratio has been measured from the light curve to be $p = b/a = 0.80$ (Lockwood et al. 2014). Jacobi's relation for a triaxial Jacobi ellipsoid in equilibrium was used to estimate the polar axial ratio as $q = c/a = 0.52$ (Lockwood et al. 2014), under the assumption that Haumea is uniform in density. But Haumea cannot be uniform in density and also consist of a rocky core with an icy mantle.

We addressed this problem by writing a code which simulated a two-phase ellipsoid, made up of a core with silicate-like density in the range 2700 to 3300 kg m^{-3} and a mantle coating with ice-like density of 935 kg m^{-3}. We discretized the space making up this ellipsoid and then altered the core's axial ratios $p_c = b_c/a_c$ and

$q_c = c_c/a_c$ to let it take every shape subject to the constraint for Jacobi ellipsoids: $0.43 \leq q_c < p \leq 1$. All other parameters (angular velocity, density of core and mantle, outer surface dimensions) were kept fixed. We then calculated the angle of fit between the downward surface normal and the total acceleration vector (including gravity and centrifugal force), averaged over selected points around the entire surfaces, both the outer surface and the CMB. If Haumea is in hydrostatic equilibrium, then the outer surface and the CMB should both conform to equipotential surfaces. Therefore, the core shape that simultaneously minimizes both the average surface fit angle and the average CMB fit angle will be a solution to a possible configuration of Haumea.

Upon taking a full range of core shapes and densities into consideration for a variety of outer shapes of Haumea (shapes 1–5 from Table 4.1), shape 4 (from R06) with a core density of 3200–3300 kg m^{-3} and shape 5 (which represents Lockwood et al.ś (2014) measurements) with a core density of 2700–2800 kg m^{-3} emerged as the two best solutions (ignoring shape 1 due to its similarity to shape 5). The low density shape 5 configuration (surface and CMB) matched up to an equipotential surface to within 3 times our code's precision, while the high core density shape 4 configuration displayed a match of its outer and CMB to equipotential surfaces to within our code's precision. For shape 5, our equipotential metric differs from a match by several percent if $\rho_c > 2800$ kg m^{-3}.

While a Maclaurin spheroid with a high density, 3300 kg m^{-3} core such as shape 4 may prove to be a stable solution, it is unlikely to be Haumea's actual shape. The reason is because the only way for an equatorially symmetric body like a Maclaurin spheroid to produce the symmetrical double-peaked light curve that Haumea exhibits would be for its surface to display roughly equal surface heterogeneities on perfectly antipodal points along the equator. While this is within the realm of possibility, it is probabilistically very unlikely. Therefore, the most likely shape to produce Haumea's

observed light curve is a Jacobi ellipsoid. Our results show that a Jacobi ellipsoid such as shape 2 displays no stability for any core density, but that an ellipsoid with axial ratios corresponding to shape 1 and shape 5 does exhibit stability for core densities less than about 2700–2800 kg m^{-3}. Since shape 1 and shape 5 have very similar dimensions, only shape 5 will be discussed here, as it is a more robust solution to Haumea's shape taken from more recent and more stringent measurements (Lellouch et al. 2010, Lockwood et al. 2014).

5.2 Discussion

I conclude that Haumea most likely has a triaxial Jacobi ellipsoid shape very similar to shape 5, with a low core density no greater than 2700 to 2800 kg m^{-3}. This configuration represents the most likely outer shape, as well as the most stable outer shape and core shape with respect to the gravitational/rotational equipotential. In this configuration, Haumea's outer radial axes are $a = 960$ km, $b = 770$ km, and $c = 495$ km, with c also doubling as the rotation axis. The axial ratios of this outer shape are then $(p, q) = (0.802, 0.516)$. If the core density is 2700 kg m^{-3}, then the core shape that optimizes the surface fit angle (at a value of 0.266°) has axial ratios $(p_c, q_c) = (0.798, 0.499)$, very close in shape to the outer surface. Assuming the core axes are aligned with the outer surface axes, the radial axis dimensions for the core under these conditions are $a_c = 956$ km, $b_c = 763$ km, and $c_c = 477$ km. This would lead to ice thicknesses of only 4 km over the a axis, just 7 km over the b axis, and 18 km at the poles. This configuration of Haumea is shown in Figures 5.1 and 5.2, in polar and equatorial cross sectional views.

The mass error in this particular run of the code (shape 5 with $\rho_c = 2700$ kg m^{-3}, $N_x = 60$) was 0.06%, and the core mass would be 3.93×10^{21} kg, as compared to 3.58×10^{21} kg, as calculated by Cook et al. (2011). If the silicate mass fraction f for

an ellipsoid is calculated with the following equation,

$$f = \frac{\rho_{\text{core}}}{\rho_{\text{mantle}}\left(\frac{abc}{a_c b_c c_c} - 1\right) + \rho_{\text{core}}}, \tag{5.1}$$

then in the case of core density being 2700 kg m^{-3}, Haumea's silicate mass fraction is 98.2%. This contrasts with silicate mass fractions of 72% for Pluto and 65% for Eris, according to models by Hussmann et al. (2006).

From Figures 5.1 and 5.2, it is clear that Haumea's interior is remarkably uniform and possesses very low density for silicates, which typically have densities around 3300 kg m^{-3}. This may mean the core consists of hydrated silicate. Desch and Neveu (2015) predict that Haumea has a core made up of hydrated silicates at a density of 2900 kg m^{-3}. This prediction follows calculations in which they assumed that following an impact of two large differentiated progenitor bodies, the core contained some ice. As per the discussion below in Section 5.3, following the impact, the rock and water reacted to form serpentines and underwent convection, which homogenized and thoroughly hydrated the interior (Desch & Neveu 2015).

The ice crust is extremely thin, which becomes more apparent from the figures. It is especially thin over the equator (less than 10 km) and it is at its thinnest over the long (a) axis, as little as 4 km. The Dark Red Spot is along the equator, and while not directly over the a axis, it does lie over some of the thinnest ice regions. Since the ice fraction by mass is less than 2%, we can approximate Haumea to be uniform in density, thus the use of Jacobi's formula to aid in calculating Haumea's dimensions and bulk density is still valid.

It is also strikingly apparent from Figure 5.1 just how flattened Haumea is in the polar direction. When compared to the $a - b$ cross section in Figure 5.2, we see that Haumea is much more elongated in the polar direction than in the equatorial plane, in which it is significantly rounder. Yet this is the shape for this particular a, b, angular

velocity, and bulk density that is in hydrostatic equilibrium, according to Jacobi's formula.

If Haumea's core density were 2800 kg m^{-3} instead of 2700 kg m^{-3}, the configuration will change slightly. For this core density, the minimum surface fit angle (of 0.407°) occurs for a core shape of $(p_c, q_c) = (0.793, 0.488)$, and with axes of $a_c = 948$ km, $b_c = 752$ km, and $c_c = 463$ km. This core shape leads to ice thicknesses of 12 km over the a axis, 18 km over the b axis, and 32 km over the poles. The ice with a core density of 2800 kg m^{-3} is thicker everywhere since the core would be smaller, in order to allow the total density of Haumea to remain 2600 kg m^{-3}. For this particular shape of the core, the calculated mass error is 0.22%, and the mass of the core is 3.87×10^{21} kg. The silicate mass fraction for this configuration is 96.5%, leaving us with a significantly larger fraction of ice. The uniform density approximation may still be made, but it is a weaker assumption than with $\rho_c = 2700$ kg m^{-3}. Based on our results, I would not expect the core density to be much higher than 2800 kg m^{-3}.

In ascertaining whether the core density is more likely to be 2700 kg m^{-3} or 2800 kg m^{-3} for shape 5, the minimum fit angles for both the surface and the CMB are clues. For $\rho_c = 2700$ kg m^{-3}, the minimum surface fit angle is 0.266° and the minimum CMB fit angle is 0.488°. But for $\rho_c = 2800$ kg m^{-3}, the minimum surface fit angle is 0.407° while the minimum CMB fit angle is 0.518°. At this resolution ($N_x = 60$), the accuracy of the code was determined to be about 0.4°, and while both surface fit angles are close to this, the smallest fit angles are both for a core density of 2700 kg m^{-3}. There is an expectation that the core density is actually lower than this still, but if the core density was much smaller, the equations I use to calculate the core axes (i.e. Equation 3.5 and associated formulas) will generate a core with dimensions exceeding those of the outer surface. Deviations of p_c and q_c from the homeoidal core shape are less possible with decreasing core density, so that

the density of the core material is probably no less than 2650 kg m^{-3}. Since I have tested the core densities at intervals of 100 kg m^{-3}, and because 2600 kg m^{-3} is an unattainably low density, 2650–2700 kg m^{-3} seems a very likely lower limit to the core density from my calculations.

It should be stressed that I based the core axis calculations for Figures 5.1 and 5.2 on the minimum fit angle for the outer surface, and not that of the CMB. This is primarily because the minimum was more sharply visible for the outer surface plot, as opposed to the flat, spread out CMB plot, where there is a large area of similar value around the minimum CMB fit angle. If the core axes were calculated for the CMB minimum fit angle, then the ice would be thinnest at the poles and thicker over the equator (restricting this discussion to the case of shape 5 with a core density of 2700 kg m^{-3}).

The possibility that the Dark Red Spot is an impact scar is intriguing. Revisiting ice thicknesses from above, if the core density is 2700 kg m^{-3} the ice thickness of the mantle ranges from 4–18 km, and if the core density is 2800 kg m^{-3} the ice thickness ranges from 12–32 km. This ice thickness is too small to avoid significant losses by impacts, especially over the equator. Rubin et al. (2014) calculate that the probability of an impact of an object greater than 15 km onto a Charon-sized target to be less than 10^{-3} in the first billion years of the Solar System. Haumea's radius is 18% larger than Charon's, which makes its cross-sectional area 40% larger, yet Haumea is likely to have a similar impact probability to Charon's in the first billion years of the Solar System (see Theories on Haumea's Origin, Chapter 1). The DRS is likely to be a more recent scar, though, if it is one at all. Since the Late Heavy Bombardment, there may have been approximately only 1 impact by an object with diameter $\geq$ 15 km onto a body as large as Haumea in the Kuiper Belt (Rubin et al. 2014). Impactors with sizes of a few km across were probably very common, however, and such impactors would

have preferentially removed the ice at the equator. Therefore, cratering considerations allow us to set a rough lower limit to the core density of $\rho_c \gtrsim 2800$ kg m^{-3}. From the calculations in this work, a rough upper limit to the core density can be set of $\rho_c \lesssim 2800$ kg m^{-3}. Using these arguments, we can conclude that the most likely core density of Haumea is $\rho_c \approx 2800$ kg m^{-3}.

5.3 Implications

The fact that Haumea shows a closer match to equipotential surfaces with a lower core density suggests much about its formation history. If $\rho_c = 2700$ kg m^{-3}, then the core would most likely consist of a hydrated silicate, perhaps hydrated olivine. This would suggest much mixture between water and silicate in the past.

Desch and Neveu (2015) provide a scenario that may explain our current picture of Haumea. They propose a collision which merges two progenitor bodies, each with radius 650 km and bulk density 2000 kg m^{-3}, sometime during the Late Heavy Bombardment period. If this collision occurred around this timeframe, then the progenitor bodies will have had time for radioactive decay to allow for heating and differentiation into structures with rocky cores, icy mantles, and thin crusts composed of an undifferentiated rock/ice mixture. During the collision, Desch and Neveu propose that the cores merged and that the undifferentiated crusts and most of the icy mantles were ejected. Immediately after the impact, ice is melted throughout the interior, almost all the way to the surface. After the collision, Haumea would consist of a core composed of mostly rock and some ice, with a very thin ice mantle, only tens of kilometers thick. Hydrothermal circulation throughout the core would then fully hydrate the rock, and the rock and water would react to form serpentines. Convection would uniformly mix and homogenize the core, while also cooling the interior and preventing temperatures from rising high enough to dehydrate the rock. Their conclusion is that

Haumea would end up with a core density of 2900 kg m^{-3} and a bulk density of 2530 kg m^{-3}. If some more ice convects in, which may be likely, this can further lower the core density, leading to numbers which conform with this work's conclusions.

That almost all but not all of the ice was ejected is an interesting occurrence. One possibility may be that all of the ice was ejected and the ice present now was emplaced later. This may have happened via outgassing of water from the interior.

According to our calculations, the ice mantle appears to be at its thinnest over the equator, specifically over the a axis. This may allow some material to show through from beneath the ice, especially if the Dark Red Spot is an impact scar. Though this has been ruled out as a topographic feature (Lacerda 2010), it could be a topographically relaxed impact scar.

5.4 Caveats and Future Work

Several assumptions and potential limitations were applied to Haumea in this work that may have implications on future work that can be done. First of all, it was assumed that the core axes are aligned with the outer surface axes. Perhaps Haumea's rapid rotation rate has caused the a axis of the outer surface to lag behind the a_c axis of the core. If the axes are actually misaligned, then significant changes must be made to the equations that were used to calculate the core axes. An angular term must be introduced to allow the core to be rotated with respect to the outer surface. The outer surface shape will remain fixed, but the more the core is rotated, the more the a_c axis will be limited to smaller lengths. This may allow p_c to approach values closer to 1, and it may also change the nature of Haumea's equilibrium state.

This leads to consideration of another assumption that was made in this work, namely that Haumea is in a state of hydrostatic equilibrium. If it turns out that Haumea is not in hydrostatic equilibrium, then that would change our assumption

about the metric our code calculates. The surface normal would not necessarily be parallel to the gravity vector at any given point, on the outer surface or on the core-mantle boundary. It then would make the conclusions in this work less valid, though our results would still serve to narrow down the core density, shape, and size in a general manner. If Haumea is not in hydrostatic equilibrium, that may also imply that its CMB is not a sharp boundary.

Future considerations should not only include misalignment of the axes and deviations from hydrostatic equilibrium, but also a closer look at the implications of the minimum fit angle for the CMB contour plots. If the CMB is a well-defined boundary within Haumea, then a further development of how baroclinicity and vorticity affect the stability of that boundary could be performed. This may affect our interpretation that the thinnest ice is on the equator, and we may end up finding the thinnest ice over the poles.

5.5 Final Thoughts

Because of its collisional family and its unusual interior structure, Haumea is one of the most important objects to study in that it may provide our best opportunity to see the inside of a KBO. Understanding the makeup of a KBO can further help us understand how KBOs and other objects may have formed in that part of the solar system. Understanding further details of Haumea's impact history may also shed further light on how populated the Kuiper Belt may have been at certain times. The upcoming flyby this summer of the New Horizons spacecraft past Pluto, the other known multiple KBO system, may shed more light on these questions. This will be our first close encounter with a KBO, and perhaps it will allow us to gain new insights into Haumea. We are standing on the edge of knowing our outer solar system better than we have ever known it before.

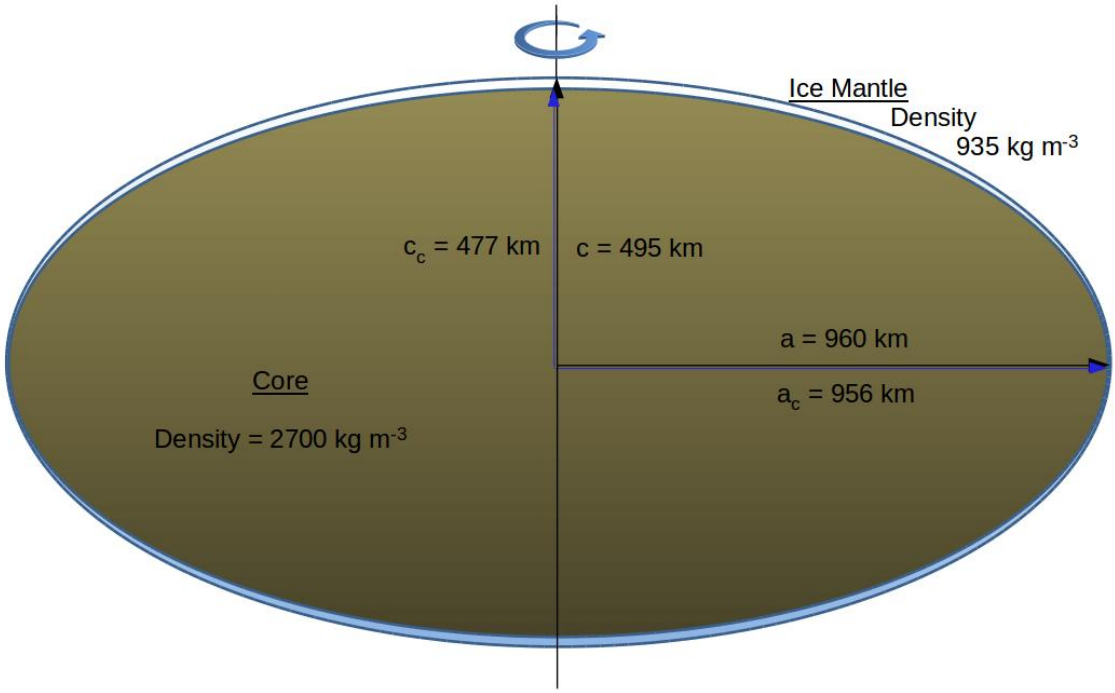

Figure 5.1: Vertical Cross Section of Haumea (the $a - c$ Section).

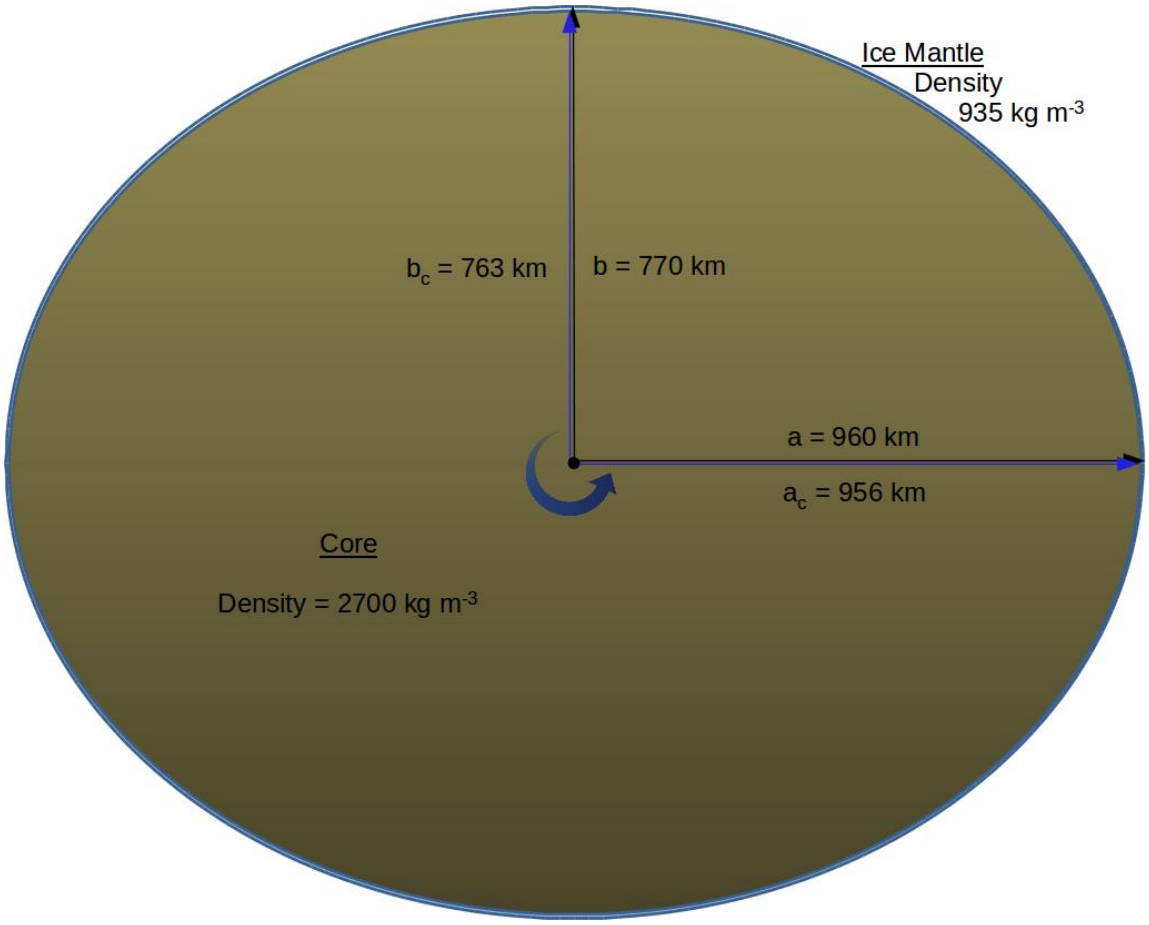

Figure 5.2: Horizontal Cross Section of Haumea, Cut Through the Equatorial Plane (the $a - b$ Section).

REFERENCES

Anderson, J. D., R. A. Jacobson, T. P. McElrath, W. B. Moore, G. Schubert and P. C. Thomas, "Shape, Mean Radius, Gravity Field, and Interior Structure of Callisto", Icarus **153**, 157–161 (2001).

Barkume, K. M., M. E. Brown and E. L. Schaller, "Water Ice on the Satellite of Kuiper Belt Object 2003 EL_{61}", Astrophysical Journal, Letters **640**, L87–L89 (2006).

Binney, J. and S. Tremaine, *Galactic Dynamics: Second Edition* (Princeton University Press, 2008).

Braga-Ribas, F., B. Sicardy, J. L. Ortiz, E. Lellouch, G. Tancredi, J. Lecacheux, R. Vieira-Martins, J. I. B. Camargo, M. Assafin, R. Behrend, F. Vachier, F. Colas, N. Morales, A. Maury, M. Emilio, A. Amorim, E. Unda-Sanzana, S. Roland, S. Bruzzone, L. A. Almeida, C. V. Rodrigues, C. Jacques, R. Gil-Hutton, L. Vanzi, A. C. Milone, W. Schoenell, R. Salvo, L. Almenares, E. Jehin, J. Manfroid, S. Sposetti, P. Tanga, A. Klotz, E. Frappa, P. Cacella, J. P. Colque, C. Neves, E. M. Alvarez, M. Gillon, E. Pimentel, B. Giacchini, F. Roques, T. Widemann, V. S. Magalhães, A. Thirouin, R. Duffard, R. Leiva, I. Toledo, J. Capeche, W. Beisker, J. Pollock, C. E. Cedeño Montaña, K. Ivarsen, D. Reichart, J. Haislip and A. Lacluyze, "The Size, Shape, Albedo, Density, and Atmospheric Limit of Transneptunian Object (50000) Quaoar from Multi-chord Stellar Occultations", Astrophysical Journal **773**, 26 (2013).

Brown, M., K. Barkume, B. Reach, J. Stansberry and C. Trujillo, "Characterization of the Icy Planetoids of the Outer Solar System", Spitzer Proposal (2004).

Brown, M. E., "On the Size, Shape, and Density of Dwarf Planet Makemake", Astrophysical Journal, Letters **767**, L7 (2013).

Brown, M. E., K. M. Barkume, D. Ragozzine and E. L. Schaller, "A Collisional Family of Icy Objects in the Kuiper Belt", Nature **446**, 294–296 (2007).

Brown, M. E., A. H. Bouchez, D. Rabinowitz, R. Sari, C. A. Trujillo, M. van Dam, R. Campbell, J. Chin, S. Hartman, E. Johansson, R. Lafon, D. Le Mignant, P. Stomski, D. Summers and P. Wizinowich, "Keck Observatory Laser Guide Star Adaptive Optics Discovery and Characterization of a Satellite to the Large Kuiper Belt Object 2003 EL_{61}", Astrophysical Journal, Letters **632**, L45–L48 (2005a).

Brown, M. E. and E. L. Schaller, "The Mass of Dwarf Planet Eris", Science **316**, 1585 (2007).

Brown, M. E., C. A. Trujillo and D. L. Rabinowitz, "Discovery of a Planetary-Sized Object in the Scattered Kuiper Belt", Astrophysical Journal, Letters **635**, L97–L100 (2005b).

Brown, M. E., M. A. van Dam, A. H. Bouchez, D. Le Mignant, R. D. Campbell, J. C. Y. Chin, A. Conrad, S. K. Hartman, E. M. Johansson, R. E. Lafon, D. L. Rabinowitz, P. J. Stomski, Jr., D. M. Summers, C. A. Trujillo and P. L. Wizinowich, "Satellites of the Largest Kuiper Belt Objects", Astrophysical Journal, Letters **639**, L43–L46 (2006).

Buie, M. W., W. M. Grundy, E. F. Young, L. A. Young and S. A. Stern, "Orbits and Photometry of Pluto's Satellites: Charon, S/2005 P1, and S/2005 P2", Astronomical Journal **132**, 290–298 (2006).

Carry, B., C. Snodgrass, P. Lacerda, O. Hainaut and C. Dumas, "Characterisation of Candidate Members of (136108) Haumea's Family. II. Follow-up Observations", Astronomy and Astrophysics **544**, A137 (2012).

Chandrasekhar, S., *Ellipsoidal Figures of Equilibrium* (New York: Dover, 1987).

Cook, J. C., S. J. Desch and M. Rubin, "The Black Sheep of Haumea's Collisional Family", in "Lunar and Planetary Science Conference", vol. 42 of *Lunar and Planetary Science Conference*, p. 2503 (2011).

Desch, S. J., J. C. Cook, T. C. Doggett and S. B. Porter, "Thermal Evolution of Kuiper Belt Objects, with Implications for Cryovolcanism", Icarus **202**, 694–714 (2009).

Desch, S. J. and M. Neveu, "On the Origin of Haumea", in "Lunar and Planetary Science Conference", vol. 46 of *Lunar and Planetary Science Conference*, p. 2082 (2015).

Dumas, C., B. Carry, D. Hestroffer and F. Merlin, "High-Contrast Observations of (136108) Haumea. A Crystalline Water-Ice Multiple System", Astronomy and Astrophysics **528**, A105 (2011).

Farinella, P., P. Paolicchi, E. F. Tedesco and V. Zappala, "Triaxial Equilibrium Ellipsoids among the Asteroids", Icarus **46**, 114–123 (1981).

Fraser, W. C. and M. E. Brown, "Quaoar: A Rock in the Kuiper Belt", Astrophysical Journal **714**, 1547–1550 (2010).

Holton, J. R., *An Introduction to Dynamic Meteorology* (Academic Press, 1992).

Hussmann, H., F. Sohl and T. Spohn, "Subsurface Oceans and Deep Interiors of Medium-Sized Outer Planet Satellites and Large Trans-Neptunian Objects", Icarus **185**, 258–273 (2006).

Jewitt, D. C. and J. Luu, "Crystalline Water Ice on the Kuiper Belt Object (50000) Quaoar", Nature **432**, 731–733 (2004).

Jewitt, D. C. and S. S. Sheppard, "Physical Properties of Trans-Neptunian Object (20000) Varuna", Astronomical Journal **123**, 2110–2120 (2002).

Kohlstedt, D. L., B. Evans and S. J. Mackwell, "Strength of the Lithosphere: Constraints Imposed by Laboratory Experiments", Journal of Geophysics Research **100**, 17587–17602 (1995).

Lacerda, P., "The Dark Red Spot on KBO Haumea", in "IAU Symposium", edited by J. A. Fernandez, D. Lazzaro, D. Prialnik and R. Schulz, vol. 263 of *IAU Symposium*, pp. 192–196 (2010).

Lacerda, P., D. Jewitt and N. Peixinho, "High-Precision Photometry of Extreme KBO 2003 EL_{61}", Astronomical Journal **135**, 1749–1756 (2008).

Lacerda, P. and D. C. Jewitt, "Densities of Solar System Objects from Their Rotational Light Curves", Astronomical Journal **133**, 1393 (2007).

Leinhardt, Z. M., R. A. Marcus and S. T. Stewart, "The Formation of the Collisional Family Around the Dwarf Planet Haumea", Astrophysical Journal **714**, 1789–1799 (2010).

Lellouch, E., C. Kiss, P. Santos-Sanz, T. G. Müller, S. Fornasier, O. Groussin, P. Lacerda, J. L. Ortiz, A. Thirouin, A. Delsanti, R. Duffard, A. W. Harris, F. Henry, T. Lim, R. Moreno, M. Mommert, M. Mueller, S. Protopapa, J. Stansberry, D. Trilling, E. Vilenius, A. Barucci, J. Crovisier, A. Doressoundiram, E. Dotto, P. J. Gutiérrez, O. Hainaut, P. Hartogh, D. Hestroffer, J. Horner, L. Jorda, M. Kidger, L. Lara, M. Rengel, B. Swinyard and N. Thomas, ""TNOs Are Cool": A Survey of the Trans-Neptunian Region. II. The Thermal Lightcurve of (136108) Haumea", Astronomy and Astrophysics **518**, L147 (2010).

Lockwood, A. C., M. E. Brown and J. Stansberry, "The Size and Shape of the Oblong Dwarf Planet Haumea", Earth Moon and Planets **111**, 127–137 (2014).

Milani, A. and P. Farinella, "The Age of the Veritas Asteroid Family Deduced by Chaotic Chronology", Nature **370**, 40–42 (1994).

Morbidelli, A., H. F. Levison and R. Gomes, *The Dynamical Structure of the Kuiper Belt and Its Primordial Origin*, pp. 275–292 (2008).

Newton, I., *The Principia : Mathematical Principles of Natural Philosophy* (Berkeley, CA: University of California Press, 1999).

Pál, A., C. Kiss, T. G. Müller, P. Santos-Sanz, E. Vilenius, N. Szalai, M. Mommert, E. Lellouch, M. Rengel, P. Hartogh, S. Protopapa, J. Stansberry, J.-L. Ortiz, R. Duffard, A. Thirouin, F. Henry and A. Delsanti, ""TNOs Are Cool": A Survey of the Trans-Neptunian Region. VII. Size and Surface Characteristics of (90377) Sedna and 2010 EK_{139}", Astronomy and Astrophysics **541**, L6 (2012).

Pinilla-Alonso, N., R. Brunetto, J. Licandro, R. Gil-Hutton, T. L. Roush and G. Strazzulla, "The Surface of (136108) Haumea (2003 EL{61}), the Largest Carbon-Depleted Object in the Trans-Neptunian Belt", Astronomy and Astrophysics **496**, 547–556 (2009).

Porter, S. B., S. J. Desch and J. C. Cook, "Micrometeorite Impact Annealing of Ice in the Outer Solar System", Icarus **208**, 492–498 (2010).

Pravec, P., A. W. Harris and T. Michalowski, "Asteroid Rotations", Asteroids III pp. 113–122 (2002).

Press, W. H., S. A. Teukolsky, W. T. Vetterling and B. P. Flannery, *Numerical Recipes in FORTRAN. The Art of Scientific Computing* (Cambridge University Press, 1992).

Quick, L. C., L. S. Glaze and S. M. Baloga, "Rheology of Lava on Europa and the Emergence of Cryovolcanic Domes", in "Lunar and Planetary Science Conference", vol. 46 of *Lunar and Planetary Science Conference*, p. 1060 (2015).

Rabinowitz, D. L., K. Barkume, M. E. Brown, H. Roe, M. Schwartz, S. Tourtellotte and C. Trujillo, "Photometric Observations Constraining the Size, Shape, and Albedo of 2003 EL61, a Rapidly Rotating, Pluto-sized Object in the Kuiper Belt", Astrophysical Journal **639**, 1238–1251 (2006).

Ragozzine, D. and M. E. Brown, "Candidate Members and Age Estimate of the Family of Kuiper Belt Object 2003 EL61", Astronomical Journal **134**, 2160–2167 (2007).

Ragozzine, D. and M. E. Brown, "Orbits and Masses of the Satellites of the Dwarf Planet Haumea (2003 EL61)", Astronomical Journal **137**, 4766–4776 (2009).

Ragozzine, D., M. E. Brown, C. A. Trujillo and E. L. Schaller, "Orbits and Masses of the 2003 EL61 Satellite System", in "AAS/Division for Planetary Sciences Meeting Abstracts #40", vol. 40 of *Bulletin of the American Astronomical Society*, p. 462 (2008).

Rubin, M. E., S. J. Desch and M. Neveu, "The Effect of Rayleigh-Taylor Instabilities on the Thickness of Undifferentiated Crust on Kuiper Belt Objects", Icarus **236**, 122–135 (2014).

Schlichting, H. E. and R. Sari, "The Creation of Haumea's Collisional Family", Astrophysical Journal **700**, 1242–1246 (2009).

Sheppard, S. S. and D. Jewitt, "Extreme Kuiper Belt Object 2001 QG_{298} and the Fraction of Contact Binaries", Astronomical Journal **127**, 3023–3033 (2004).

Sheppard, S. S. and D. C. Jewitt, "Time-resolved Photometry of Kuiper Belt Objects: Rotations, Shapes, and Phase Functions", Astronomical Journal **124**, 1757–1775 (2002).

Sicardy, B., J. L. Ortiz, M. Assafin, E. Jehin, A. Maury, E. Lellouch, R. Gil-Hutton, F. Braga-Ribas, F. Colas, J. Lecacheux, F. Roques, P. Santos-Sanz, N. Morales, A. Thirouin, J. I. B. Camargo, R. Vieira-Martins, M. Gillon, J. Manfroid, R. Behrend and T. Widemann, "Size, Density, Albedo and Atmosphere Limit of Dwarf Planet Eris from a Stellar Occultation", in "EPSC-DPS Joint Meeting 2011", p. 137 (2011).

Tassoul, J.-L., *Theory of Rotating Stars* (Princeton University Press, 1978).

Tegler, S. C., W. M. Grundy, W. Romanishin, G. J. Consolmagno, K. Mogren and F. Vilas, "Optical Spectroscopy of the Large Kuiper Belt Objects 136472 (2005 FY9) and 136108 (2003 EL61)", Astronomical Journal **133**, 526–530 (2007).

Thomas, P. C., J. A. Burns, P. Helfenstein, S. Squyres, J. Veverka, C. Porco, E. P. Turtle, A. McEwen, T. Denk, B. Giese, T. Roatsch, T. V. Johnson and R. A. Jacobson, "Shapes of the Saturnian Icy Satellites and Their Significance", Icarus **190**, 573–584 (2007).

Thomas, P. J., R. T. Reynolds, S. W. Squyres and P. M. Cassen, "The Viscosity of Miranda", in "Lunar and Planetary Science Conference", vol. 18 of *Lunar and Planetary Science Conference*, p. 1016 (1987).

Trujillo, C. A., M. E. Brown, K. M. Barkume, E. L. Schaller and D. L. Rabinowitz, "The Surface of 2003 EL_{61} in the Near-Infrared", Astrophysical Journal **655**, 1172–1178 (2007).

Turcotte, D. L. and G. Schubert, *Geodynamics* (Cambridge University Press, 2002).

Tyldesley, J.-R., *An Introduction to Tensor Analysis for Engineers and Applied Scientists* (London: Longman, 1975).

Weaver, H. A., S. A. Stern, M. J. Mutchler, A. J. Steffl, M. W. Buie, W. J. Merline, J. R. Spencer, E. F. Young and L. A. Young, "S/2005 P 1 and S/2005 P 2", IAU Circular **8625**, 1 (2005).

APPENDIX A

Derivation of Maclaurin's Formula

Appendix A

DERIVATION OF MACLAURIN'S FORMULA

To derive the equilibrium shapes of a homogeneous body rotating with a uniform angular velocity ω, we must first start with the second order virial equation. This equation relates potential energy, moment of inertia, and pressure tensors. But to show where the second order virial equation comes from, first we must take one more step back, to the hydrodynamic equation which describes fluid motions within the body. (Unless otherwise referenced, this material is collected from Chandrasekhar 1987). Let $\mathcal{P} \equiv \mathcal{P}(x,t)$ be isotropic pressure, and let $\rho \equiv \rho(x,t)$ be density. Also, let x_i be the coordinate in the i^{th} direction, u_i be the velocity component in the i^{th} direction, and similar for ω_i. Some other physical definitions are in order before we get to the hydrodynamic equation. The gravitational potential is defined as

$$\Phi(x) = G \int_V \frac{\rho(x')}{|x - x'|} dx', \tag{A.1}$$

where $\rho(x')/|x - x'|$ is integrated over the entire volume V of the body. Using this potential, the potential energy is calculated according to the following equation:

$$P = -\frac{1}{2} \int_V \rho \, \Phi \, dx \tag{A.2}$$

and kinetic energy is defined as

$$K = \frac{1}{2} \int_V \rho |\vec{u}|^2 dx. \tag{A.3}$$

Another important physical quantity will be the moment of inertia I, which is defined as

$$I = \int_V \rho(x) |x|^2 dx. \tag{A.4}$$

A final quantity of importance is the work done by the system, Π:

$$\Pi = \int_V \mathcal{P} dx. \tag{A.5}$$

What will be needed in the second order virial equation are the tensor forms of the gravitational potential, potential energy, kinetic energy, and moment of inertia, respectively:

$$\Phi_{ij}(x) = G \int_V \rho(x') \frac{(x_i - x_i')(x_j - x_j')}{|x - x'|^3} dx', \tag{A.6}$$

$$P_{ij} = -\frac{1}{2} \int_V \rho \Phi_{ij} dx = \int_V \rho x_i \frac{\partial \Phi}{\partial x_j} dx, \tag{A.7}$$

$$K_{ij} = \frac{1}{2} \int_V \rho u_i u_j dx, \tag{A.8}$$

and

$$I_{ij} = \int_V \rho x_i x_j dx. \tag{A.9}$$

With the proper physical quantities defined, now we are ready to begin deriving the second order virial equation by beginning with the hydrodynamic equation. If gravity is the only force to which the body is subject, then in a frame of reference that is rotating with the body's own uniform angular velocity, the hydrodynamic equation is

$$\rho \frac{du_i}{dt} = -\frac{\partial \mathcal{P}}{\partial x_i} + \rho \frac{\partial \Phi}{\partial x_i} + \frac{1}{2} \rho \frac{\partial}{\partial x_i} |\vec{\omega} \times \vec{x}|^2 + 2\rho \epsilon_{ilm} u_l \omega_m. \tag{A.10}$$

The notation ϵ_{ilm} is the Levi-Civita symbol, defined with respect to the permutation of i, l, and m according to the following convention (Tyldesley 1975):

$$\epsilon_{ilm} = \begin{cases} 1 & \text{if } (i,j,k) \text{ is } (1,2,3), (2,3,1), \text{ or } (3,1,2), \\ -1 & \text{if } (i,j,k) \text{ is } (3,2,1), (2,1,3), \text{ or } (1,3,2), \\ 0 & \text{if } i = j, \ j = k, \text{ or } k = i. \end{cases} \tag{A.11}$$

The last two terms on the right side of the hydrodynamic equation represent the centrifugal potential and the Coriolis acceleration, respectively. To obtain the virial equation of second order, the hydrodynamic equation above must be multiplied by x_j and then integrated over the entire volume V:

$$\int_V \rho \frac{du_i}{dt} x_j dx = -\int_V x_j \frac{\partial \mathcal{P}}{\partial x_i} dx + \int_V \rho x_j \frac{\partial \Phi}{\partial x_i} dx + \frac{1}{2} \int_V \rho x_j \frac{\partial}{\partial x_i} |\vec{\omega} \times \vec{x}|^2 dx + 2 \int_V \rho \epsilon_{ilm} u_l \omega_m x_j dx. \tag{A.12}$$

Each of these terms simplifies and will be treated from left to right. Beginning with the term on the left side, since $d(u_i x_j)/dt = (du_i/dt)x_j + u_i u_j$, and if ρ is treated as a constant for each fluid element, then

$$\begin{aligned} \int_V \rho \frac{du_i}{dt} x_j dx &= \int_V \rho [\frac{d}{dt}(u_i x_j) - u_i u_j] dx \\ &= \int_V \rho \frac{d}{dt}(u_i x_j) dx - \int_V \rho u_i u_j dx \\ &= \frac{d}{dt} \int_V \rho u_i x_j dx - 2K_{ij}. \end{aligned} \tag{A.13}$$

Addressing the first term on the right side, using integration by parts,

$$-\int_V x_j \frac{\partial \mathcal{P}}{\partial x_i} dx = -\mathcal{P}_i x_j \Big|_V + \int_V \mathcal{P}_i dx_j.$$

Since $\mathcal{P} = 0$ on the boundary of the volume, the first term on the right vanishes. The second term on the right will vanish if $i \neq j$, since $\mathcal{P}_i$ must be acting in the same direction as x_j, so

$$-\int_V x_j \frac{\partial \mathcal{P}}{\partial x_i} dx = \delta_{ij} \int_V \mathcal{P} dx = \delta_{ij} \Pi, \tag{A.14}$$

where δ_{ij} is the Kronecker delta, defined as

$$\delta_{ij} = \begin{cases} 0 & \text{if } i \neq j \\ 1 & \text{if } i = j \end{cases} \tag{A.15}$$

Moving on to the second term on the right side of the virial equation, this expression is simplified by starting elsewhere, with the definition of P_{ij}:

$$\begin{aligned} P_{ij} &= -\frac{1}{2}\int_V \rho\Phi_{ij}dx \\ &= -\frac{1}{2}G\iint_V \rho(x)\rho(x')\frac{(x_i - x_i')(x_j - x_j')}{|x - x'|^3}dxdx'. \end{aligned} \tag{A.16}$$

Since $x_i = -x_i'$,

$$\begin{aligned} P_{ij} &= -G\iint_V \rho(x)\rho(x')\frac{x_i(x_j - x_j')}{|x - x'|^3}dxdx' \\ &= +G\iint_V \rho(x)x_i dx\frac{\partial}{\partial x_j}\int\frac{\rho(x')}{|x - x'|}dx' \\ &= \int_V \rho x_i\frac{\partial\Phi}{\partial x_j}dx. \end{aligned} \tag{A.17}$$

So the second term on the right side of the virial equation is P_{ij}. Or rather, to be more precise, the term is P_{ji}, which is equivalent to P_{ij}.

The simplification of the third term (the centrifugal force term) on the right side of Equation (A.12) starts with the expansion of the $|\vec{\omega}\times\vec{x}|^2$ component. Since

$$\vec{\omega}\times\vec{x} = (\omega_j x_k - \omega_k x_j)\hat{\imath} + (\omega_k x_i - \omega_i x_k)\hat{\jmath} + (\omega_i x_j - \omega_j x_i)\hat{k}, \tag{A.18}$$

it follows that

$$|\vec{\omega}\times\vec{x}|^2 = (\omega_j x_k - \omega_k x_j)^2 + (\omega_k x_i - \omega_i x_k)^2 + (\omega_i x_j - \omega_j x_i)^2. \tag{A.19}$$

Differentiating $|\vec{\omega}\times\vec{x}|^2$ with respect to x_i, after some algebra it turns out that

$$\frac{\partial}{\partial x_i}|\vec{\omega}\times\vec{x}|^2 = 2\omega_k^2 x_i - 2\omega_i\omega_k x_k + 2\omega_j^2 x_i - 2\omega_i\omega_j x_j. \tag{A.20}$$

Plugging this expression back into the centrifugal force term of the virial equation,

$$\begin{aligned}\frac{1}{2}\int_V \rho x_j \frac{\partial}{\partial x_i}|\vec{\omega}\times\vec{x}|^2 dx &= \frac{1}{2}\int_V \rho(2\omega_k^2 x_i x_j - 2\omega_i\omega_k x_k x_j + 2\omega_j^2 x_i x_j - 2\omega_i\omega_j x_j^2)dx \\ &= \int_V \rho(\omega_k^2+\omega_j^2)x_i x_j dx - \int_V \rho(\omega_i\omega_k)x_k x_j dx - \int_V \rho(\omega_i\omega_j)x_j^2 dx.\end{aligned}$$

Since the angular velocity about one direction is 0, we can set that to be the i direction. Then $\omega_k^2+\omega_j^2 = \omega_i^2+\omega_j^2+\omega_k^2 = |\vec{\omega}|^2 = \omega^2$. Using this along with the definition of I_{ij}, we then have

$$\frac{1}{2}\int_V \rho x_j \frac{\partial}{\partial x_i}|\vec{\omega}\times\vec{x}|^2 dx = \omega^2 I_{ij} - \omega_i\omega_k I_{kj} - \omega_i\omega_j I_{jj}. \tag{A.21}$$

According to Chandrasekhar, $I_{jj} = I$, and this term vanishes. The centrifugal force term finally simplifies to

$$\frac{1}{2}\int_V \rho x_j \frac{\partial}{\partial x_i}|\vec{\omega}\times\vec{x}|^2 dx = \omega^2 I_{ij} - \omega_i\omega_k I_{kj}. \tag{A.22}$$

Simplifying the final Coriolis acceleration term on the right side of the virial equation is the quickest one, as the Levi-Civita symbol and angular velocity are taken out of the integral:

$$2\int_V \rho\epsilon_{ilm}u_l\omega_m x_j dx = 2\epsilon_{ilm}\omega_m \int_V \rho u_l x_j dx. \tag{A.23}$$

After simplifying all of its terms, the second order virial equation in a rotating reference frame can be written as

$$\frac{d}{dt}\int_V \rho u_i x_j dx = 2K_{ij} + \delta_{ij}\Pi + P_{ij} + \omega^2 I_{ij} - \omega_i\omega_k I_{kj} + 2\epsilon_{ilm}\omega_m \int_V \rho u_l x_j dx. \tag{A.24}$$

If the body is in steady state, in other words, if Haumea's mass is not migrating from one place to another within the body, then the term on the left side of the virial equation vanishes. If the object is static in rotating frame, so that there are

no motions of the body within the frame of reference, then the kinetic energy term vanishes, as well as the last term on the right side, since the velocity $u_l = 0$. The second order virial equation then simplifies to

$$P_{ij} + \omega^2 I_{ij} - \omega_i \omega_k I_{kj} = -\delta_{ij}\Pi. \tag{A.25}$$

Since rotation is about the x_3-axis, we will set $k = 3$. Then $-\omega_i\omega_k I_{kj} = -\omega^2\delta_{i3}I_{3j}$, and the final form of the virial equation appropriate to our setup of a rotating object with homogeneous density is

$$P_{ij} + \omega^2(I_{ij} - \delta_{i3}I_{3j}) = -\delta_{ij}\Pi. \tag{A.26}$$

Examination of the diagonal elements of this equation leads to the following relationships:

$$P_{11} + \omega^2 I_{11} = -\Pi. \tag{A.27}$$

Similarly,

$$P_{22} + \omega^2 I_{22} = -\Pi \tag{A.28}$$

and

$$P_{33} = -\Pi, \tag{A.29}$$

so that

$$P_{11} + \omega^2 I_{11} = P_{33}. \tag{A.30}$$

This last equation will be used to derive Maclaurin's formula. Before starting this directly, though, at this point, another group of definitions needs to be made. A particular integral form pops up commonly when dealing with ellipsoids, which relates the three ellipsoidal axes. Two primary forms, in singly index dependent and doubly index dependent versions, are defined as follows:

$$A_i = a_1 a_2 a_3 \int_0^\infty \frac{du}{\Delta(a_i^2 + u)} \tag{A.31}$$

$$A_{ij} = a_1 a_2 a_3 \int_0^\infty \frac{du}{\Delta(a_i^2 + u)(a_j^2 + u)} \tag{A.32}$$

$$B_i = a_1 a_2 a_3 \int_0^\infty \frac{u\, du}{\Delta(a_i^2 + u)} \tag{A.33}$$

$$B_{ij} = a_1 a_2 a_3 \int_0^\infty \frac{u\, du}{\Delta(a_i^2 + u)(a_j^2 + u)} \tag{A.34}$$

where

$$\Delta = \sqrt{(a_1^2 + u)(a_2^2 + u)(a_3^2 + u)}. \tag{A.35}$$

With some quick algebra, an important relation between the above definitions can be shown:

$$B_{ij} = A_j - a_i^2 A_{ij}. \tag{A.36}$$

According to Corollary 2 of Theorem 14, on page 57 of Chandrasekhar (1987),

$$\frac{P_{ij}}{\pi G \rho} = -2 A_i I_{ij}. \tag{A.37}$$

Plugging this relationship into Equation (A.30) results in the following equation:

$$-2A_1 I_{11} + \frac{\omega^2}{\pi G \rho} I_{11} = -2 A_3 I_{33}. \tag{A.38}$$

And again, if eccentricity e is defined as that of the $a_1 - a_3$ plane, $e = [1 - (a_3^2/a_1^2)]^{1/2}$, then solving the above equation for $\omega^2/(\pi G \rho)$ gives

$$\begin{aligned} \frac{\omega^2}{\pi G \rho} &= \frac{2A_1 I_{11} - 2A_3 I_{33}}{I_{11}} \\ &= 2(A_1 - A_3 \frac{I_{33}}{I_{11}}). \end{aligned} \tag{A.39}$$

But $I_{11} \propto a_1^2$ and $I_{33} \propto a_3^2$, so then

$$\frac{\omega^2}{\pi G \rho} = 2(A_1 - A_3 \frac{a_3^2}{a_1^2}) = 2(A_1 - A_3(1 - e^2)). \tag{A.40}$$

Alternate definitions in terms of e can be made for A_1, A_2, and A_3. In the case where $a_1 = a_2 > a_3$, in other words when we have a Maclaurin spheroid, then

$$A_1 = A_2 = \frac{(1-e^2)^{1/2}}{e^3} \sin^{-1} e - \frac{1-e^2}{e^2} \tag{A.41}$$

and

$$A_3 = \frac{2}{e^2} - \frac{2(1-e^2)^{1/2}}{e^3} \sin^{-1} e. \tag{A.42}$$

If these alternate forms for A_1 and A_3 are plugged into Equation (A.40), then the following relationship emerges:

$$\frac{\omega^2}{\pi G \rho} = \frac{2(1-e^2)^{1/2}}{e^3}(3-2e^2) \sin^{-1} e - \frac{6(1-e^2)}{e^2}. \tag{A.43}$$

This equation is Maclaurin's formula. It is important in shape dynamics, as it relates the eccentricity or oblateness of an oblate spheroid to the spheroid's rate of spin and its density. This equation only applies to bodies of homogeneous density, and so it will only be useful to model Haumea if we consider it to be made of the same material inside and out. We know this cannot be the case, however, since Haumea's overall density suggests a large component of a material much denser than water ice, which is all that we see on its surface.

APPENDIX B

Derivation of Jacobi's Formula

Appendix B

DERIVATION OF JACOBI'S FORMULA

Revisiting Equation A.26,

$$P_{ij} + \omega^2(I_{ij} - \delta_{i3}I_{3j}) = -\delta_{ij}\Pi, \tag{B.1}$$

we will now search for a solution of triaxial shape, i.e. a shape in which all three axes are unequal. In speaking about triaxial ellipsoids, also known as Jacobi ellipsoids, we will use the convention $a_1 > a_2 > a_3$, where in the case of Haumea (and in most all cases), the smallest axis (a_3) is coincident with the rotational axis. Rewriting the diagonal elements of the above relationship, we find again that

$$P_{11} + \omega^2 I_{11} = P_{22} + \omega^2 I_{22} = P_{33}, \tag{B.2}$$

since each of these elements is equal to $-\Pi$. Making use of Equation A.37, the above expression becomes

$$\frac{\omega^2}{\pi G\rho}I_{11} - 2A_1 I_{11} = \frac{\omega^2}{\pi G\rho}I_{22} - 2A_2 I_{22} = -2A_3 I_{33}. \tag{B.3}$$

And since $I_1 \propto a_1^2$, $I_2 \propto a_2^2$, and $I_3 \propto a_3^2$, then

$$\frac{\omega^2}{\pi G\rho}a_1^2 - 2A_1 a_1^2 = \frac{\omega^2}{\pi G\rho}a_2^2 - 2A_2 a_2^2 = -2A_3 a_3^2. \tag{B.4}$$

Now, if the term $2a_1^2 a_2^2 A_{12}$ is added to each side of the equation above, and knowing that $A_{12} = A_{21}$ and $B_{12} = B_{21}$, we will make use of Equation A.36 to get

$$a_1^2(\frac{\omega^2}{\pi G\rho} - 2A_1 + 2a_2^2 A_{12}) = a_2^2(\frac{\omega^2}{\pi G\rho} - 2A_2 + 2a_1^2 A_{12}) = 2(a_1^2 a_2^2 A_{12} - A_3 a_3^2)$$

$$\Rightarrow a_1^2(\frac{\omega^2}{\pi G\rho} - 2(A_1 - a_2^2 A_{21})) = a_2^2(\frac{\omega^2}{\pi G\rho} - 2(A_2 - a_1^2 A_{12})) = 2(a_1^2 a_2^2 A_{12} - A_3 a_3^2)$$

$$\Rightarrow a_1^2(\frac{\omega^2}{\pi G\rho} - 2B_{21}) = a_2^2(\frac{\omega^2}{\pi G\rho} - 2B_{12}) = 2(a_1^2 a_2^2 A_{12} - A_3 a_3^2). \tag{B.5}$$

If $a_1 \neq a_2$, then the solutions to these equations conform to the following conditions:

$$\frac{\omega^2}{\pi G\rho} = 2B_{12} \tag{B.6}$$

and

$$a_1^2 a_2^2 A_{12} = a_3^2 A_3. \tag{B.7}$$

These conditions were derived by Jacobi. The first condition, when expanded, gives the following relationship between angular velocity, density, and all three axes:

$$\frac{\omega^2}{\pi G\rho} = 2a_1 a_2 a_3 \int_0^\infty \frac{u\, du}{\Delta(a_1^2 + u)(a_2^2 + u)}. \tag{B.8}$$

This equation is one of the primary tools used to model homogeneous triaxial ellipsoids. Again, Haumea is not a homogeneous ellipsoid, but if it turns out to be mostly composed of silicate material with just a thin ice veneer on the outside, then this equation is useful and will allow us to achieve a close approximation to Haumea's true nature.

The second condition provides a geometric constraint to the body, as it sets up a relationship between the three axes. This condition must be met in order for equilibrium to be achieved within the object. Thus, it describes a Jacobi ellipsoid. This condition can be partially rewritten in terms of the axial ratios. If $a_2/a_1 = p$ and $a_3/a_1 = q$, then the second condition can be written as

$$a_1^2 p^2 A_{12} = q^2 A_3 \tag{B.9}$$

$$\Rightarrow p^2 \int_0^\infty \frac{a_1^2\, du}{\Delta(a_1^2 + u)(a_2^2 + u)} = q^2 \int_0^\infty \frac{du}{\Delta(a_3^2 + u)}. \tag{B.10}$$

An interesting occurrence is that, at the precise point where $\omega^2/(\pi G\rho) = 2B_{11}$, the object's shape can quasistatically deform from a Maclaurin spheroid to a Jacobi

ellipsoid. When this angular velocity is exceeded, the equilibrium shape can then be either an oblate spheroid or a triaxial ellipsoid. This is the point at which the Jacobi curve becomes separate from the Maclaurin curve.